C02018: Doctor of Philosophy
CRICOS Code: 0000
Subject Code: 1234
Feb. 2020

Wireless Off-body Channel Analysis and Sparse Modeling

Pengfei Cui

School of Communication and Computation
Faculty of Engineering & IT
University of Technology Sydney
NSW - 2007, Australia

UNIVERSITY OF TECHNOLOGY SYDNEY

Wireless Off-body Channel Analysis and Sparse Modeling

A thesis submitted in partial fulfilment of the requirements
for the degree of

Doctor of Philosophy
in
Analytics

by
Pengfei Cui

to
School of Communication and Computation
Faculty of Engineering and IT
University of Technology Sydney, Australia

June 21, 2020

CERTIFICATE OF ORIGINAL AUTHORSHIP

I, *Pengfei Cui* declare that this thesis, is submitted in fulfilment of the requirements for the award of Doctor of Philosophy, in the *School of Communication and Computation*, *Faculty of Engineering & IT* at the University of Technology Sydney.

This is wholly my own work unless otherwise referenced or acknowledged. In addition, I certify that all information sources and literature used are indicated in the thesis.

This document has not been submitted for qualifications at any other academic institution. I certify that the work in this thesis has not previously been submitted for a degree nor has it been submitted as part of the requirements for a degree at any other academic institution except as fully acknowledged within the text. This thesis is the result of a Collaborative Doctoral Research Degree program with Nanjing University of Posts and Telecommunications.

This research is supported by the Australian Government Research Training Program.

Production Note:
SIGNATURE: Signature removed prior to publication.

DATE: 15th Feb., 2020

Acknowledgments

First and foremost, I would like to express my sincere gratitude to my supervisors Professor J. Andrew Zhang and Y. Jay Guo for their guidance, support and encouragement throughout my PhD studies. Thank you for the patient guidance and extra encouragement. I will remain forever grateful for the research skills, patience and vast knowledge you passed on to me.

I would like to thank Global Big Data Technologies Centre, Jiangsu Key Laboratory of Wireless Communications for their funding and other supports during my PhD research.

I would like to thank Dr Weiwei Zhou, Ping Chu, Yuyue Luo, Bai Yan, Zhenguo Shi, Xin Yuan, Lang Chen, Chuan Qin, Dianhao Zhen, Can Ding, Mingye Ju, Yujiao Wu and Wenwei Mo for their help during my research.

My special thanks go to professor Hongbo Zhu, Wenjun for research guidance and financial support to research, training and travel.

Finally, I would like to thank my family and friends for their continual support and encouragement. I would like to single out Mum, Dad and Hui Deng in particular for always being their for me.

Publications

The following papers have been written based on the materials presented in this thesis.

JOURNAL PAPERS :

1. **Peng-fei Cui**, J. Andrew Zhang, Wen-Jun Lu, Y. Jay Guo, and HongBo Zhu. Statistical sparse channel modeling for measured and simulated wireless temporal channels. *IEEE Transactions on Wireless Communications*, Sep. 2019.

2. **Peng-fei Cui**, Yu Yu, Wen-Jun Lu, Yang Liu, and Hong-Bo Zhu. Measurement and modeling of wireless off-body propagation characteristics under hospital environment at 6-8.5 GHz. *IEEE Access*, 5:10915–10923, 2017.

3. **Peng-fei Cui**, Wen-Jun Lu, Yu Yu, B. Xue, and Hong-Bo Zhu. Off-body spatial diversity reception using circular and linear polarization: measurement and modeling. *IEEE Communications Letters*, 22(1):209–212, Jan. 2018.

4. Yu Yu, **Peng-fei Cui**, Wen-Jun Lu, Yang Liu, and HongBo Zhu. Off-body radio channel impulse response model under hospital environment: measurement and modeling. *IEEE Communications Letters*, 20(11):2332–2335, Nov. 2016.

5. Jun She, Wen-Jun Lu, Yang Liu, **Peng-fei Cui**, and HongBo Zhu. An experimental massive mimo channel matrix model for hand-held scenarios. *IEEE Access*, 7:33881–33887, 2019.

CONFERENCE PAPERS :

1. **Peng-fei Cui**, J. Andrew Zhang, Wen-jun Lu, Y. Jay Guo, and Hong-bo Zhu. Influence of human body on massive MIMO indoor channels. In *2019 IEEE 89th Vehicular Technology Conference (VTC2019-Spring)*, pages 1–6, June 2018.

2. **Peng-fei Cui**, J. Andrew Zhang, Wen-jun Lu, Y. Jay Guo, and Hong-bo Zhu. Sparse channel modeling using multi-measurement vector compressive sensing. In *2018 IEEE Global Communications Conference (GLOBECOM)*, pages 1–6, Dec 2018.

3. **Peng-fei Cui**, Yu Yu, Yang Liu, Wen-jun Lu, and Hong-bo Zhu. Body obstruction characteristics for off-body channel under hospital environment at 6-8.5 ghz. In *2016 IEEE International Conference on Ubiquitous Wireless Broadband (ICUWB)*, pages 1–4, Oct 2016.

4. **Peng-fei Cui**, Yu Yu, Yang Liu, Wen-jun Lu, and Hong-bo Zhu. Joint rls and lms adaptive equalization for indoor wireless communications under staircase environments. In *2015 International Conference on Wireless Communications Signal Processing (WCSP)*, pages 1–5, Oct 2015.

5. Yu Yu, **Peng-fei Cui**, Jun She, Yang Liu, Xi Yang, Wen-Jun Lu, Shi Jin, and Hong-Bo Zhu. Measurement and empirical modeling of massive MIMO channel matrix in real indoor environment. In *2016 8th International Conference on Wireless Communications Signal Processing (WCSP)*, pages 1–5, Oct 2016.

6. Jun She, Chen Gao, Yu Yu, **Peng-fei Cui**, Wen-jun Lu, Shi Jin, and Hong-bo Zhu. Measurements of massive MIMO channel in real environment with 8-antenna handset. In *2017 9th International Conference on Wireless Communications and Signal Processing (WCSP)*, pages 1–4, Oct 2017.

Contents

List of Figures

List of Tables

Abstract

The successful application of very rapidly growing wearable devices relies on the research on the propagation characteristics of off-body channels which plays a key role in connecting the wireless body area network and cellular network, WiFi and other local area networks. This thesis concentrates on the bottleneck problems of the measurement, analysis and modeling of the off-body propagation characteristics. A large number of measurement investigations have been carried out to solve the thorny problem of complicated and changeable scenes of off-body channel and heavy fading caused by adjacent humans. These activities include different transmission schemes, different influence factors, and typical changeable configurations. Then, in this study, the systematic analysis of the measured big channel datasets are conducted based on traditional large/small scale propagation analysis methods and compressive sensing based sparse channel analysis methods.

The first part of the thesis discusses the measurement and analysis of typical off-body channel types including single input single output (SISO), diversity reception and multiple input multiple output (MIMO). A two-factor integrated path loss model with variable body worn locations and variable access point (AP) height is proposed to improve the power management and link budgeting ability in off-body scenarios. A highly robust circularly polarized spatial diversity off-body scheme is made up and validated to tackle the heavy fading problem. In addition, the influences of humans including both hand-held effect and body obstruction effect on off-body transmission angular spectrum and capacity are estimated.

In the second part of the thesis, the novel compressive sensing based sparse channel analysis methods are proposed to deal with the modeling problems of off-body temporal channels with complex multipath components. The channel impulse response (CIR) models of SISO and MIMO channels based on single measurement vector (SMV) and multi-measurement vector (MMV-CS) compressive sensing methods respectively are established.

Finally, according to the off-body link types, the propagation characteristics, sparse analysis and modeling methods are integrated into several channel simulators with friendly GUI interface, whose source codes are shared on gitHub. Those models and simulators are expected to be used in theoretical analysis and engineering practice for the coverage planning, link simulation, algorithm design, and performance validation.

Chapter 1

Introduction

1.1 Off-body Wireless Communication

With the deployment of 5G and the ongoing research on Beyond 5G (B5G), cellular communication networks tend to be more deeply integrated with Body Area Network (WBAN) and Internet of Things (IoT). Both academia and industry expect to form a network that includes not only all people but also their belongings [2]. WBAN, especially Off-Body network, which implement the link function between human and the others, is the most critical part. In the IMT-2020 standard, the WBAN will become the most important application field with the fastest growth in the direction of 5G massive Machine Type Communication.

Channels in body area network can be classified into three types according to the relative positions of receiving and transmitting nodes, namely, in-body, on-body and off-body channels. In-body channel is defined as the transmission medium in which at least one transceiver is set inside the body; On-body channel refers to those when both transceivers are worn on the surface of the human body while the off-body channel is mainly defined as the transmission medium between body-worn devices and the remote Access Point (AP). Fig. 1.1 lists some examples for typical in-, on- and off-body channels.Their location of transceivers and transmission distance between transmitter and receiver are obviously different. Before 5G, researchers mainly focused on on- and in-body channels, which are connected to other networks through sink node or main

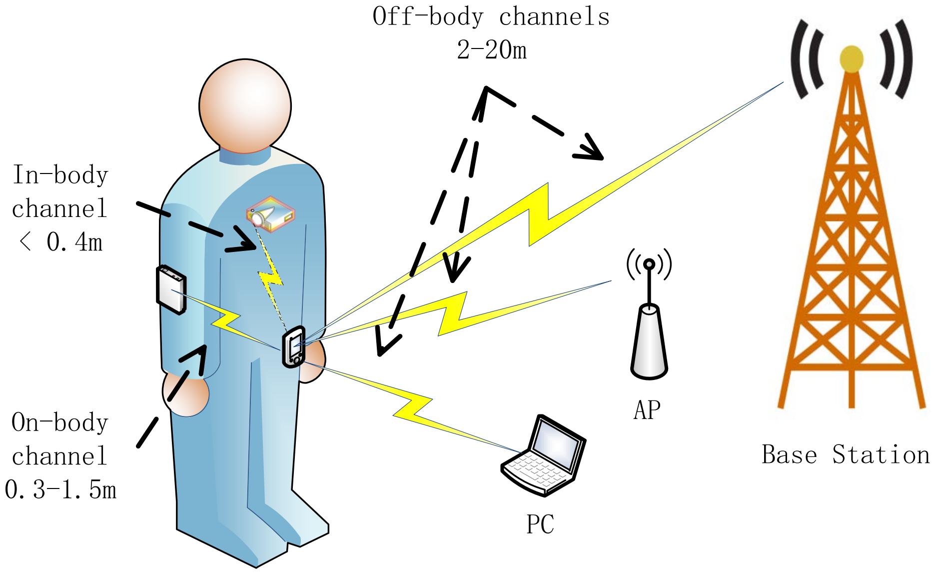

Figure 1.1: The illustration for WBAN channel types including off-body, in-body and on-body cases

node with strong communication ability and very large size [3]. However, it is found that such schemes may cause many severe problems in practice, such as failure of single point, user privacy disclosure and frequent network interupt. Meanwhile, the fast development of wireless portable equipment makes the direct off-body transmission scheme (i.e., body-worn devices directly linked to remote devices without any relay) feasible. Compared with the traditional scheme relying on the relay of collection node, off-body transmission not only overcomes many problems in traditional WBAN are but also has many advantages such as improving user experience, convenience in carrying, no limit to activity scope and low cost. This makes off-body communication a key enabling technology for the future mobile network.

The main task of off-body communication is to implement the interconnection between different WBANs or between WBAN and other heterogeneous networks (such as cellular network and WIFI network). Its initial task was to upload human health information (such as heart rate, blood pressure and temperature) and environment-related parameters (such as fire detection, smoke concentration and PM2.5 concentration) collected by WBAN for recording and analysis in a low rate and asynchronous communication way. With the expansion of users and wireless access demand, the number of access devices and transmission rate of wearable devices has increased rapidly, and the requirements for real-time and reliable transmission are also greatly increased. Accordingly, an off-body communication network is rapidly expanding from traditional health monitoring to sports, military, fitness, entertainment and intelligent home among others. At present, it is an urgent problem in off-body communication to improve real-time transmission capacity and transmission reliability [4]. For example, smart watches have evolved from a simple pedometer to forwarding messages, answering and making calls, controling apps by voice, intelligent assistant, posture recognition and automatic emergency alarm. These new needs require higher transmission capacity, lower delay and interrupt probability of off-body channel. In the future, with the integration of artificial intelligence, cloud computing and big data technology, wearable devices need to deal with a large amount of information with different priorities and will become the main personal proxy to control intelligent home, intelligent office and intelligent manufacturing, ultimately revolutionizing human-computer interaction mode and human social communication mode [5].

However, different from the traditional short distance wireless channel, the application of off-body communications are obstructed by many severe problems. On the one hand, as the portable devices are too close to the human body or implanted into the body, the off-body channel is vulnerable to human characteristics and human movement. For example, antenna-body effect is significant, transmission stability is limited by frequent body posture changes and mobility. This makes the systematic study of off-body propagation characteristics an urgent task [6]. On the other hand, considering that the transceivers of the off-body transmission are usually supported by heterogeneous networks, the physical layer design should meet the requirements of several different wireless access specifications (e.g. WBAN, WIFI, Bluetooth, ZigBee and Wimax). However, the strict limits on the size, power and electromagnetic absorption rate of then human body of wearable devices are often in conflict with the methods of improving transmission rate and link stability [7]. These factors directly lead to poor user experience and high market turnover rate although the enthusiasm for wearable applications is increasing rapidly. Therefore the study of communication characteristics of off-body channel can not only enrich the wireless communication theory, but also be beneficial to the wearable-device industry, i.e., it is important in both theoretical study and industrial application. Thus, the research of off-body channel has become a common focus of industry, academia and standardization organizations since the 4G era.

1.2 Motivation and background

Off-body channel is the key to connect WBAN and other networks. The research methodology is usually based on the combination of mature research theory of wireless short distance channel and the beneficial experience of on-body transmission so as to conduct targeted research on the characteristics and unique needs of off-body channel. In terms of frequency band, according to WBAN planning of IEEE802.15.6 , the research of off-body channel usually covers a wide range from 13.5MHz to 10.6GHz. In recent years, the rise of 28GHz and 60GHz millimeter-wave band in off-body channel research has further expanded its frequency range. This allows it to play an important role in many applications characterized by high performance, high concurrency and low latency. The robust off-body access technology is thus expected to be the enabling technology of improved quality of service (QoS) in wireless communication.

Targeting the basic research of off-body channel, this thesis is mainly focusing on two aspects, namely, the propagation characteristics and anti-fading measures, as well as sparse analysis and sparse modeling to deal with dimensional disaster problems in off-body application. The study of off-body propagation characteristics provides a research basis for sparse analysis, while sparse analysis and modeling further solve the frequently occurring "dimensional disaster problems" in the off-body propagation analysis. In order to establish a highly available, highly reliable and easy to implement off-body communication link, the specific research on off-body channel is further divided into four categories, shown in Fig. 1.2: The first is to study the large-scale and small-scale fading characteristics of off-body propagation. The second category is some anti-fading methods based on the propagation characteristics in the first category, aiming at the serious fading problems in off-body channel. In the third category, sparse analysis method is introduced to analyze the sparse characteristics of the off-body channel to solve the dimentional disaster problems and meet the needs of multi-channel joint processing in off-body

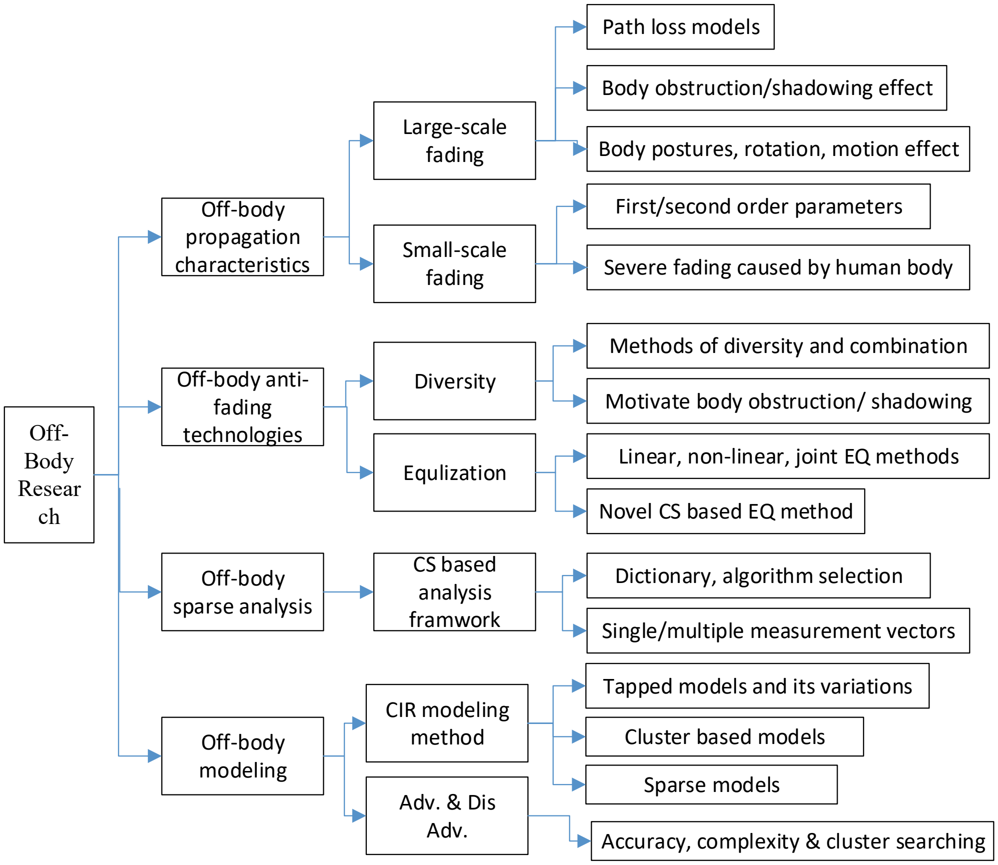

Figure 1.2: The classification for main research directions and content of off-body channels

transmission. Last but not least, based on the characteristics of sparse analysis, we discuss the advantages of sparse temporal channel modeling methods of off-body channels with complex cluster structures.

1.2.1 Off-body Propagation Characteristics

The propagation characteristics of off-body channel are mainly divided into two aspects: large-scale fading characteristics and small-scale fading characteristics. Studies of large-scale fading characteristics of off-body channels include path loss models, body obstruction/shadow effects, and the influences of body posture, body steering and motion. The research of small-scale fading characteristics mainly includes the statistical characteristics of key propagation parameters and the influence of the human body on fading characteristics.

When designing any wireless communication system, link budget should be considered first. Generally, the predicted power loss is the sum of average path loss of a large-scale range (usually several to hundreds of meters), the shadow variable with normal regular fluctuation (i.e. 1-5 dB) and the small-scale fading component with random fluctuation in a small range (several working wavelengths). The main task of link budget is to make up transmitter power to ensure that the predicted receiving power is greater than the demodulation threshold; meanwhile the budget power should be as low as possible to reduce interference for other APs and the interrupt probability should be as small as possible to guarantee Quality of Service (QoS). In the off-body channel, since the wearable device is too close to the human body, its shadow effect not only comes from the surrounding obstruction objects, but also from the complex effects of the human body, such as body obstruction, motion, coupling and diffraction. This makes the link budget in off-body channel significantly higher than that in general wireless short-range communication. In this case, it is crucial to design high-precision large-scale and small-scale models specially optimized for off-body channels to enable off-body communication. Thus, it is very important to study the influence of the human body as well as the closely related movement, posture change and other influencing factors to improve the performance of off-body transmission.

Off-body large-scale propagation characteristics

The most famous wireless short-distance channel model is the log-distance path loss model introduced by Friis in 1946 [8]. By generalizing its basic parameters, many large scale path loss models are formed. Since the path loss of adjacent near frequency bands is similar, frequency characteristics are generally not considered as the focus, so the logarithmic distance model is expressed as follows:

$$PL(d) = PL_0 + 10 \times \gamma \times log_{10}(d) + \delta_X \tag{1.1}$$

where PL_0 is the reference path loss predicted by free space path loss model, γ is the path loss exponents relevant to specific scenario and δ_X is the standard deviations for shadowing effect. In the off-body channel, the statistical distribution of these path loss parameters may change due to different combinations of influencing factors. The typical influencing factors include body obstruction, body rotation, motion status, AP height, wearing position, polarization characteristics, and antennae-body effect listed in Table 1.1. A variety of large-scale path loss models are proposed dependent on modeling preference of different parameters and different dominating factors of scenarios. According to their different hypothesis preference on PL_0, they can be roughly divided into three categories:

1. **Fixed reference path loss model**

   PL_0 is fixed in all the scenes based on one selected measurement value in a reference off-body scene, while other scenes are modified based on this reference. A logarithmic distance model of fixed reference path loss based on measurement is thus obtained. Its advantage is that the modification of the original model is minimal, the large-scale fading of all scenes is based on the superposition of a simple scene, the physical significance is very clear, and the path loss exponents and shadow deviation are easy to do comparative study in different scenes. The disadvantage is that the selection of the reference scene has a great influence, and its errors tend to be accumulated to other scenes.

2. **Floating reference path loss model**

   Compared with the fixed reference path loss model, the reference path loss PL_0 of floating path loss model changes dynamically according to the measured value in each scene. As the reference path loss values of all scenarios are different, the corresponding path loss exponents are also quite different. The advantage is that the reference path loss is usually more accurate according to the real-field measurement, and there is no error accumulation of the reference scene in fixed path loss. At the same time, it achieves a good balance between the physical meaning and the measured precision. The main disadvantage is that due to too many scenes in the off-body channel under the combined factors of body-worn positions, body rotation directions and motion influence etc; the generated floating reference path loss model needs to frequently update its key parameters PL_0, γ and even σ_X, which is not conducive to the design of the algorithm and the deployment of the actual WBAN.

3. **Intercept path loss model**

> In order to maintain the physical significance of the reference distance, the path loss values at the reference distance (usually 1m) of fixed/floating reference path loss models are generally associated with the actual measurement, and only the exponential path loss factor is fitted in the fitting. In the intercept model, the physical meaning of the reference path loss value is not restricted, and the PL_0 and γ of each scene are directly fitted by the least square or maximum likelihood estimation methods.
>
> The advantages of this method are clear. The dual parameter fitting can significantly improve the prediction accuracy under certain scenarios. However, its disadvantages are also very obvious. Firstly, it is only applicable to a particular scene and is sensitive to the change of scene. Meanwhile, the frequent changes of parameter table are unavoidable. Secondly, its physical meaning is not clear and such a model lacks theoretical interpretation and further parameter expansion. For example, in the case of severe obstruction or shadow cases (i.e., significant beam pass through walls, human body or crossing long distance), the measured path loss tends to remain unchanged or even decrease within a certain range (when transceiver steps away from the obstructions). In this case, the path loss exponents fitted by the intercept model may be 0 or negative, which obviously belongs to the over-fitting of the path loss in a specific scene and local range. Therefore such a kind of model is only suitable for a limited number of specialized scenarios.

Table 1.1 shows the research details for off-body channels in some literatures including off-body scenes, measurement setup, main influencing factors, large-scale modeling methods and typical parameters' range. It is found that there are many measurement systems widely used in the off-body channel, mainly including spectral analysis, time domain measurement, VNA measurement and correlation measurement. The measuring scenarios are concentrated in a microwave anechoic room, small, medium and large laboratory or office. The tested frequency band ranges from 820MHz to 12.7GHz, covering the popular cellular band, ISM band and UWB band. In a word, the measurement methods, measurement scenarios and test frequency of the off-body channel are relatively diverse and wide. The floating reference path loss model is most frequently adopted in the selection of large-scale models to balance the accuracy of

Table 1.1: The dominant influence factors, path loss exponents and shadow deviation of large-scale off-body models in some literatures

Cite	**Measure -ment Setup**	**Scenario**	**Freq -uency**	**Influence factors**	**Path Loss Models**	PL_0	**PLE** γ	δ_X
[9]	Vector signal source + spectral analysis	Small conference room	2.45 GHz	Body rotation, Motion, AP height	Floating Path loss model	42.6 dB	0.5-1.2	7.0-10.0
[10]	VNA Measure -ment	Medium conference room	3.1-8 GHz	Body -worn locations, Body obstruction	Floating Path loss model	49-57 dB	1.6-3.9	0.3-3.1
[11]	Time domain multi -channel measure -ment	Medium Lab	4.15 -4.25 GHz	Postures, Body -worn locations, Polar -ization	Fixed Path loss model	43 dB	1.29	4.29
[12]	Time domain correlation measure -ment	Medium Lab	4.5 -12.7 GHz	Antenna -Body, Worn locations, Motions	Intercept path loss model	74 dB	1.1-1.5	2.7-3.1
[13] [14] [15]	Ultra Wideband correlation measure -ment	Hospital	3.1-6.3 GHz	Worn locations, Postures, Motions, Rotation	Sub -section model+ Floating Path loss model	62-72 dB	0 or 2	1.8-2.8
[16]	HaLo430 Synch -ronized measure -ment	Cross multiple large offices	2.45 GHz	Wall obstruction , Body rotation, Motion	Comb -ination of multile models	-	-	0.5-3.8
[17]	VNA measure -ment	anechoic chamber	950 MHz	Arm waving, Foot span, Roation	Constant in small range area	-	-	0.5-3.5

the path loss fitting and the theoretical interpretation of off-body measured scene. However, these also lead to a large distributed range of path loss exponents. The wide range of path loss exponents from 0.5 to 10 is significantly different from traditional short range wireless channels. At the same time, the shadow deviation varies greatly in different off-body cases. On the one hand, it is caused by numerous combinations of influencing factors. On the other hand, the dominating influencing factors of even the same combination under different situations, such as crowd density, traffic flow partition and dense scene object occlusion, are also different.

Off-body small-scale propagation characteristics

Different from large-scale fading characteristics, small-scale parameters in short distance wireless channels are often difficult to predict directly due to their randomness, so probabilistic statistical models are commonly used in small-scale analysis and modeling. When making link budget, it is often necessary to consider the influence of small-scale fluctuations to ensure the connectivity of channel links. As small-scale off-body channel often experiences much more severe fading than that of traditional short distance channels, the small-mall characteristics play a key role in link budget and design of communication algorithms. At present, the research of small-scale characteristics in off-body mainly focuses on the distribution types and statistical parameters of multipath fading and shadow effect. In addition, a proportion of the research focus on the study of some human body related factors, such as electromagnetic absorption and the coupling of the human body, the impedance drift caused by human conductance characteristics.

Table 1.2 shows some research contents and conclusions about small-scale fading characteristics of in the offbody channel.The types of signal fading caused by the multipath effect vary greatly, depending on different scenes, different parts and even different wearers. These distributions mainly include lognormal, weible, Rayleigh, rice and Nakagami fading types. S. l. Cotton proposed a k-u distribution model, which was specifically used to describe serious off-body multipath fading scenarios, and produce a corresponding theoretical derivation [18]. Its advantage are that it contains typical Rayleigh and Rician fading cases and can describe

Table 1.2: Research contents and conclusions of small-scale fading characteristics of off-body channel in some literatures

Cite	**Scenario**	**Types of small-scall fading**	**Body shadow types**	**Influence factors**
[4]	Suburb road sides	k-u distribution	Log -normal	Vehicles' approach, obstruction and departure on signal attenuation and multipath distribution parameters; The orientation of human body; Long/short term fading caused by traffic flow
[8]	Small office	Rician, Nakagami, Weibull, Rayleigh	Log -normal	RMS delay spread and number of significant multipath components caused by adjacent human and motion
[9]	Medium office	Rician, Rayleigh	Normal	RMS delay spread features influenced by body roation
[10]	Medium office	Log-normal	Normal	Off-body capacity, Signal level crossing rate and correlations between different off-body links
[10]	Medium office	Log-normal	Normal	Signal level crossing rate and average fading durations influenced by body-worn locations and motion
[17]	Hospital	Log-normal Weibull	Normal	Time-varying features and obstruction probability influenced by scenarios
[12] [13] [14]	Crossing mulitple large offices	Log-normal Weibull	Normal	Signal level fluctuations, relative path loss, RMS delay spread
[15]	Anechoic chamber	Rayleigh	Log -normal	The variation of capacity, bit error rate and correlation under different off-body scenarios
[18]	Small officer	k-u distribution	Log -normal	Therotic validation for distributions and off-body multipath analysis
[16]	Laboratory	Rayleigh	Log -normal	Variation of fading types under the influence of arm waving, efficiency of antenna radiation and shadowing

distribution types that are more serious than both Rayleigh and Rician fading channels. Its disadvantages are that the model is too complex, hard to mathematically express and difficult to understand and generalize random dataset. Body shadow effects, by contrast, are typically modeled as either normal or log-normal, and the standard deviation is usually between 0.5 and 4. In addition to multipath fading types and body shadow effects, the statistics characteristics of RMS delay spread characteristics, multipath number, level crossing rate, average fading time, link capacity and bit error rate fluctuation receive more focus of researchers. All these small-scale parameters are closely associated with the combination of some factors such as body-worn position, body obstruction effect, channel line-of-sight status, body rotation angle, transceiver distance and motion influence. Among them, the first four have been most frequently studied and usually have the most important influence on in off-body communication.

The challenges faced by large-scale fading characteristics of off-body channel mainly include two aspects: 1) how to reasonably express a large number of influencing factors, such as variable wearing position, variable AP height, and variable human posture, with one or a few large-scale path loss models. On the premise of avoiding frequent switching of large-scale models, the prediction accuracy and scene expansibility are also key evaluating indexes. 2) The analysis and modeling of multi-dimensional off-body channel sets under the influence of aforementioned many factors. This analytical model is limited by the poor processing power of wearable devices and should be as easy to implement as possible. At the same time, in order to cope with the changeable scene of off-body communication , it is necessary to have a high adaptability and expansion ability for off-body applications. At this point, the current research progress and proposed methods seem to be a long way from meeting the development needs of wearable communication.

There are two main challenges in studying off-body small-scale fading channel characteristics : 1) in many traditional propagation characteristics, channel fading and the emerging of sparse characteristic portfolio, how to effectively filter out the combination of the key factors, find out the important correlation relationships between them, and finally understand how such optimal combination works in a small-scale fading profile. Such an optimal combination as the combination of RMS delay spread and level crossing rate, the packet of significant multipath number and channel cluster structure, etc. 2) different combinations of influencing factors in different scenarios, how to jointly analyze, model and visualize those useful results. The requirements for channel estimation, channel modeling, link budget or performance measurement are often different. However, due to the diversity of wearable communication scenarios, it is not practical or necessary to conduct channel measurement one by one. Therefore, it has become an urgent problem to design measurement scheme, a conduct reasonable analysis and modeling, and use storage or display methods beyond the existing combinations of graphs, tables and relational databases to visually and interactively present the research results of off-body measurement, analysis and parameter modeling. These are very important for deepening the theoretical research and practical application of off-body communication.

1.2.2 Off-body Anti-fading Measures

Through the study of the large/small scale propagation characteristics of the off-body channel, it is found that the multi-path effect in off-body channel is very complex due to the severe influence of human obstruction, movement and other interferences. This makes the off-body channel experience a much more serious fading than traditional short-range wireless cases. Meanwhile, antenna radiation fragmentation, impedance deviation and near-field coupling due to human-antenna effect will also cause additional fading to off-body communication. In addition, some studies have shown that the body channel is extremely susceptible to the polarization mismatch of the receiver [19], and the influence of the height changes caused by the body posture change on the fading of the off-body channel cannot be ignored. To sum up, effective measures must be taken to ease or eliminate the negative effects of various fading types on wearable communication. Generally, there are two kinds of anti-fading methods in wireless communication: one is channel diversity, the other is channel equalization. Because wearable devices are limited by computing power and implementation cost, they can only adopt a relatively simple equalization method, while the effect of a simple equalizer is often limited by applicable scenarios. [20] has found that only linear equilibrium can effectively cope with the fading caused by body obstruction through simulation and comparison of multiple body-worn parts of different wearers.

However, it has little effect on the severe fading caused by human movement, posture change and polarization mismatch. Therefore, the method of diversity is a better choice for easing fading and enhancing off-body link reliability.

There are four common channel diversity methods, namely, space diversity, polarization diversity (or antenna radiation diversity), frequency diversity and time diversity [21–23]. Due to the richness of human deployment location and the low cost of wearable devices, spatial diversity is usually the preferred method. The advantage of polarized diversity is that it occupies very little space and is easy to deploy, while the disadvantage is that polarized diversity gain is not as good as spatial diversity gain, so it will only be used in specific applications [24]. Frequency and time diversity are limited by communication resources and device complexity. Therefore, the application of spatial diversity in off-body channel is most commonly used and will be used in our work.

There are three main kinds of combination methods in the receiver, namely, MRC (Maximum Ratio Combination), EGC (Equal Gain Combination) and SC (Switch Combination). If the received signals of each branch are respectively $\{r_1, r_2, \cdots r_M\}$, then MRC means mixing the power of each branch at the weight of their ratio. The total received signal level is equivalent to:

$$R_{MRC} = \sqrt{r_1^2 + r_2^2 + \cdots + r_M^2} \tag{1.2}$$

The EGC is equivalent to combine each branch with the same weight value, and its overall output signal level is:

$$R_{EGC} = \frac{r_1 + r_2 + \cdots + r_M}{\sqrt{M}} \tag{1.3}$$

SC is equivalent to selecting only the strongest branch and discarding all the others. The overall output signal level is:

$$R_{SC} = max(r_1, r_2, \cdots, r_M) \tag{1.4}$$

In order to measure the effectiveness of practical diversity, the most commonly used index is diversity gain. Diversity Gain (DG) is defined as the improvement degree of the average received signal after combination compared with the mean original signal at a specific distribution probability level (generally 10% of the cumulative probability distribution). Theoretically, under the same conditions, DG of MRC is greater than that of EGC, and the DG of EGC is greater than that of SC. Of course, the implementation complexity is the opposite, MRC implementation complexity is much higher than EGC, and EGC is slightly higher than SC implementation complexity. In addition to DG, diversity order is also commonly used as a theoretical measure although its way of calculation is more complicated. Some literature reported some simple methods of quantitative definition of diversity order in specific scenarios, such as the literature [25, 26] mentioned the use of the square of the ratio between the channel matrix trace and the Frobenius function as diversity order under the condition of Rayleigh fading channel.

Table 1.3 shows the research status of channel diversity of off-body channels in some literatures in recent years. It can be found that the research for off-body spatial diversity is very active. In many scenarios like microwave dark room, interior walls, larger space, corridor and laboratory, a variety of extensive field measurement investigations are conducted. Multiple diversity combination methods are compared, and many factors influencing the off-body channel diversity are explored. The off-body frequency is mainly focused on UWB and some low frequency such as 868 MHz, and a small amount of ISM frequency band. Similar to the traditional spatial diversity, the spatial diversity of off-body channel is also deeply influenced by the combination method, the number of diversity branches, the correlation between branches and the line-of-sight state. However, there are also many obvious differences. Due to the influence of the human body, the diversity gain of the off-body channel is significantly affected by the motion, face direction and different wearing parts of a human. Meanwhile, different wearers, and the movement of adjacent people and different trajectory of nearby people also are shown to have a significant impact. At the same time, it is found that in different scenarios, even with the same number of branches and the same wearing position, off-body DG range is significantly larger than traditional DGs. Moreover, many papers have shown that even under the

Table 1.3: Research contents and conclusions of off-body channel diversity in some literatures

Cite	Scenario	Frequency	Body worn position	Number of branch	Diversity way	DG [dB]	Research highlights
[27]	Laboratory	3-10 GHz	Chest, head, wrist, ankle, back	2	MRC	9-14.4	The distance between wearable devices affects the diversity gain; NLOS diversity has larger gain
					EGC	8.1-11.8	
					SC	8-10.1	
[28]	Anechoic chamber, Open office, Corrider	868 MHz	Wrist, waist, left chest, shoulders (back side)	2, and 6	MRC	5.7-11.1	Signal distribution of different combination; And the specific distribution of LCR
					EGC	5.2-10.1	
					SC	4.4-6.9	
[29]	Complex lab., NLOS	3-10 GHz	Head, chest, waist, wrists	2 to 8	EGC	5.6-11	Custom diversity measure; It is suggested that a single person should arrange 5 diversity devices at most
[30]	Open offices	5.8 GHz	Waist both sides	2	SC	LOS: 0-3.9 NLOS: 0-4.1	Number of people and the trajectory of people have a significant effect on diversity gain
[31]	Anechoic chamber	2.45 GHz	Chest, wrist, thigh	2	EGC	9.1-14.9	Link correlation has a significant effect on diversity gain; When less correlation, double diversity can effectively combat the influence of multiple walking people
					SC	9.4-13.1	
[32]	Indoor NLOS lab.	3-10 GHz	Chest, head, wrist, ankle, back	2	MRC	9.1-14.9	Extend the study in [27] to the NLOS case, and find DG was significantly improved, correlation and power imbalance were significantly reduced
					EGC	9.4-13.1	
					SC	8.1-13.1	

same conditions, off-body DG fluctuates greatly in a wide range. These fluctuations from the cumulative effect of many influence factors in off-body channel, which are significantly different from traditional ones. This indicates that the diversity method and anti-fading improvement effect of off-body channel still need to be further explored.

The above are all the research results of linear polarization diversity reception, and many literatures have shown that polarization characteristics also have a significant impact on the diversity performance of off-body channels [8, 33–38]. It is found that dual polarization or circular polarization can effectively improve diversity efficiency in different frequency bands and multiple scenarios [39–42]. However, most of these researches have not carried out systematic studies on off-body diversity propagation characteristics and channel performance, and the comparison between linear and circular polarizations under the same conditions is also negelected. Literature [26] proposed a circular-polarized dual-diversity scheme deployed on two fire-fighters for body-to-body communication measurement. It is found that the dual-circular-polarized reception can effectively deal with various kinds of fading like NLOS, serious obstruction and strong interference source. At the same time, the performance of circular polarization diversity scheme is significantly improved by evaluating the bit error rate curves. The communication between a pair of circularly polarized antennas can be compared to the performance of linear polarized dual diversity in off-body channels.

In addition, in the application layer, many literatures have proposed other novel transmitting diversity schemes to improve the reliability and transmission efficiency of off-body channels [19, 34, 43–47]. Literature [48] proposed a method to improve off-body transmission capacity by using the transmission diversity of a macro- and micro- base station. Using the wide deployable area of human body surface, the channel reliability is enhanced by diversity, signal relay and cooperative communication. Similarly, reliable in off-body channels are of great significance for conducting off-body diversity research to promote fire protection, security, national defense and many fast-developing consumer electronics. Therefore, the off-body diversity anti-fading technologies have made great progress, but it is still of importance to further explore the selection/combination of anti-fading schemes and the insights of off-body diversity due to the complexity of off-body transmission and serious/high fading probability.

Anti-fading diversity measures of off-body channel are mainly faced with three challenges: 1) the performance of off-body diversity channel still needs to be further improved, especially the research on the influence of human height, human motion, polarization mismatch fading and circular polarization. 2) the physical layer design and theoretical exploration of off-body diversity measures need to be further promoted, including the determination of diversity number, wearing position, scene adaptability and anti-fading mechanism. 3) research needs to be done into the development of new off-body diversity methods. Some researches based on circular polarization, double polarization, MIMO and transmitting diversity between base stations provide good ideas. However, further research and verification are still needed and performance improvement in various scenes need to be estimated.

1.2.3 Off-body Sparsity Analysis

Due to the complex and changeable scenes of the off-body channel, which are affected by the posture, rotation direction and motion of the human body, the problem of "dimension disaster" is often encountered in the channel measurement, propagation analysis, algorithm design and system modeling. For example, literature [49] showed this problem occurring in the hospital beds environment under the typical measurement schemes of changing wearable positions. 7 volunteers are repeatly measured to avoid the influence of human individual differences. For each volunteer, measurement data of 10 wearable positions and 12 different AP heights need to be collected. For each measurement position or height, eight large-scale grids are planned and each grid contains 16 grid points with a λ (working wavelength) space between any 2 adjacent grid points to offset the impact of small-scale fading. Each grid is repeated five times for eliminating measurement bias. Each measured Impulse Response signal (CIR, Channel Impulse moisturiser Response) is combined by 801 uniform frequency sampling data. Thus, the amount of data for 1 measurement investigation is accumulated to more than 400 million ($7 \times 10 \times 12 \times 16 \times 8 \times 5 \times 801 = 430,617,600$). Such a large and growing amount of data brings great challenges to traditional methods of off-body channel analysis and modeling. With the fast development of off-body channel towards multi-channel, large-bandwidth and other high-dimensional signal technologies, "dimensional disaster problem" will be further highlighted [50–52].

Dimension disaster or dimension curse was first put forward by Richard E. Bellman when he studied dynamic programming in the 1960s. It mainly refers to a series of difficulties brought by data collection, organization and analysis due to the rapid increase of space capacity when the dimension of research objects rapidly increases [53, 54]. A widely used way to solve dimensional disasters is sparse representation (or feature representation) [55]. In wireless communication, the sparse representation method aims to find out the significant low-dimensional structural information hidden in the high-dimensional signal space. By means of the compression perception (CS, Compressive sensing) principle [56–58], the low dimensional structure can usually be expressed by the simple linear combination of a few dictionary atoms [59–62]. The following mainly describes its research status and challenges from two perspectives: the application principle of sparse expression in wireless communication and the key compressed sensing recovery algorithm in sparse approximation.

The application principle of sparse approximation in wireless communication

At present, several important steps of progress have been made by combining wireless communication and compression sensing based sparse approximation methods [62], such as channel estimation [63, 64], millimeter wave [65, 66], large-scale antenna system [66, 67] and high resolution angle spectrum recognition [68]. Literature [69] proposed a feasible pilot scheme design for downlink of large-scale MIMO systems based on CS. Similarly, literature [67, 70] proposed a kind of CS based pilot frequency design method for better estimating channel and obtaining channel feedback information. Literature [50, 52, 71] proposes a system framework to theoretically solve the design problems of millimeter wave based on parallel stream transmission and high demodulation broadband by using CS based sparse approximation theory.

The basic premise that these sparse expressions can be applied effectively in wireless communication is consistent, i.e., sparse structures (useful signals with low dimensions) commonly exist in high-dimensional wireless signals. Fig. 1.3 shows a schematic diagram of the sparse

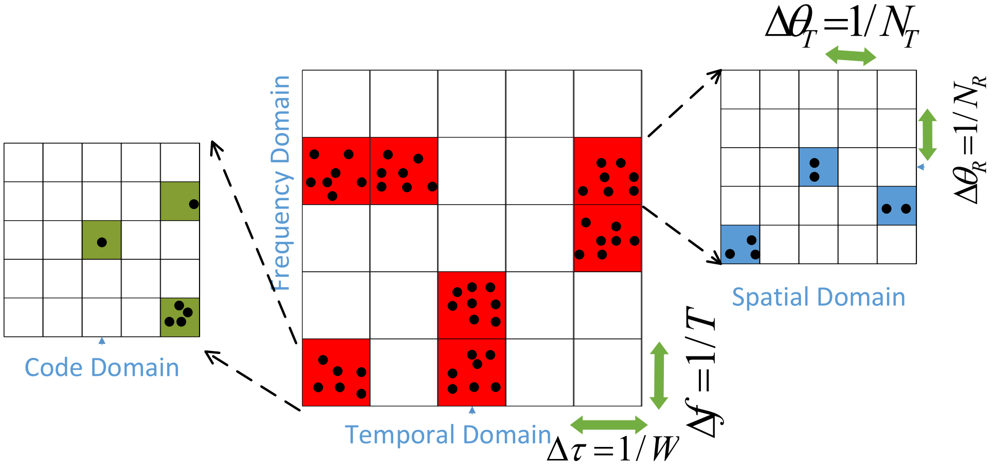

Figure 1.3: An example of channel sparse expression, although the overall dimension (number of all grids) of the channel is high, the actual effective signals in each dimension of the spatio-temporal, frequency or code domain are sparse, so the actual meaningful signal dimension (number of colored grids) is usually much smaller than the total signal dimension space. Sparsity represents the proportion of significant signals in the overall signal space. The sparsity of the examples in the figure is only 0.13%.

structure of a large dimensional channel in all dimensions of time, frequency, space and code domain. Temporal and frequency resolution are respectively $\triangle\tau$ and $\triangle f$. The number for transmitting and receiving antennas are N_T and N_R. The quantitative number of distinguishable grids of all four-dimensional channel matrixes in time, frequency and code domain are $P, Q\ and\ W$ respectively. Thus, the total resolvable degree is the product of resolvable grids of each dimension $D_{max} = N_T N_R PQW$. However, as the actual number of significant signals d is very limited in each dimension, the number of useful signal lattices is usually much smaller than the total distinguishable lattices of the large dimensional channel D_{max}.

Based on the traditional Nyquist sampling theory, uniform sampling at equal intervals is necessary to collect and store the signals completely, while the sparse representation method directly captures the signal parts we are interested in. For the complex scene of off-body transmission and the numerous influencing factors, the limited processing capacity of the wearable device itself is highly applicable [72–75]. Literature [72] proposed to use the sparse sampling principle to collect multi-channel physiological signals with wearable portable devices, so as to promote the originally expensive EEG and ECG devices to the field of home medical care with low consumption and cost. Similarly, literatures [73–75] also successfully designed a volume domain communication network with low energy consumption, high reliability and elastic expansion based on compression sensing.

Generally, there are three significant advantages after sparse representation. First, data volume is greatly reduced after sparse representation, which greatly saves transmission/saving/processing power. The second is to use compressed sensing technology to ensure the robustness of the recovery of the receiver. Thirdly, the amount of computation of the wearable device on the acquisition side is very small, and a large amount of computation takes place on the server side, which further saves the computing cost of the wearable side. These advantages promote the research of sparse representation of body area channel in many aspects. In literature [13, 76], some research on channel characteristics as research on algorithm and scene adaptability of off-body and on-body as well are presented. Literature [77] also takes advantages of the off-body channel model recommended by IEEE802.15.6 to prove the sparsity of off-body channel, and the compression sensing technology can significantly reduce the sampling rate requirements of off-body channel. However, most of these applications are based on WBAN simulation channel sets, while researches of sparse representation on measured data sets are rarely mentioned. Due to the complexity of propagation characteristics of the off-body channel, the recovery of the simulation channel from real channel set is still poor. It is urgent to analyze the sparse characteristics of the measured WBAN channel sets and select/improve the sparse recovery algorithm.

The key compressed sensing recovery algorithms

From the perspective of dimensional space, the rapid development of wireless communication in the recent 50 years is attributed to the deepening and refined utilization of wireless resources in frequency, time, code and space domain. Therefore, in high-dimensional wireless signal spaces, it is crucial to find, understand and characterize its low-dimensional characteristics. Sparse analysis provides a feasibility, and the key to its implementation lies in selecting and developing appropriate signal representation methods, especially suitable sparse recovery algorithms [51, 78]. For any sampled n-dimensional signal $y \in \mathbb{R}^n$, we can express the sparse signal vector of this channel as,

$$\begin{aligned} x_s &= arg\min_x ||x||_0 \\ s.t. \quad y &= \Phi\Psi x + r \end{aligned} \tag{1.5}$$

where, x_s is the sparse coefficient vector, $k = ||x||_0$ is the 0 order norm of sparse vector x, i.e., the number of non-zero variables of x. Generally, the required number k of non-zero coefficients is far less than the original vector dimension n, i.e., $k \ll n$. $\Phi \in \mathbb{R}$ $(m < n)$ is the measurement matrix (or sensing matrix), $\Psi \in \mathbb{R}^{n\times n}$ is the isometric transformation matrix, and r is the residual vector (used to express the error of noise or sparse approximation). This is the basic framework for solving the sparse representation problem based on compressed sensing, which can be further explored in references [79–81].

Table 1.4 presents 9 typical implementations of four main compression sensing recovery algorithms, and their main characteristics and implementation complexity are compared. It can be found that there are abundant alternative algorithm libraries with different complexity and implementation costs. Most of these algorithms, such as IHT and AMP, are optimized for specific scenarios, while many other algorithms have a general application scenario and maintain a balance between complexity with performance. An appropriate algorithm should be selected or designed according to the actual scenario, channel sparsity and other characteristics.

The sparsity representation in off-body channels is mainly faced with two challenges: 1) there is still a lack of further exploration on the sparsity of the measured real off-body channels. Furthermore, the sparsity is also affected by the wearing position, human shadow and body rotation etc. 2) Due to the limited computing power of wearable devices, the adaptive algorithm library of sparse representation is extremely limited, and it is a difficult problem to design an appropriate algorithm that well balances the accuracy and complexity. Specifically, research and verification of the dynamic relationship among accuracy, sparsity and algorithm complexity in sparse analysis should be carried out urgently according to practical application requirements.

Table 1.4: The main features and complexity of 9 algorithms of four main CS recovery algorithms

Algorithm category	Algorithm implementation	Algorithm features	Compution complexity
Greedy algorithms	OMP, orthogonal matching pursuit [82]; gOMP, general OMP [83]	Each iteration selects non-zero elements from large to small	$O(mnk)$ Usually the lowest complexity
	CoSaMp, compressed sampling matching pursuit [84]; SP, subspace pursuit [85]	Each round of iteration selects k non-zero candidate sets at one time, and updates candidate sets round by round	$O(mnkT)$, T is the actual number of iterations
	MMP, multipath matching pursuit [86]	Tree search algorithm is used to optimize the selection efficiency of atoms	Slightly higher than OMP alg. , and better performance
Convex optimization algorithms	BP, base pursuit [87]	Use $\ell 1$ regular method to constrain sparse approximation error, can achieve high precision	$O(m^2n^3)$
	Reweight Ł1 min. [88]	Sparse vector of last round is used as weights to optimize the next iteration	$O(m^2n^3T)$
Iterative algorithms	IHT iterative hard threshold method [89]	Repeating iteration threshold steps. Only has significant advantages in certain scenarios	$O(mnT)$
	AMP, approximation cell transfer method [90]	Compressed sensing algorithm derived from gaussian approximation is commonly used in information transmission	$O(mnT)$
Statistical sparse recovery algorithms	MAP algorithm with Laplace priori [91]	Laplacian distribution is used as the prior distribution of sparsity to estimate the maximum posterior probability of sparse vector	$O(m^2n^3)$
	SBL, sparse bayesian learning [92]; BCS, bayesian compressed sensing [93]	The sparsity of the sparse signal is the super parameter. The EM maximum expectation algorithm is used to find these super parameters iteratively	$O(n^3)$, Mainly limited by matrix inverse operation

1.2.4 Off-body Sparse Modeling

Time-domain wireless channel modeling, which characterizes the propagation of wireless signals, is typically based on the Tapped Delay Line (TDL) model [94–96] and its variants such as the cluster structured Saleh-Valenzuela (SV) model [97] and Clustered Delay Line (CDL) model [98]. The parameters of these models are described by statistical distributions, such as small-scale Rayleigh and Rician fading, exponential power delay profile (PDP), channel coherent time and bandwidth. Such models are simple and straightforward in structure, and they would provide clear physical interpretation for wireless signal propagation. However, some of the advantages may disappear for large-bandwidth channels. For example, there could be tens and even hundreds of resolvable multipath components in the latest 5G channel models [98, 99], where multipath components typically arrive in clusters. Although SV model and CDL model introduce cluster structure to better characterize such channels, their underlying base function is still the impulsive delta function. For such dense multipath channels, there are as many parameters as the number of channel types to be characterized for channel modeling, and to be estimated for channel estimation, using delta-function based channel models. This renders the TDL model and its variants ineffective for dense multipath channels.

A natural question to ask is whether we can develop an efficient channel model to represent such dense multipath channels in a more sparse and compact way. Compressive sensing (CS) [100, 101] provides an effective tool for both sparse channel modeling (SCM) and signal processing based on sparse channel models. However, it is surprising that most work has been focusing on the latter, while SCM, which should have been the basis for sparse signal processing, is somewhat neglected. In the past decade, there has been strong interest in applying CS techniques for sparse channel estimation [63, 102, 103] and for sparse channel coding [104–106]. These works assume that wireless channels are sparse and compressible, and hence less training signals at the transmitter and observations at the receiver can be used to obtain a complete estimation for the sparse channels. Such sparsity assumption, however, is not very well validated by practical SCM results. The channel sparsity for millimetre-wave channels has been validated by several channel models established from practically measured data [107, 108], particularly in the angular domain. However, for lower-frequency centimetre-wave channels, there are very limited reported results, validating the sparsity assumption – not even to mention detailed statistical analysis for the sparse channel parameters. One of the limited number of examples is [109], where a sparsity pattern expressed by virtual channel representation with the Fourier dictionary is proposed to model the double-selective fading multi-path channels, but the channel is not well developed.

The lack focus on SCM is probably linked to its unacknowledged importance. SCM, through disclosing the inherent channel sparse structure, can not only provide a potentially simpler method for channel simulation, but also provide a benefit to sparse channel estimation and coding directly. For example, SCM can demonstrate the sparsity and best dictionaries, and hence provide guidance to the training symbol design for channel estimation [103]; the statistics of parameters in sparse channel models can also be exploited for developing better channel estimation algorithms, as has been explored in [110]. SCM can also estimate the sparsity, which is a necessary knowledge required by many sparse reconstruction algorithms such as CoSaMP.

The challenges of off-body sparse modeling mainly focus on three aspects: 1) how to balance the dynamic relationships among the variable sparsity degree, sparse approximation accuracy and implementation complexity; 2) how to properly characterize the sparse characteristics of different scenes (such as different wearing parts, different posture) and different influences (such as body shielding/non-shielding), i.e. the selection of sparse indicating parameter group; 3) how to improve the performance of sparse channel modeling by using these off-body channel sparse features.

1.3 Overview of the Thesis and Contributions

In the last section, the research status of propagation characteristics and sparse modeling of off-body area is summarized, and some problems and challenges raised by propagation analysis and sparse modeling are proposed. Aiming at some of the problems which have high attention and need to be solved, this thesis carries out large amounts of field measurement activities according to the guidance of data engineering and data-inspired-research methodology and forms some important statistical analysis and modeling results, according to the propagation characteristics, spatial diversity, MIMO schemes and sparse representation characteristics of off-body channel. The whole thesis is divided into seven chapters, and its structural relationship is shown in Fig. 1.4.

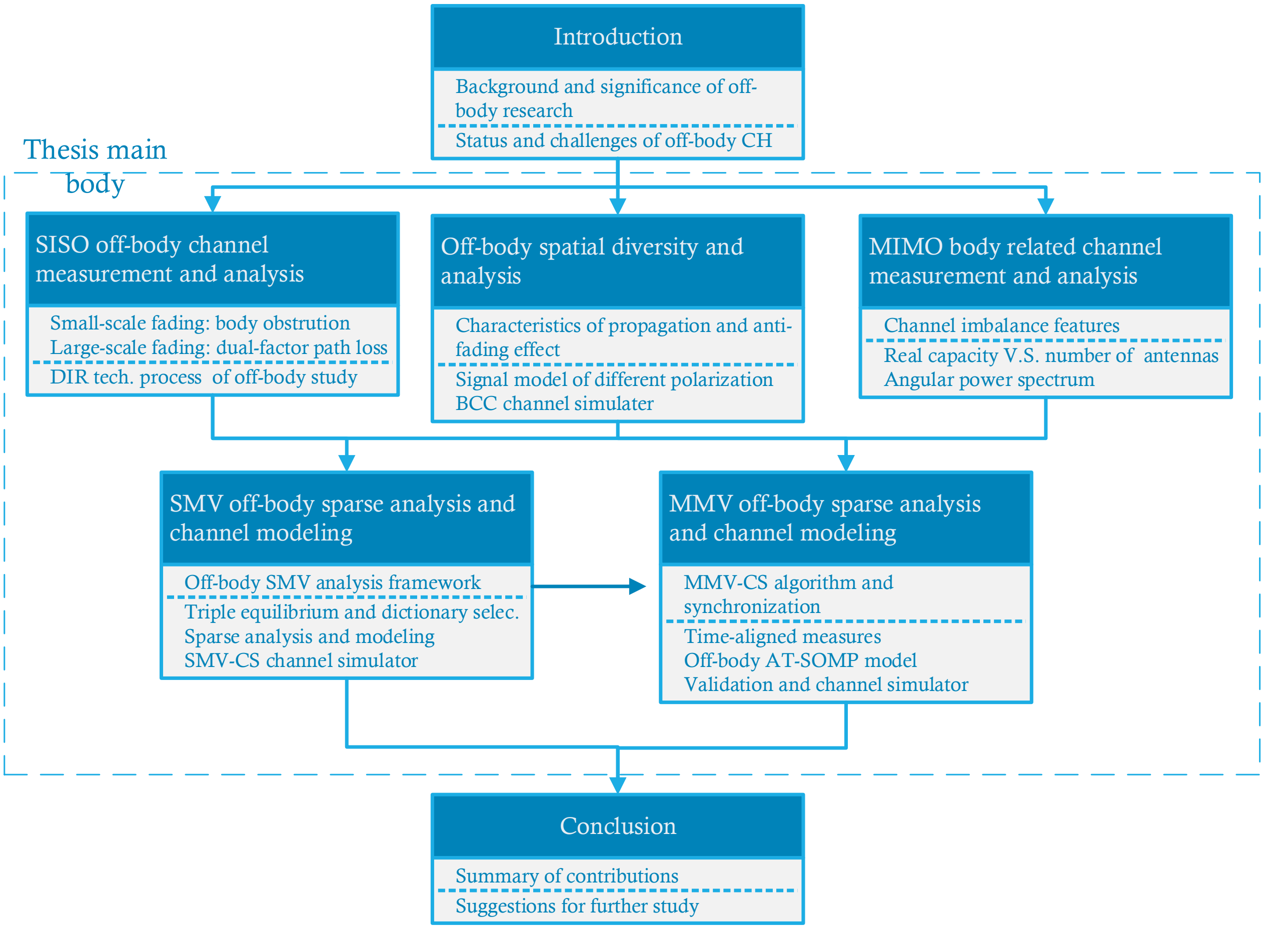

Figure 1.4: Chapter structure relationship of the thesis

The first chapter is the introduction. Firstly, the concept, theoretical significance and practical value of off-body channel research are introduced. Then, the research status and challenges in various fields of off-body channel research are summarized. Finally, we introduce the research methodology, main work and contributions of this thesis.

Chapter two to chapter six is the main part of the thesis. The second to fourth chapters are the basic research part of this thesis. The basic research of off-body channel is divided into three aspects: single input and single output channel (SISO), diversity channel (single input and multiple output, SIMO) and multiple input and multiple output channel (MIMO) for basic channel measurement, analysis and modeling. In chapter 5 and 6, aiming at the modeling problem of complex off-body channel and dimension disaster problem in basic research work, sparse modeling is carried out by introducing the compressed sensing method. Sparse channel modeling based on single measurement vector (SMV) and multiple measurement vector (MMV) is studied respectively in single channel and multi-channel.

In chapter 2, systematic measurement, analysis and modeling activities are carried out for multiple wearers with variable AP height and variable wearing position under both large/small scale fading conditions. This chapter focuses on the characteristics of large/small scale fading. In terms of large-scale characteristics, a dual-factor off-body channel path loss model is proposed, which is characterized by the path loss factor being modeled as a function of AP height, and the signal decay statistics parameters based on the position of wear are modeled as additional correction terms of path loss. This method has many advantages, such as clear physical insights, strong expansibility and stable model parameters with scene changes. In the aspect of small scale characteristics, the effects of body shadow on off-body channel are systematically compared from various small scale fading characteristics. Some fundamental reasons of serious small scale fading are verified. It is worth noting that research on measurement and modeling of off-body channel is essentially a data-inspired scientific research type (DIS). Based on the work of predecessors and their own experience, this chapter summarizes a set of general flow of channel measurement, analysis and modeling based on data engineering and feature selection method. In addition to guiding the research of in vitro channel, it is also useful for promoting many research projects based on high dimensional data sets.

In chapter 3, to deal with the serious fading in off-body channel, the circularly polarized spatial diversity method is proposed to enhance the channel reliability. Compared with two classical linear polarization schemes, the proposed scheme has obvious advantages of catabatic large/small scale fading and improved transmission performance . Further, by modeling the combined received signals of circularly and linearly polarized diversity, it is found that the cross polarization discrimination (XPD) factor and diversity gain of circular polarized diversity method can explain those advantages, and these advantages are further verified quantitatively by Monte Carlo simulation. Finally, the body centric network channel simulator is built to integrate the diversity propagation characteristics, the combined receiving signal model and the simulation module and present them to other researchers in a visual and easy to use way.

In chapter 4, to assess the effects of human obstruction and proximity on the channel in MIMO (and in the future massive MIMO) environments, practically measured channel dataset is collected using a 32x8 massive MIMO system in complex office environment. We classified all human-related scenes into 4 categories, with/without hand-held (mobile device with 2/4/8 antennas) and with/without body obstrution to systematically evaluate the influence of the presence of a static human body on MIMO channel. We introduce a parameter of Power Imbalance (PI) indices to estimate the wide-sense non-stationarity in multiple domains and another parameters of Channel Popularity Indices (CPI) to predict the popularity of MIMO channel.

Chapter 5 and chapter 6 solve the "dimensional disaster problem" in traditional off-body channel research by introducing the sparse analysis method based on compressed sensing. In chapter 5, a unified sparse analysis framework based on single measurement vector-compressed sensing (SMV-CS) is established, and triple equilibrium principles of channel sparsity, modeling accuracy and modeling complexity are established to guide the selection of dictionaries and algorithms for sparse analysis. Secondly, the proposed analysis framework is used to carry out sparse analysis on multiple measured and simulated channel sets of off-body channel. It is found that the average sparsity of measured off-body channel is about 20, and the optimal selection set, distribution characteristics of sparse vector and amplitude attenuation rule are analyzed in detail. Finally, a channel generation model based on SMV-CS method is established, and its advantages of high accuracy and low complexity over traditional STDL model are quantitatively verified. Then, the propagation characteristics and sparse channel model are condensed into a vivid and easy to operate sparse channel simulator for theoretical research and engineering reference.

In chapter 6, aiming at the analysis of high-dimensional off-body channel sets, the joint common sparse features of multiple parts and scenes are extracted from the perspective of multi-channel synchronous analysis. The analysis results in chapter 5 are successfully extended to the synchronous multi-channel scenario. Meanwhile, some measures such as wavelet de-noising and synchronization enhancement are adopted to improve the synchronization orthogonal matching pursuit algorithm, and the sparse statistical analysis of multi-channel scenes is carried out. The multi-channel model is established, and its accuracy is verified from the point of view of key small scale characteristics. The proposed scheme has many advantages, such as low implementation complexity, flexible expression of cluster characteristics.

The last chapter is the summary and prospects. The main work, research achievements and innovation points of measurement and sparse modeling of off-body channel are summarized.

Chapter 2

SISO Off-body Channel Measurement and Analysis

2.1 Introduction

The capacity boosting, ultra reliability and massive connectivity are key technologies of the 5G mobile communications. In order to accomplish these techniques, it is necessary to extend the future mobile communications to more frequency bands. It is pointed out that the international mobile telecommunication (IMT) has at least a 663 MHz spectrum deficit [111]. Whilst, the super high frequency (SHF) bands, especially the 5-10 GHz, provides a promising choice for such a frequency deficit. Further, the SHF band has great potential to realize the 5G key performance indicators, such as up to 1 GBps cell edge user data rate and 1000 times traffic density [112]. Thus, it is critical to fully investigate the propagation characteristics of the SHF band to provide robust wireless coverage and to develop robust physical layer transmission schemes.

People's increasing need to communicate at anytime and anywhere in 5G era has promoted the development of body-centric communication (BCC) as they allow for the integration of wearable and/or hand-held devices within the surrounding infrastructure [113]. According to the mutual position of the transmitter (Tx) and receiver (Rx) involved in the body-centric

Table 2.1: PARAMETERS OF MEASUREMENT SYSTEM

Parameter	Value
Center frequency	7.25 GHz
Bandwidth	2500 MHz
Frequency separation	3.125 MHz
Sweeping time	400 ms
Transmit power	0 dBm
Low noise amplifier	20 dB
Power amplifier	20 dB

transmission, it is possible to identify four communication scenarios: In-body, On-body, Off-body and Body-to-Body [114]. In these scenarios, the off-body scenario causes increasing attention in both academia and industry for the function of direct access to the Internet.

The off-body channel is characterized by on-body wearable devices access to remote Access Point (AP). The propagation characteristics of off-body channel are considered to be mainly dependent on four factors including the antenna body-worn locations [10], AP deployment [113], body posture (including both static and dynamic scenarios) [11, 113] and carrier frequency [12, 113, 115]. Compared to the widely reported off-body channel characteristics under walking and body-rotation states [10, 113], the propagation characteristics under lying state is rarely studied [116]. Since the successful application of height gain factor of Okumura model [117], a large number of AP height dependent path loss studies under cellular communications are reported [118, 119]. Although the IEEE 802.15 (Channel Model for Body Area Network (BAN) 8.2.10.B.A) views the impact of antenna height as the primary channel factor for off-body communication (body surface to external) [120], the impact of AP height on path loss exponent (PLE) in off-body channel is seldom studied. There are a large number of statistical analyses of different body-worn links and various body postures [10–12, 113, 115]. Nevertheless, few statistics are used to set up a synthetically path loss model. Thus, it is of critical concern for the BCC system to build an off-body path loss model which systematically takes body-worn locations, AP emplacement and statistical influences into consideration under lying state. Furthermore, it would be useful to describe the small scale fading features, such as time delay dispersion, multi-path components distributions, coherence bandwidth etc. [121, 122].

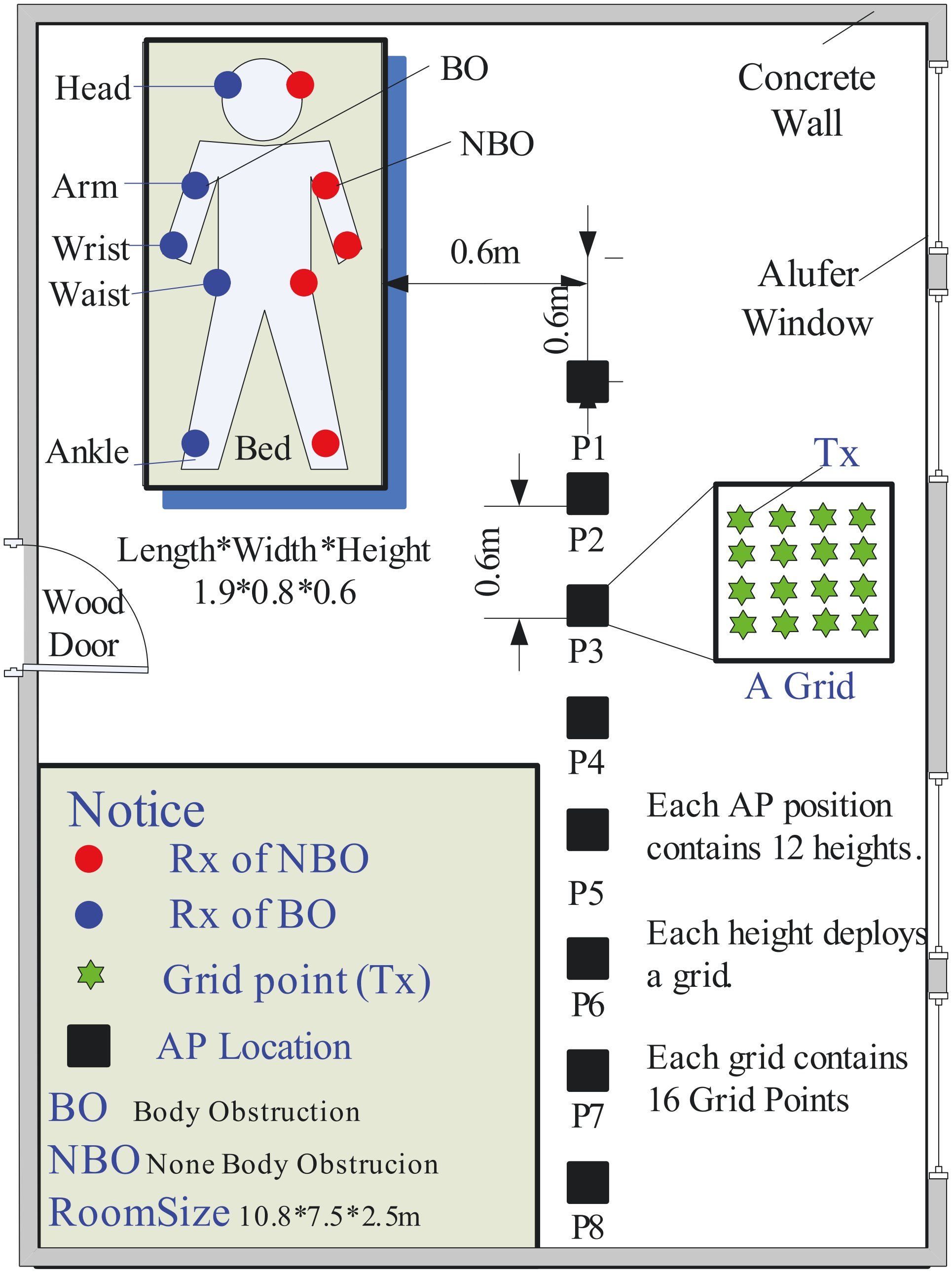

Figure 2.1: Illustration of the typical hospital scenario with definite measurement locations (External AP functions as Tx).

In this chapter, a novel off-body propagation model with a height-dependent PLE factor and a body obstruction (BO) factor is studied. Section II presents the measurement campaign. Section III depicts the details of the proposed dual-factor model. The experimental simulation and validation is introduced in Section IV. To the best of the authors' knowledge, this is the first path loss model that can describe the effects of variable antenna-height and body-worn-location deployments. As the dual factors provide clear physical insights into the transmitter and receiver conditions, the proposed model can be flexibly implemented in engineering and beneficial to the theoretical exploration. With the computer simulation, it exhibits higher accuracy than the conventional models.

2.2 Channel Measurement

2.2.1 Measurement Setup and Schemes

Measurement campaign is conducted in a typical less-furniture, hospital room environment shown in Fig. 2.1. An omnidirectional monopole antenna is used to emulate the external access point (AP) shown on the left in Fig. 2.2(a), and a wearable loop-dipole combined antenna worn on different positions of the volunteer is used to emulate the receiver (Rx) [123]. The measured radiation pattern of the wearable antenna is shown in Fig. 2.2(b) and Fig. 2.2(c) and the antenna gains are removed from the path loss during the data analysis. Due to the high cross-polarization of the RX antenna and the scattering around the lying body, the polarization mismatch has no significant effect on the signal measurement. A vector network analyzer (cf. VNA Agilent 8720) is used to generate a 0 dBm, 801-point sweeping signal with the frequency ranging from 6 to 8.5 GHz. The measured data are stored in a laptop computer via a general purpose interface bus (GPIB) interface. Table 2.1 shows the parameters for the measurement system and more details can be found in [124–127].

In order to study the influence of AP height and body-worn position on the off-body channel, two schemes are designed: In scheme I, the external AP is deployed to 12 variable heights to study the relationship between the large scale fading and different AP heights. In scheme II, the wearable antenna is disposed to ten primary on-body positions, including the left and right side of head, arm, wrist, waist, and ankle to explore attenuations caused by alerted antenna body-worn positions [128]. Small scale features like time dispersion and multipath for ten

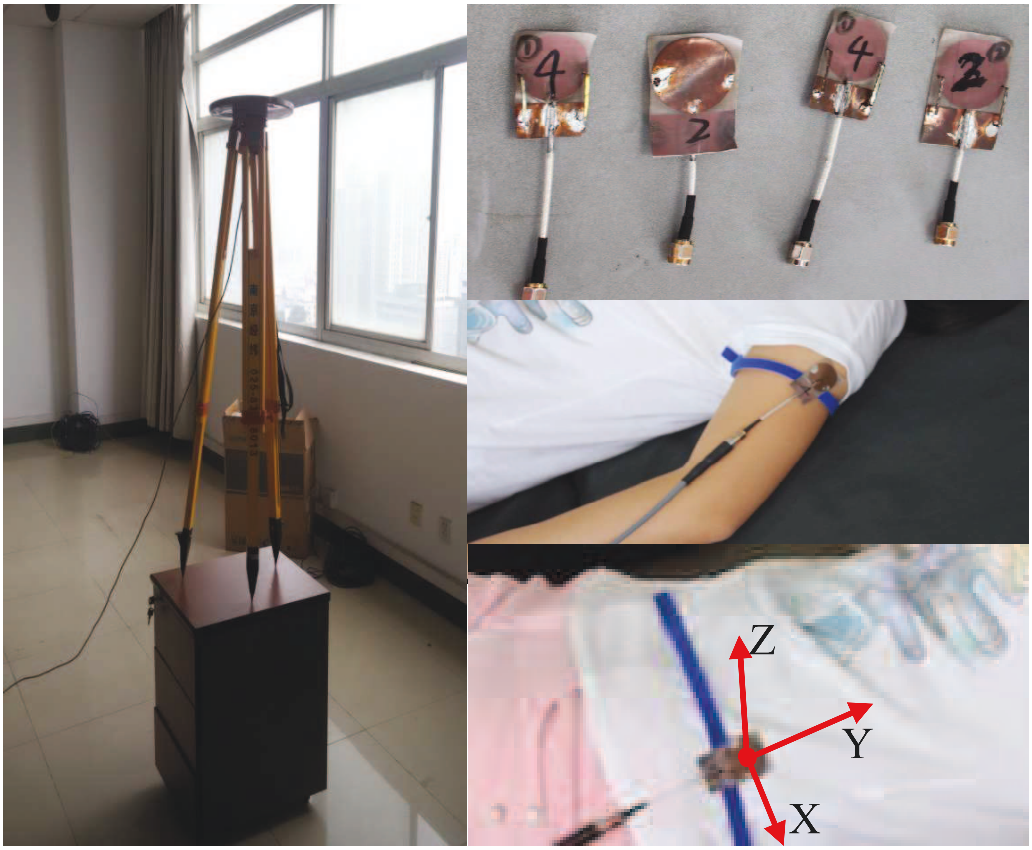

(a) External access point (left), wearable antenna (right top) and body-worn location (right middle and bottom).

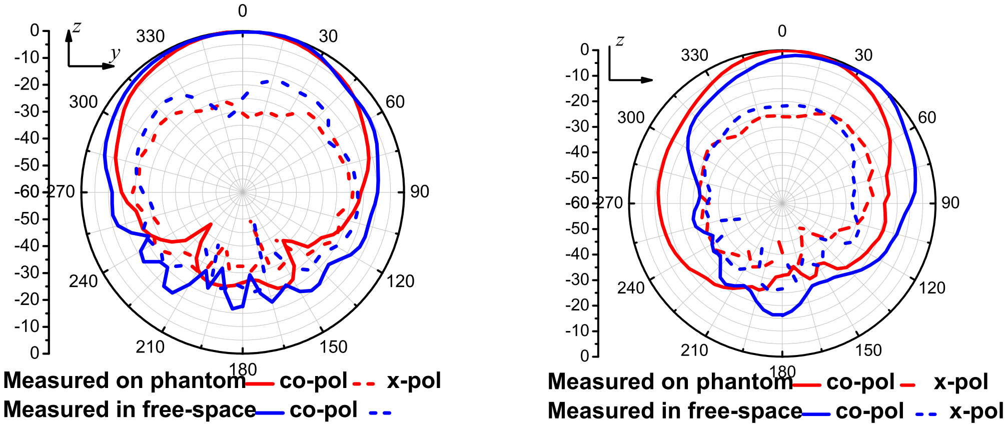

(b) E-plane

(c) H-plane

Figure 2.2: The illusion of (a) Real environment and equipment and radiation pattern for the wearable antenna in (b) E-plane and (c) H-plane.

antenna body-worn positions are further extracted to study the body obstruction effect. In the measurement, the volunteer keeps static. Therefore, the propagation channel under test is recognized as a non-time-variant channel so that its time dispersion characteristic can be measured by a VNA in frequency domain [129].

Scheme I: large scale scheme with variable AP height

When performing the height-dependent measurement campaign [124,125], the wearable antenna (Rx) is fixed on the left wrist of the volunteer. The AP mounted atop a wooden tripod is alternatively deployed at 12 heights between 0.4 and 1.9 m. For each acquisition run, the AP equipment is sequentially placed at eight locations ranging from 0.8 to 5.0 m. In each location, the area is divided into 16 different points (4ąÁ4 matrix points) using a 5-cm spacing, as shown in Fig. 2.1.

Scheme II: different antenna body-worn positions

Height of AP is fixed to 0.6 m, the same height as the hospital bed. To compare the BO and non-BO (NBO) effects, the wearable antenna is alternatively placed on five pairs of symmetrical on-body positions, i.e., the left and right side of head, arm, waist, wrist, and ankle in Fig. 2.1. Six volunteers are tested with different physical characteristics (height, weight, and gender). Another two AP height, 0.4 m and 1.9 m are also measured for validation and comparison.

For both schemes, the measurement of each location is repeated five times to eliminate noise.

2.2.2 Clarification on BO/NBO Left/Right and LOS/NLOS

Before channel modeling, three important concepts including NBO/BO, left/right side and Line Of Sight/ None Line Of Sight (LOS/NLOS) are illustrated to avoid possible confusion.

In our experiment, ten antenna body-worn positions are divided into two kinds of scenarios: BO and NBO. The former is defined that the direct link between wearable antenna and the AP is obstructed by human body, while the latter one is not.

For the off-body channel, BO is completely different from NLOS. LOS path between the AP and wearable antenna will not be completely blocked because the AP is higher than lying human in most BO cases. Similarly, NBO is not identical to the LOS scene, due to the complex antenna-body coupling effect, and the body shadowing effect that introducing extra attenuation. It is shown that the statistical signal level of the BO case is about 5dB larger than that of the NBO and the gap between BO and no body scene becomes even lager under the same emission conditions and environment [121].

As the direct link between AP and the wearable antenna on the left wrist in Fig. 2.1 is not obstructed by the volunteer in Scheme I, such scenario should be classified as the NBO case. However, if we take AP from the right side of the room to the left, the corresponding scenario would be changed, i.e., Scheme I would belong to the BO case. Thus, it is more convenient and reasonable to name such a scenario with the NBO wrist case than the traditional left wrist one.

2.3 Dual-factor Path loss Model

2.3.1 Proposed Dual-factor Path loss Model

Generally, average local path loss almost linearly increases with the logarithm of the Tx-Rx distance [37]. In order to describe the extra attenuation caused by the variations of the AP height and the antenna body-worn position, two factors are used to construct the proposed off-body path loss model. A height-dependent PLE factor is adopted to describe the influence of the AP height, and a body obstruction factor is added to describe the effects of different antenna body-worn positions. Then, the proposed novel dual-factor path loss model is represented by

$$PL(d) = PL(d_0) + 10N(h) \times log_{10}(\frac{d}{d_0}) + BOF + X_\delta \tag{1}$$

where the $PL(d)$ is the off-body path loss value at the Tx-Rx separation distance d, $PL(d_0)$ is the measured path loss at the reference distance d_0, the $N(h)$ is the AP height-dependent PLE factor. The BOF is the extra body obstruction factor which is dependent on specific antenna

Table 2.2: MEASUREMENT-BASED BODY OBSTRUCTION FACTOR UNDER HOSPITAL ENVIRONMENT

BOF [dB]	Different Antenna Body-Worn Positions				
	Ankle	Wrist	Waist	Arm	Head
NBO category	-2.4	0.0	-4.9	-0.4	1.5
BO category	5.4	0.1	3.4	5.1	5.3

body-worn position. The X_δ represents the shadowing effect which is a zero mean Gaussian random variable.

The contribution of increasing UWB frequency to path loss is not constant. Since the size of daily objects is similar to the wavelength of these frequency bands, the environmental impact exceeds the general rule that the higher the frequency band, the greater the attenuation will be. The path loss modeling of multiple UWB papers [13, 29] shows that the frequency loss contribution of this frequency band is similar and can be considered as a constant quantity.

2.3.2 Expression of AP Height-dependent PLE Factor

The AP height-dependent PLE factor is modeled as a quadratic function: [118]

$$N(h) = a \times h^2 + b \times h + c \tag{2}$$

where h represents the height of AP, const values a, b, c are three parameters of quadratic function which are dependent on the specific environment.

2.3.3 Description of the Body Obstruction Factor

Based on the statistical parameters of the measurement results in Scheme II, the body obstruction factor which is dependent on specific antenna body-worn position is added to modify the attenuation caused by the body obstruction. As the observed data of ten body-worn cases all fit the log-normal distribution well, the BOF is represented by the statistical mean parameter of the log-normal model. Table 2.2 shows the normalized measurement-based BOF values by subtracting the reference value (i.e., the NBO case with Rx on the left wrist).

The theoretical derivation for PLE factor and BO factor would be described in Section IV.

2.4 Modeling and Validation

2.4.1 Parameters for Proposed Path Loss Model

By averaging the complex frequency response data [130, 131], local path loss equation is calculated as following:

$$PL(d) = \frac{1}{MN}\sum_{i=1}^{M}\sum_{j=1}^{N}\left|H\left(f_i, t_j; d, h\right)\right|^2 - g_{ant}(\theta, \varphi) \tag{3}$$

where $H(f_i, t_j; d, h)$ is the complex signals at Tx-Rx separation distance d and the AP height h, $f_i(i = 1 \cdots M)$ is the observed M discrete frequency points, $t_j(j = 1 \cdots N)$ represents the N snapshots. The $g_{ant}(\theta, \varphi)$ is the antenna gain at elevational angle θ and azimuthal angel φ shown in Fig. 2.2(b) and Fig. 2.2(c). Two angels are calculated by $\theta = 2\pi - arcsin(\frac{d_{Bias}}{d_{ground}})$, $\varphi = 2\pi - arcsin(\frac{h}{d_{ground}})$ respectively, where the d_{ground} represents the horizontal distance between the wood stand and wearable antenna and d_{Bias} represents the shortest horizontal distance between the measured path and the wearable antenna.

The reference path loss $PL(d_0)$ is the initial path loss value at the reference distance $d_0 = 1$ m, including antenna gains. The PLE function $N(h)$ is first viewed as a constant n to evaluate the overall PLE parameter of the proposed off-body path loss model.

Table 2.3: BASIC PARAMETERS AND PATH LOSS EXPONENT FACTOR FUNCTION FOR PROPOSED PATH LOSS MODEL

Para-meter	BASIC PARAMETERS			PLE Function *N(h)*		
	$PL(d_0)$ $[dB]$	General *PLE*	X_δ $[dB]$	a	b	c
Value	48.6	2.36	2.4	1.33	-2.64	3.52

The measured 7,433,280 complex frequency response signals are fitted with the least square (LS) method. Fig. 2.3 shows recorded data and LS fitting path loss curve. The overall PLE $n = 2.361$, is comparable to the path loss exponents of typical indoor environment found by empirical, numerical and analytical methods reported in [132]. Fig. 2.4 shows the probability distribution of shadow variable. The shadow variable X_δ conforms to zero mean Gaussian distribution with a standard deviation of 2.42 dB, close to [133]. Table 2.3 summarizes the parameters of the proposed path loss model.

The result of the proposed model in Fig. 2.3 is superior to that of the free space model, exceeding about 2.1dB. However, because this is an intermediate local fitting process, the result parameters are not listed in detail for the sake of conciseness. Finally, a detailed comparison of MSE values is given by the multi-parameter model, which is more convincing.

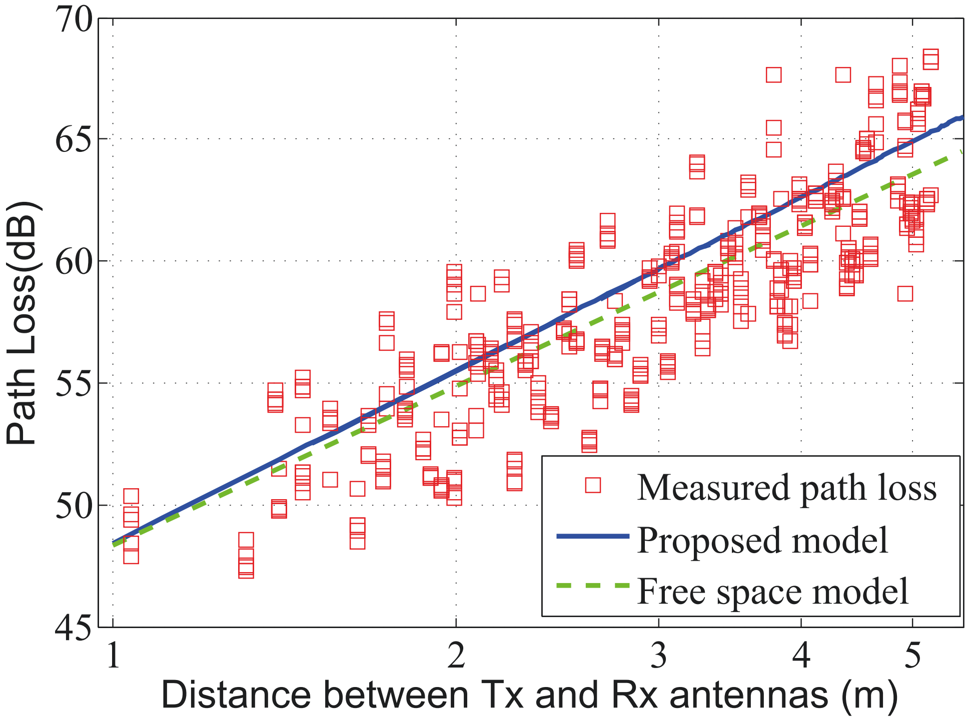

Figure 2.3: Scatter plots of the measured path loss values and the fitted curves.

These results show that the path loss model with the constant PLE fits well with the observed data. However, the AP height is proved to have a significant effect on the propagation prediction among various scenes [118, 119, 124, 125, 134], which are rarely report in BCC. The

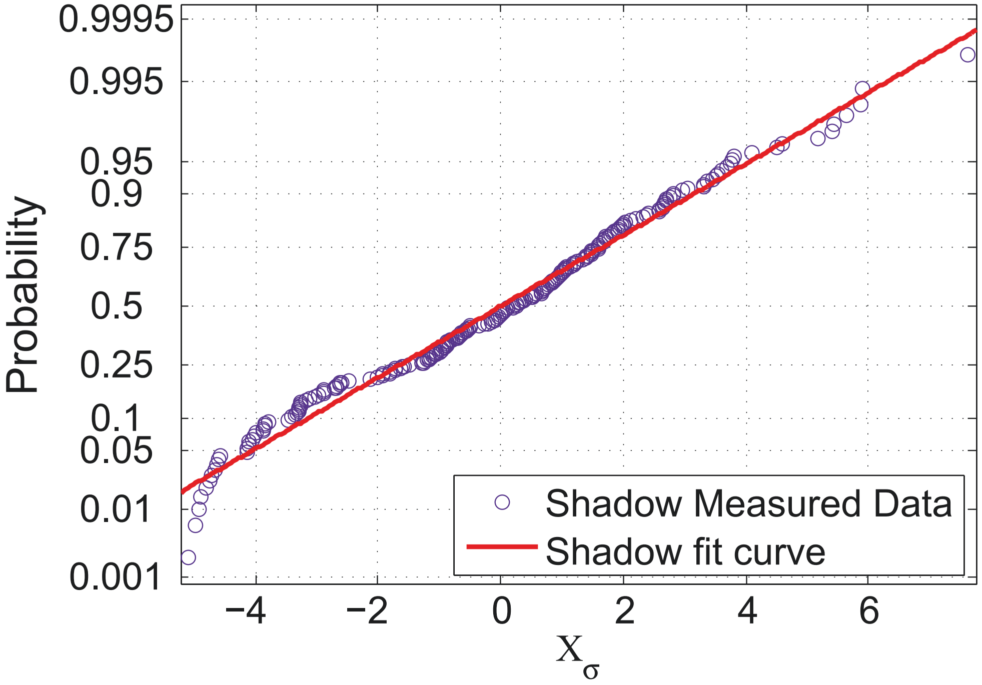

Figure 2.4: Probability plot of the shadow fading component X_δ in a typical bed-ward at 6-8.5 GHz.

channel model for BAN in [120] shows that when the height of Rx changes from 0.25 to 1 m, the path loss value increases by 6.4 dB (from 54.7 to 62.2 dB) at the frequency band of 7.25-8.5 GHz. Similarly, when Rx is elevated from 1 to 2 m, the path loss increases by 5 dB for LOS case and 15 dB for NLOS one under in stair environment [124, 125]. As both the above scenes are measured with the Tx and Rx placed on wooden stand, the impact of height variation will be greater if the antenna is worn on human body. Thus, the height relevant studies are expected to further improve the predictive accuracy.

2.4.2 Fitting and Validity for PLE Factor

Fig. 2.5 shows five fitted path loss curves with different AP heights by the log-distance path loss model. It is clearly seen that the path loss is height-dependent. It is also supported by the improved 30 percent of the maximum likelihood values (MLH) during the path loss fitting performance using the definite AP height observations other than the mixed height data.

Fig. 2.6 shows the fitted quadratic curve and the observed PLE values. The least square estimation approach and different functions, including power functions, logarithmic function and exponential function etc., are employed to model the path loss. It is found the quadratic function exhibits the best fitting performance. Table 2.3 lists the parameters for PLE function (2).

The parabolic function of PLE, which is indeed a very interesting discovery, has been observed in many of our observation LabS, and both practical and theoretical analysis support its good universality. Theoretical analysis also finds that this is true for non too small space structures (waveguide effects cause slower attenuation of power, such as narrow closed corridors). Part of the theoretical analysis also explains the cause of sag, which provides a certain basis for its universality.

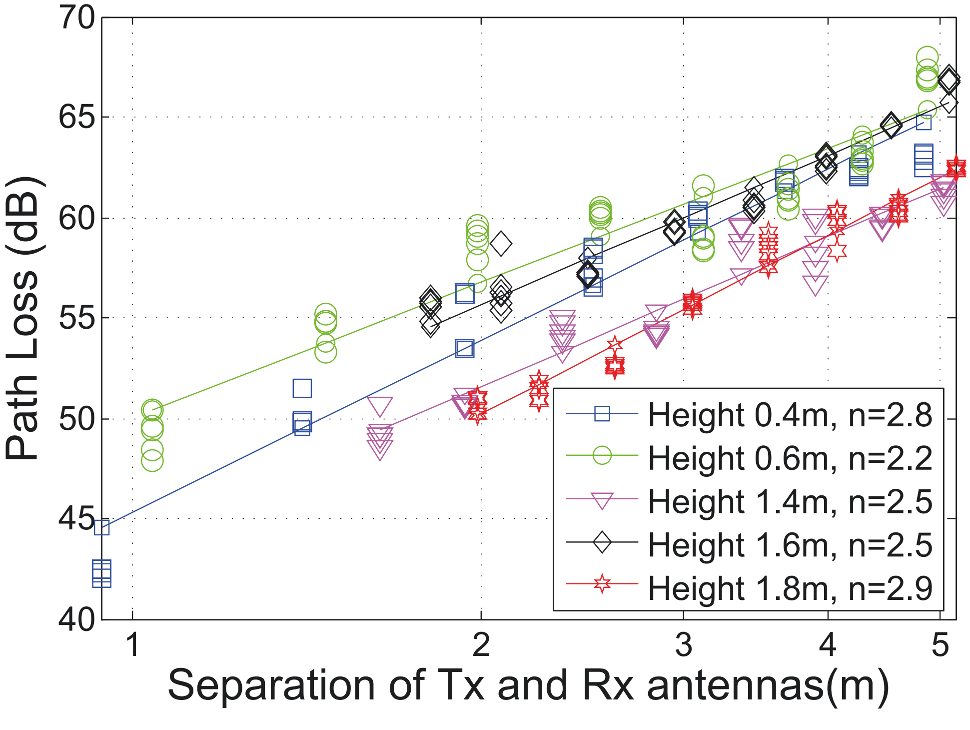

Figure 2.5: Comparison of five fitted path loss curves at different AP heights and their distinctive PLE values.

The well fit of the quadratic function on the height-dependent PLE factor *N(h)* can be explained by the two-ray model and quasi free space propagation in specific indoor environment

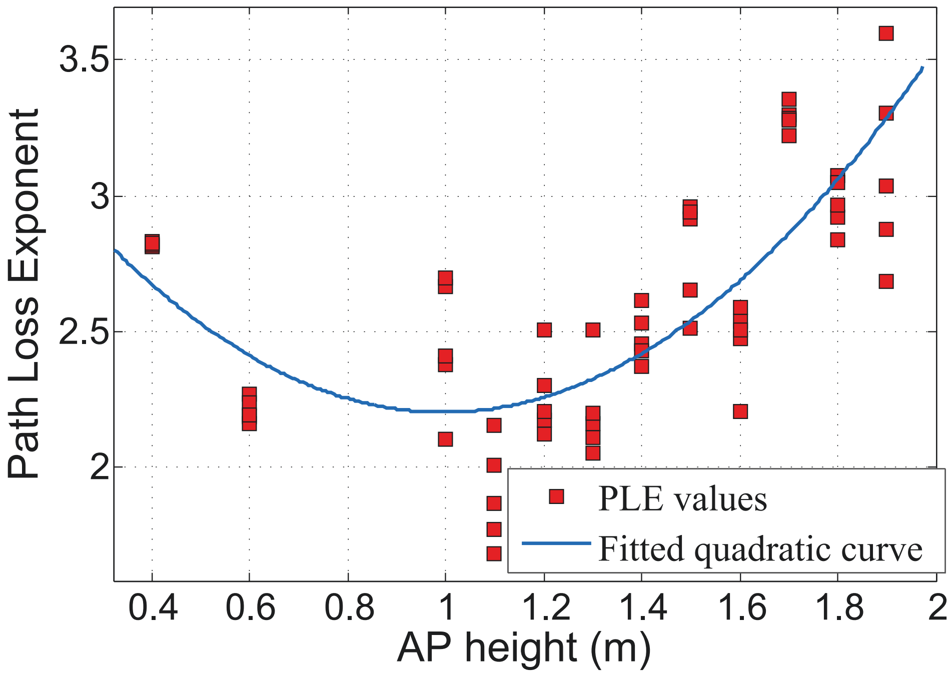

Figure 2.6: The PLE factor values at various AP heights and the best fitted quadratic function.

from the respects of the PLE bonds [118, 119]. The two-ray model reaches the maximum PLE value, when the distance between Tx and Rx antennas d is far enough shown as:

$$d \gg \sqrt{h_t h_r} \tag{4}$$

where h_t and h_r separately represent the heights of Tx and Rx [117]. Then, the path loss model will be simplified to:

$$PL_{two-ray}(d) = 40log_{10}(d) - 20log_{10}(h_t h_r) \tag{5}$$

where $PL_{two-ray}(d)$ is the path loss value of two ray model at distance d. Equation (5) shows the upper bound of PLE values for the two-ray model, i.e., PLE $n = 4$.

Fig. 2.7 shows the cross-sectional view of the AP height-dependent PLE factor under the hospital environment. The left part shows four AP locations at different heights and the same Tx-Rx separation distance $d = 5$ m. The four access points (APs) are the locations near the floor (i.e., Tx1), at the same height with bed (i.e., Tx2), in the middle of the room (i.e., Tx3), and close to the ceiling (i.e., Tx4). The coordinate axes on the right part of Fig. 2.7 shows a

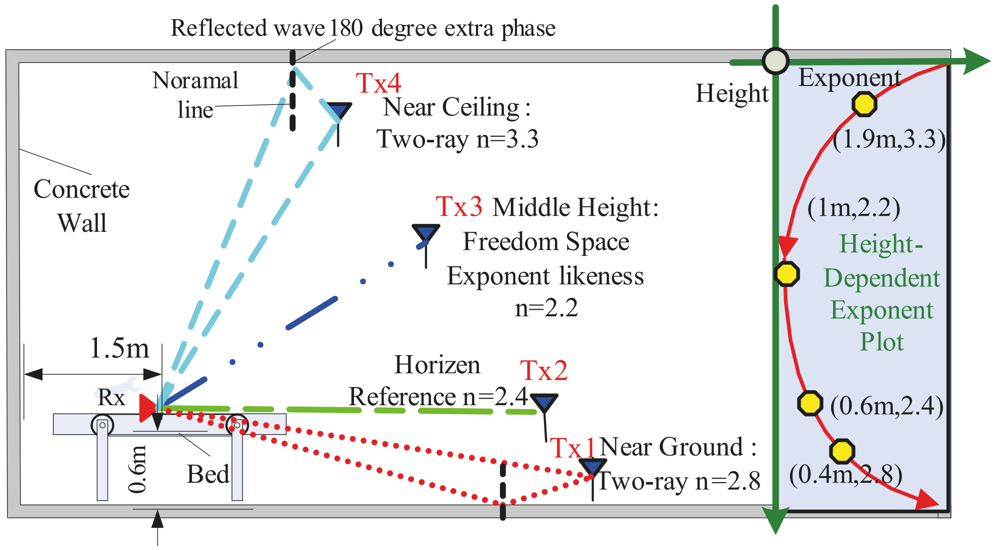

Figure 2.7: Cross-sectional view of AP height-dependent PLE factor and corresponding quadratic path loss exponent function.

quadratic PLE curve corresponding to the indoor AP height. Four circles in the PLE-height curve in the right part separately represent the specific PLE values of four APs on the left.

For Tx3 and Tx2 in Fig. 2.7, the PLEs of middle heights can be approximately explained by free space propagation PLE $n = 2$. The reflected components are much weaker than the direct ray, as the AP for Tx3 at the centre of the room is far away from the ground, ceiling and walls. For the APs like Tx2 around the bed-height, the shortest reflected path is blocked by the iron bed and the lying human body. This weakens the power of the reflected waves to 8-10dB less than the direct path in real measurement, similar to the UWB bed-shadowing report in [135]. The strongest direct path dominates the propagation characteristic in the moderate-height cases. As a result, the values of PLE are approximate to 2.

For Tx4, the PLE values of APs near the ceiling could be validated by the two-ray model. According to the two-ray model, in both cases the reflected ray has the almost same magnitude but the opposite phase with the direct ray [117]. Thus, the direct ray tends to be greatly weakened by the reflected ray in these cases. PLEs for Tx4 is 3.3, close to the upper bound PLE $n = 4$ in two-ray model (5).

Different from other APs which are higher than the bed, both the direct path and reflected

Table 2.4: Comparison of various path loss models among mathematical express and goodness of fit

Model cases		Mathematical express	RMSE
Overall	All data	$PL_0 + 10nlog_{10}(d/d_0)$	2.72
Height divided Models	Height 0.4m	$PL_0 + 10nlog_{10}(d/d_0)$	1.63
	Height 0.6m		1.79
	Height 1.4m		1.62
	Height 1.6m		1.08
	Height 1.8m		1.44
Height dependent Models	log-distance height gain model	$PL_0 + 10nlog_{10}(d/d_0) + alog_{10}(h/b)$	2.45
	Proposed model	$PL_0 + 10(ah^2 + bh + c)log_{10}(d/d_0)$	2.26

waves of AP at Tx1 are greatly weakened by the iron bed and the lying body. There is less offset between direct path and shortest reflected wave, while abundant surface waves around the body makes the PLE slightly fluctuate among 2.4-2.8. Thus, PLE values are expected to mainly fluctuate between 2 and 4. PLE $n = 2$ is obtained under the free space fading and PLE $n = 4$ is the upper bound for two-ray model. This is in agreement with the observed PLE values and the fitted curve in Fig. 2.6 which range from 2.0 to 3.5. Due to the strong interference from the nearby reflectors, the PLE for the top or low Tx is greater than the medium height one under the same receiving conditions.

The analysis above implies that the quadratic fitting curve of PLE factor $N(h)$ is explained by the two-ray model and free space theory from the perspectives of symmetry and boundaries, especially when the APs are higher than the bed.

Fig. 2.8 shows the fitting surface of the two path loss models. As observed, it is clearly demonstrated that the proposed model exhibits better fitting performance than the conventional log-distance height gain factor model with model shown in Table 2.4. The parameters for log-distance height gain model are PLE $n = 2.42$, $a =$ -2.48 and $b = 4.47$. The deviation between the measured PLEs and predicted values by the proposed model is smaller than 2 dB, while the deviation between the measured PLEs and predicted values with log-distance model rise

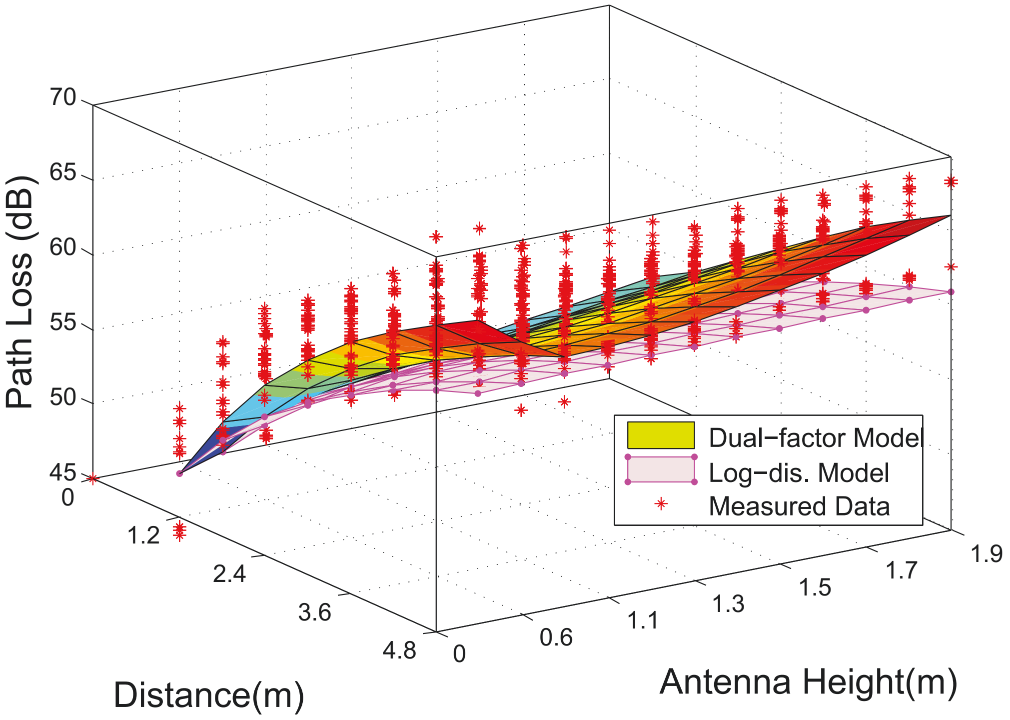

Figure 2.8: The simulation for the proposed height-dependent path loss model on the left wrist under the NBO case.

dramatically to more than 7 dB as the AP height and Tx-Rx distance increase. In this way, the accuracy of the dual-factor off-body model is both numerically and experimentally validated, and its novelty and effectiveness is also convinced.

In order to identify the appropriate path loss models for application, three kinds of models where evaluated in terms of root mean square errors (RMSE) are shown in Table 2.4. PL0 represents the reference path loss equivalent to PL(d_0) and the fitted curves for three models are shown in Fig.2.3, Fig. 2.5 and Fig. 2.9. The root mean square of the differences between observed and predicted data sets is a meaningful measure of the error shown as:

$$RMSE = \sqrt{\frac{\sum_{i=1}^{n}(X_{obs,i} - X_{model,i})^2}{n}} \tag{6}$$

where $X_{obs,i}$ and $X_{model,i}$ are the observed and predicted values respectively. The number of two data sets are both n.The biggest RMSE value is with the overall (i.e. height-mixed) model while the most accurate kind of model is height divided modes with RMSE less than 1.5. However, this kind of models has an obvious shortcoming that repeated measurement and fitting are needed whenever the the AP height changes. Thus, the unified model (e.g. the height-dependent models) that takes the height factor into consideration is developed for convenience in application and link evaluation at the cost of prediction accuracy. Both the two height dependent models have 3 fitting parameters and their accuracies are better than overall model while inferior to height divided models from the perspective of RMSEs.

The proposed height-dependent PLE factor model is chosen mainly for three reasons. First, the constant PLE in the log-distance model is not reasonable when comparing to the fitted curves of height divided models with PLEs ranging from 2.2-2.9. In contrast, the PLE factor in the proposed model varies with the AP height. Second, in the BCC or body area network (BAN), the studies for PLE in different height not only improve the predictive accuracy but also provide more physical insight for AP deployment and system-level simulation. For tens or hundreds of APs in the future off-body communication, it is meaningful to reduce the power of APs with small PLE at the optimized height to reduce possible mutual interference. Last but not least, there are increasing modified attenuation factors for path loss model in off-body communication due to the body shadowing and antenna-body effect. Thus, it will benefit the extraction and analysis of body related attenuation factors to put those intrinsic parameters (e.g. height) into intrinsic part PLE.

The theoretical analysis and numerical simulation of PLEs imply that the novel off-body PLE factor is well characterized by the AP-height-dependent quadratic function.

2.4.3 Effect of Antenna Mismatch

As the polarization alignment between the Tx-Rx antennas is easy to be changed in off-body communication (e.g. the subject's small deflection, slight wrinkle of textile antennas and Tx-Rx inclination), the analysis of Tx and Rx mismatch on the accuracy of path loss model validation experience is very important. Figure 2.9 shows the Path loss fitted curves for measured case without polarization mismatch, Rx polarization direction changed and Tx polarization direction changed cases at the Tx height of 1 m and Rx worn on the left wrist. Under the same conditions, the PLEs over three scenes are all around 2.5. It seems that the polarization mismatch has no significant effect on the PLE values.

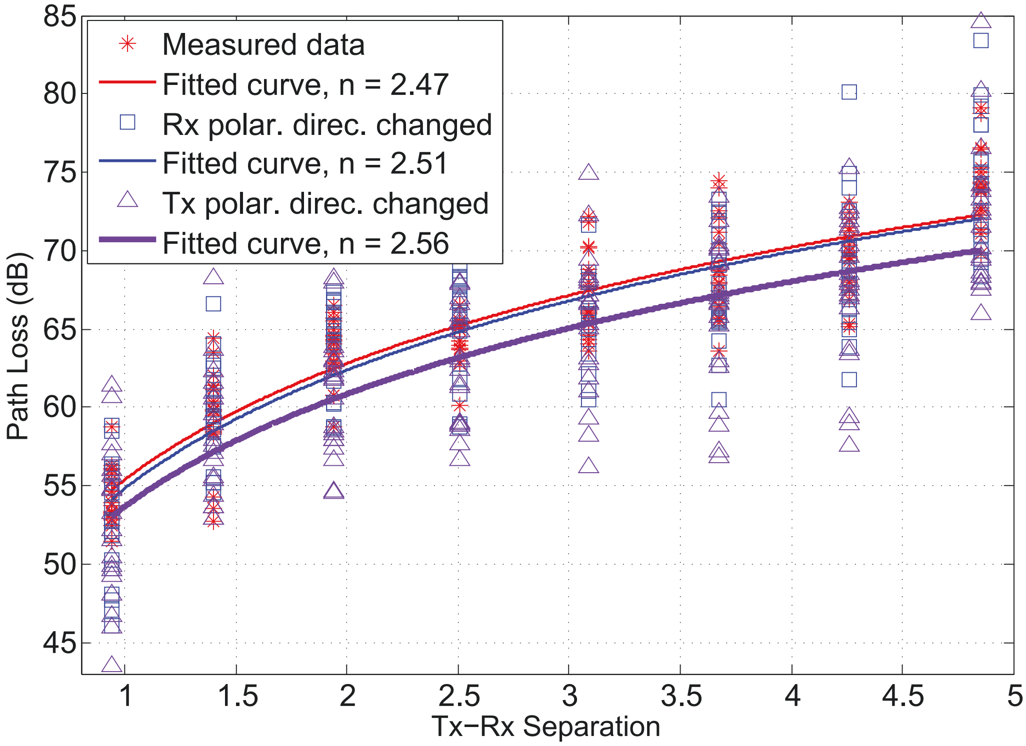

Figure 2.9: The Path loss fitted curves for measured case without polarization mismatch, Rx polarization direction changed and Tx polarization direction changed cases at the Tx height of 1 m and Rx worn on the left wrist.

There are three main reasons. First, the dipole wideband wearable antennas adopted in this work have high cross polarization levels shown in Fig. 2.2(b) and Fig. 2.2(c). On one hand, the cross polarization components for dipole antenna are strong, as the cross polarized direction is perpendicular to the co-polarized direction shown in following figure (not included in the paper). On the other hand, the cross polarization level for the wideband antennas is general high (see Fig. 4-6 in [136]). Thus, the Rx can receive signals with cross polarized components. Second, the multipath components are complex under the indoor environment especially for off-body communication. Meanwhile, the polarization direction for the multipath components can be arbitrary [137]. Last but not least, the antennas for mobile applications are characterized by high cross polarized components (see Fig. 12-13 in [138]) to guarantee that Users can receive signals in any polarized direction. Thus, the possible fading caused by polarization mismatch is made up by the high cross polarization of Rx and the complex multipath environment can provide an explanation.

2.4.4 Modeling and Validation of BO Factor

Fig. 2.10 shows the systematic simulated surfaces of the dual-factor path loss base on the height-dependent path loss model in Fig. 2.9. The fitting path loss surfaces under BO cases are evidently higher than the NBO ones while the disparity among the NBO path loss surfaces (about 8 dB) are larger than the difference among the BO cases (about 3dB). It is seen that the introduction of the BO factor will further improve the accuracy of the proposed height-dependent model. For example, the dual-factor model provides 8 accurate path loss values (60-67 dB for NBO cases and 68-70 for BO cases) for different body-worn parts while the traditional log-distance model in Fig. 2.9 provide only 58 dB (63dB provided by the height-dependent model) for general conditions with the same AP height of 1.9 m and Tx-Rx separation of 3.6 m.

Fig. 2.11 shows the cumulative probability distribution (CDF) of ten typical body-worn positions, i.e., head, arm, wrist, waist and ankle under the BO and NBO cases. The path loss values of BO cases are generally 3 to 5 dB higher than the NBO ones due to the obstruction of human body [121]. Except for the wrist position, the other path loss CDF curves for BO cases gather a cluster and the path loss values generally increased by about 3dB compared to the NBO cases. Eighty percent of measured data under NBO cases ranges from 55 to 75 dB, while the BO cases are between 65 and 80 dB. In the aforementioned example, the interval from 60 to 70 dB clusters the most observed data which proves the accurate prediction of the dual-factor model. As the wide range of the path loss distribution and the evident distinctions between BO and NBO cases, it is reasonable to depict ten scenarios with statistical parameters.

Fig. 2.10 and Fig. 2.11 show that from the perspective of link stability, wrist is the best body-worn position as the dissimilarity between NBO and BO cases is slight. Whilst, the

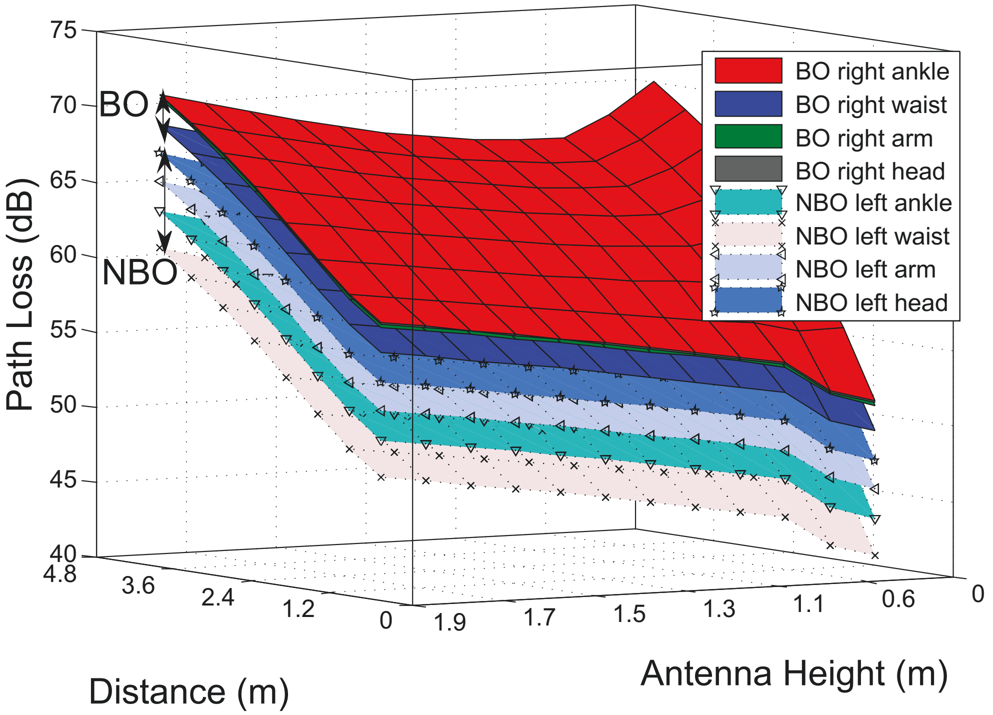

Figure 2.10: The simulation for the proposed dual-factor path loss model (The top four surfaces for BO cases and the others for the BO).

strongest signal level case is the waist position under the NBO case despite the BO case for such position has an average of 8 dB signal drops.

Table 2.5 tabulates the log-normal distribution of path loss values for the proposed ten body-worn positions using maximum likelihood estimation (MLE) method. The MLEs and small deviation imply that the log-normal distribution depicts the off-body signal level well.

From the measured and fitted six parameters, i.e., log-normal fit of the signal level, root mean square (RMS) delay spread, mean delay, multi-path and coherent bandwidth with the method reported in [127], it is found that there are obvious differences among parameters of different body-worn positions and noticeable gaps between BO and NBO cases. For example, the multi-path parameters range from 75 main components to 139 for 5 body-worn parts under NBO situation and the components for NBO situation double the number for BO cases. The creeping waves around human body and reflections from torso and surroundings provide an explanation for the differences between BO and NBO cases [139, 140]. Thus, it is necessary to

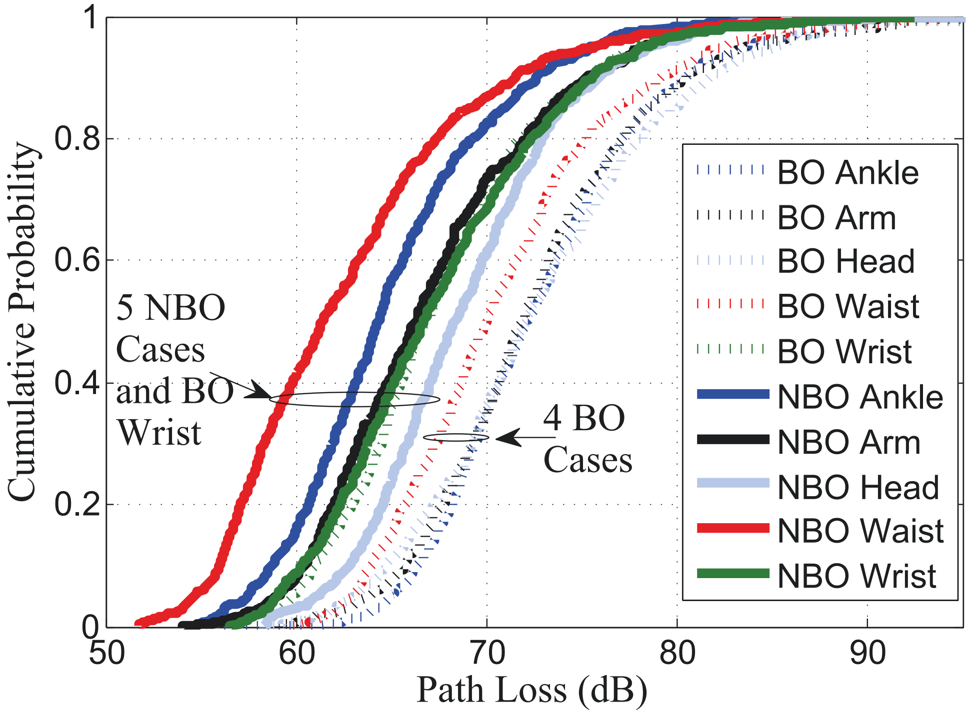

Figure 2.11: Comparison of measured path loss data under both NBO and BO cases with the Tx-Rx separation is 3.6 m and the height of AP is 1.9 m.

introduce the BO factor to discriminate the BO and NBO cases caused by the body obstruction effect.

The analysis above implies that it is of great flexibility and accuracy to predict the path loss values under the off-body channel to introduce the BO factor dependent on the body-worn position and the PLE factor dependent on the AP height.

2.5 Summary of data inspired research idea in off-body measurement

The analysis and modeling research of the off-body characteristics is essentially a kind of data inspired research, i.e., solving the problem of data collection, organization and analysis modeling in specific area[134][135]. In order to deal with the complex situation of multi-scenario, multi-influence-factor, multi-application demand and rapid growth of off-body data dimension. To

Table 2.5: COMPARISON OF PARAMETERS ON DIFFERENT BODY PARTS (TX-RX DISTANCE is 3.06m. S_{REC} IS RECEIVED SIGNAL LEVEL AND B_W IS 3DB COHERENCE BANDWIDTH.)

Cases	Body-worn position	LogNorm. Fit S_{Rec}		RMS [ns]	Mean Delay [ns]	♯ of Multipath	B_W [MHz]
		Exp(μ)	σ				
NBO	Ankle	64.9	0.08	6.93	16.4	108	21.9
	Wrist	67.3	0.09	6.16	14.6	100	76.6
	Waist	62.4	0.10	5.32	13.8	80	58.3
	Arm	66.9	0.09	6.04	17.8	139	32.9
	Head	68.8	0.08	0.77	9.79	75	90.5
BO	Ankle	72.7	0.08	6.98	20.97	260	18.9
	Wrist	67.4	0.09	6.68	17.43	169	18.9
	Waist	70.7	0.08	4.97	19.31	307	14.6
	Arm	72.4	0.09	5.10	22.93	212	24.8
	Head	72.6	0.09	17.29	29.02	435	8.1

avoid the dilemma of a blind man sensing the elephant, it is necessary for scientific research workers to use scientific methods to summarize problems, set up measurement, analyze key features and systematically sort out the modeling process, so as to improve efficiency and avoid falling into the trap of local rules. According to the basic principles of data science and feature engineering [136][137][138], Fig. 2.12 shows the main methods and processes of data collection, organization and analysis modeling adopted in this study.

2.6 Conclusion

In this chapter, a novel statistical path loss model with an AP height-dependent factor and a BO attenuation factor for off-body channel under hospital environment at 6-8.5GHz is developed and validated. The proposed model can provide not only the accurate off-body propagation prediction, but also the beneficial reference for the best antenna-height and body-worn-location deployment. Compared to the traditional log-distance path loss model, the proposed dual-factor model is observed an improvement of as high as 7dB under the condition of high AP deployment. In addition, the proposed model can be easily implemented in engineering and

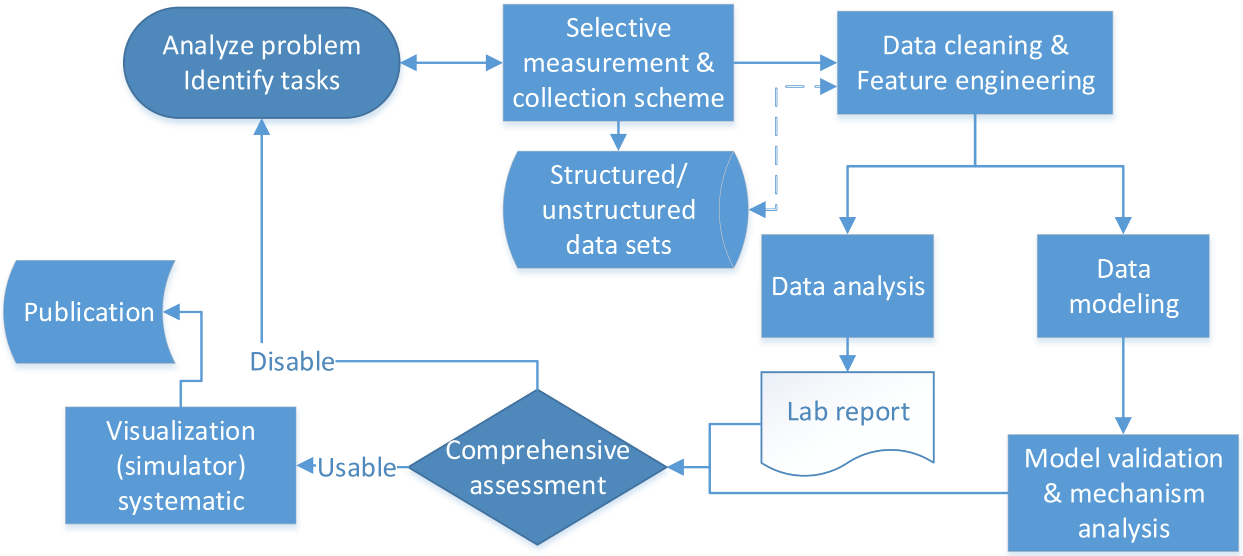

Figure 2.12: Research plan and flow chart of data inspired research in measurement practice

extended to other height-related scenarios, due to its clear physical insights of the two factors. Therefore, it is a promising candidate model in future developments of novel physical layer transmission schemes in the BCC systems.

As large amounts of electronic devices which have a high link reliability and stringent electromagnetic safety requirement have been employed in the hospital environment, our future work will focus on the challenging problems of multi-device coexistence and reliable off-body communication links.

Chapter 3

Off-body Spatial Diversity and Analysis

3.1 Introduction

The fading caused by the intervention of human body widely exists in the off-body communication [141]. Although the body-part, body-posture and body-rotation dependent fading has been extensively evaluated and modeled [142–145], the study for body-height dependent fading caused by posture variation (e.g. standing to sitting or squat) is rarely reported. As the antenna height has significant effect on the indoor communication [146, 147], it is essential to evaluate and reduce such fading effect to guarantee the robustness of off-body communication.

One common method is by employing spatial diversity at the receiver [144, 145]. This may not work well on reducing the body-height dependent fading for the complex multipath components (MPC) during the human height changes. The polarization misalignment fading caused by body deflection, wrinkled wearable antennas and reflections from circumstance further reduce the effectiveness of typical LP diversity scheme [148]. One potential method is the use of Circular Polarized (CP) antennas [149, 150]. Thus, a novel CP spatial-diversity reception method is proposed for reducing the aforementioned height-dependent and polarization misalignment fading. It is characterized by two wearable CP antennas with widečňfan-like elevational beam [151]. To the authors' best knowledge, the CP spatial diversity measurement campaign for off-body communication is up to date not available.

Due to the complex antenna-body effects (e.g. near-field coupling, radiation pattern fragmentation and shifts in antenna impedance) [152], it has been crucial to compare the propagation characteristics, as well as the anti-fading effectiveness between the proposed solution and traditional LP diversity schemes to guarantee the reliability and repeatability of the proposed method in the off-body communications [149, 153].

In this letter, the propagation characteristics for an off-body CP spatial diversity scheme and other two typical LP diversity solutions at 5.8 GHz are extensively measured. Then, the signal level models for LP and CP diversity receptions are mathematically modeled with the diversity gains, the cross-polar discrimination (XPD) gain and polarization misalignment loss (PML). The diverse effects of polarization misalignment on LP and CP are evaluated. Further, the LP-CP signal-level difference and diversity gains for both the LP and CP reception are validated.

3.2 Measurement Setup

The typical frequency domain channel sounding system and experimental environment are shown in Fig. 3.1(a) [154]. A Vector Network Analyzer (VNA) is used to generate a 0 dBm, 401-point sweeping signal with the frequency ranging from 5.7 to 5.9 GHz. An omnidirectional monopole antenna fixed at the height of 1 m is used to emulate the transmitting antenna (Tx), and two wearable antennas mounted on the shoulders of a volunteer are used to emulate the receiving antennas (Rx). An equal-gain combiner (EGC) is used to merge the signals from two wearable antennas. The measurement process is repeated for all three types of antennas and six volunteers. During the measurement, the volunteers are allowed to keep different postures, such as squat, standing and rotating which frequently occur in daily life to test the anti-fading effectiveness of measured diversity solutions in real application environment.

In order to implement the proposed novel reception scheme, the receiving antenna should be equipped with two special features: 1) a fan-like elevational beam to provide wide coverage and to guarantee the reception of strong Multi-Path Components (MPCs), 2) a CP property that provides the ability to receive arbitrary polarized signals and to reduce root mean square Delay

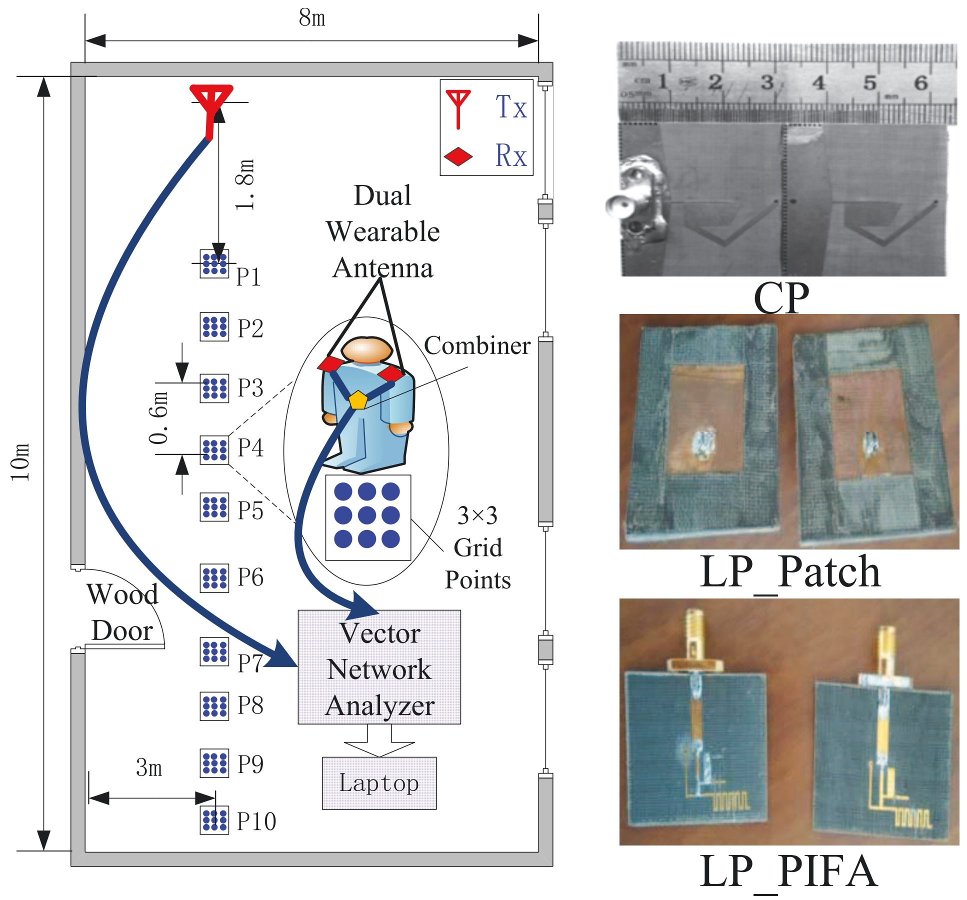

(a) The measurement system and three types of antennas.

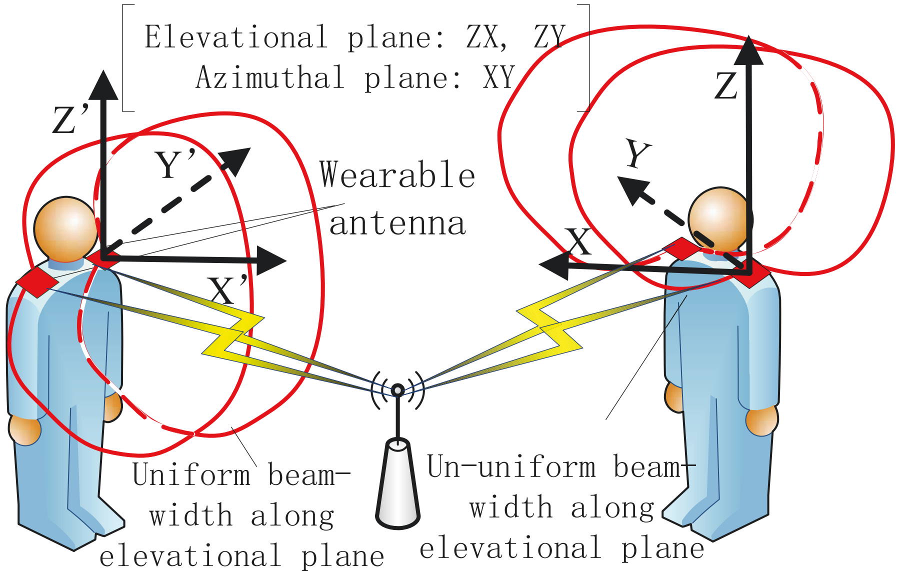

(b) Uniform and un-uniform beam width in elevational plane.

Figure 3.1: Measurement setup and novel uniform beam width in elevational plane

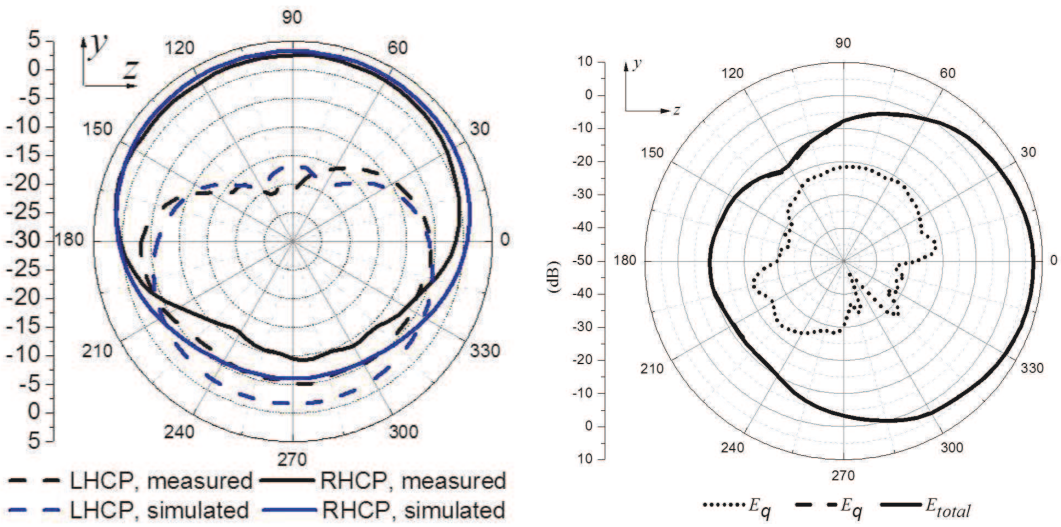

(a) CP pattern

(b) Patch pattern

Figure 3.2: Radiation patterns of wearable antennas.

Spread (DS) [149]. Fig. 3.1(b) shows that the proposed solution with wide elevational beam-width antennas on the left person can always provide strong and stable signal levels during height variations. In contrast, the signals received by the antennas on the right person can face severe fluctuations due to its inherent un-uniform elevational beam patterns. Thus, the planar end-fire CP antennas with wide elevational beam-width are chosen for implementing the proposed CP scheme [151]. Two kinds of typical LP wearable antennas are strictly chosen: a) patch LP antennas (*LP_Patch*, neither feature is equipped) and b) planar inverted-F (PIFA) omnidirectional LP antennas (*LP_PIFA*, only equipped with the first feature shown in Fig. 3.1(a).

3.3 Diversity Characteristics

The RMS DS and number of MPCs are important parameters to characterize the off-body channels, such as the data rate estimation and bandwidth limitations [149]. Fig. 3.3(a) shows the median DS and MPC numbers over different volunteers. The DS for the proposed CP reception, the LP_PIFA case and the LP_Patch over different volunteers are around 6 ns, 8 ns and 10 ns. Meanwhile, the MPC number for three diversity receptions are about 150, 200 and 250 paths. Similarly, the variations of DS σ_{DS} and MPC σ_{MPC} over different volunteers for three schemes share the same trend with the specific values of 0.8 ns, 1.6 ns, 2.5 ns and 20, 38, 59 paths respectively. It is worthy to note that the DS and MPC NUMBER can be largely reduced by using the proposed reception scheme with both features while the LP_Patch without either of two features has the worst DS and MPC parameter values.

Table 3.1: Comparison of Distributions for Three Types of Antennas (Tx-Rx Distance = 3.8 m, $\Delta AIC = AIC - AIC_{CP}$)

Cases	Parameters	Distribution	μ / Exp(μ)	σ	ΔAIC
CP	DS [ns]	Log-norm.	1.27 / 3.56	0.59	0
	MPC number	Log-norm.	4.70 / 109	0.41	0
	Delay [ns]	Log-norm.	2.48 / 11.92	0.16	0
	Sig. level [dB]	Normal	-61.49 / -	2.30	0
LP PIFA	DS [ns]	Log-norm.	1.53 / 4.62	0.59	107.2
	MPC number	Log-norm.	4.90 / 133	0.46	134.2
	Delay [ns]	Log-norm.	2.60 / 13.52	0.21	189.3
	Sig. level [dB]	Normal	-63.42 / -	3.22	142.5
LP Patch	DS [ns]	Log-norm.	1.90 / 6.69	0.46	163.2
	MPC number	Log-norm.	5.10 / 163	0.44	294.4
	Delay [ns]	Log-norm.	2.68 / 14.51	0.26	269.8
	Sig. level [dB]	Normal	-68.07 / -	2.30	13.2

Fig. 3.3(b) shows the median rms DS and MPC NUMBER results among 10 measured locations. The MPC NUMBER parameter is limited to a 15 dB dynamic range of the peak value. Similar to cases over different volunteers, an average reduction of 50 paths and 2 ns for the MPC numbers and DS over measured locations are found when the CP diversity is used. It seems that the DS and MPC NUMBER for CP diversity approximately vary in proportion to the Tx-Rx separation with flatten fluctuations,while the ones for two LP schemes exhibit significantly irregular fluctuations instead.

Table 3.1 shows the best distributions of four small-scale fading parameters at the 4th measured location, using the second-order Akaike Information Criterion (AIC) [155]. It is clear that nearly all statistics of the CP case is less than the LP_PIFA case while the latter one is less than the LP_Patch case. For example, the mean MPC NUMBER for CP diversity presents

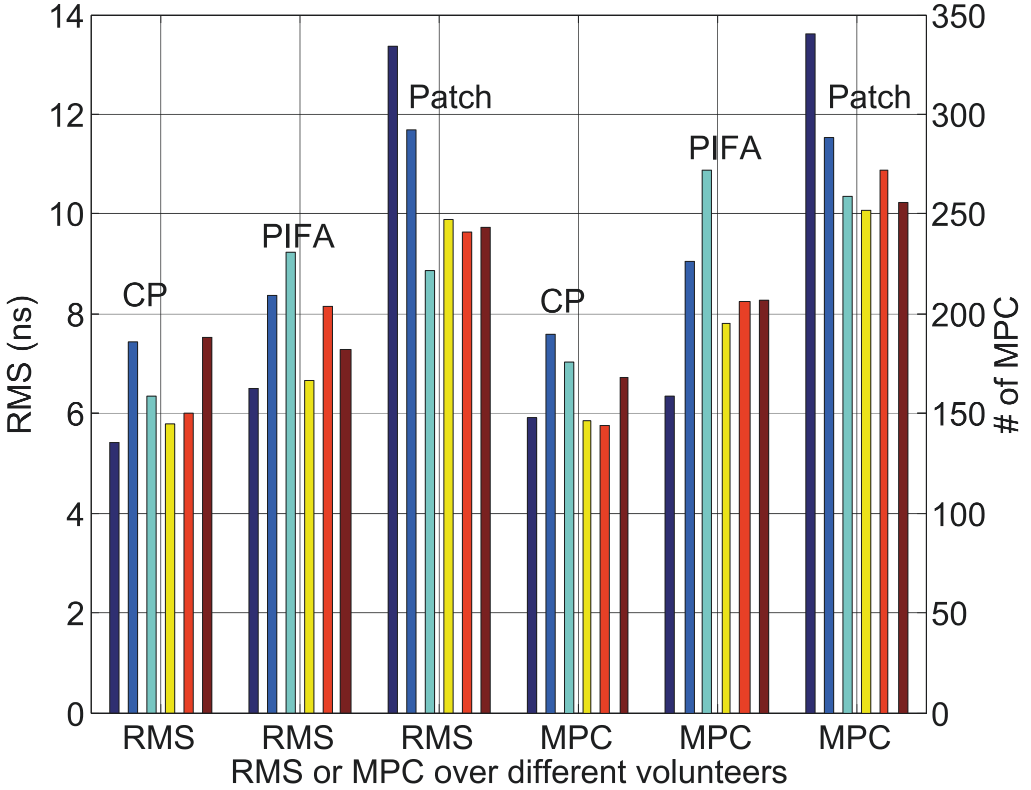

(a) The RMS delay spread and numbers of MPC for three types of antennas over different volunteers.

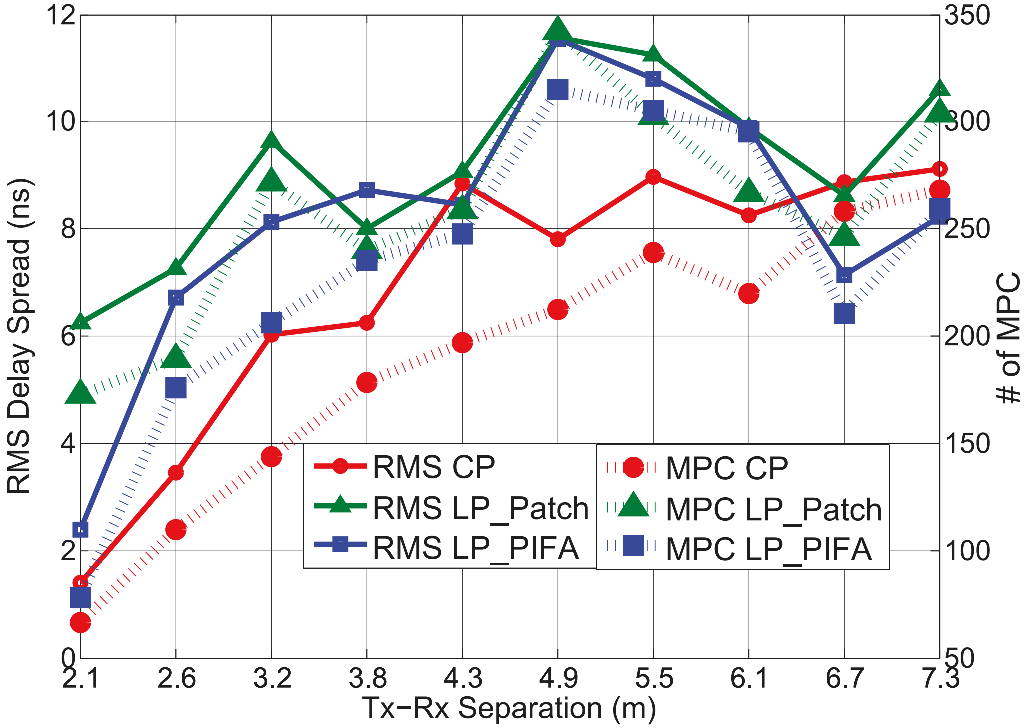

(b) The RMS delay spread and numbers of MPC for three types of antennas among ten measurement locations.

Figure 3.3: Small scale parameters over different volunteers and different measured locations.

a reduction of 22% of the LP_PIFA case while the LP_PIFA presents a reduction of 22% of the LP_Patch case. This again shows the advantages of proposed solution and its two special features.

The analysis above shows that under the same conditions, the small-scale statistics, as well as their variations over different persons and measured locations are greatly reduced when proposed reception is used.

3.4 Modeling and Validation

3.4.1 Signal Modeling

For any point-to-point wireless communication link with one LP transmitting and one LP receiving antenna [156], the discrete-time input-output relation can be given as

$$\mathbf{Y}_{LP} = \mathbf{H}x + \mathbf{N}_d = \begin{bmatrix} h_{VV}x + n_1 \\ h_{HV}x + n_2 \end{bmatrix} \tag{3.1}$$

where x is the transmitting signal vector and $\mathbf{Y}_{LP}$ is a 2×1 received signal matrix with $\mathbf{Y}_{LP}(1)$ and $\mathbf{Y}_{LP}(2)$ representing the signal received in the vertical and horizontal polarized direction respectively. The channel matrix is $\mathbf{H} = [h_{VV} \;\; h_{HV}]^T$ which is affected by depolarization or XPD ($\alpha \triangleq \frac{E|h_{HV}|^2}{E|h_{VV}|^2}$). The h_{VV} and h_{HV} represent the Channel Impulse Responses (CIR) in the vertical and horizontal direction respectively. The noise matrix is $\mathbf{N}_d = [n_1 \;\; n_2]^T$ and $n_1, \; n_2$ are both zero-mean additive white Gaussian noise with standard variation σ.

Here and throughout, vectors are in lower case letters, and matrices are in capital case letters. The notations $(\cdot)^T$, $\|\cdot\|$, $(\cdot)'$, $\tilde{(\cdot)}$ denote transpose, norm of a matrix, signal from another branch and signal with PML.

As the distance between two wearable antennas in this experiment is far more than the working wave length and the received signal of an EGC M-branch reception is $y = \frac{y_1+y_2+\cdots+y_M}{\sqrt{M}}$ [157], the EGC output for dual-branch LP reception (e.g. LP_PIFA) is

$$\begin{aligned} y_{LP-Diversity} &= \tfrac{1}{\sqrt{2}}(\mathbf{Y}_{LP}(1) + \mathbf{Y}'_{LP}(1)) \\ &= xg_l h_{VV} + n \end{aligned} \tag{3.2}$$

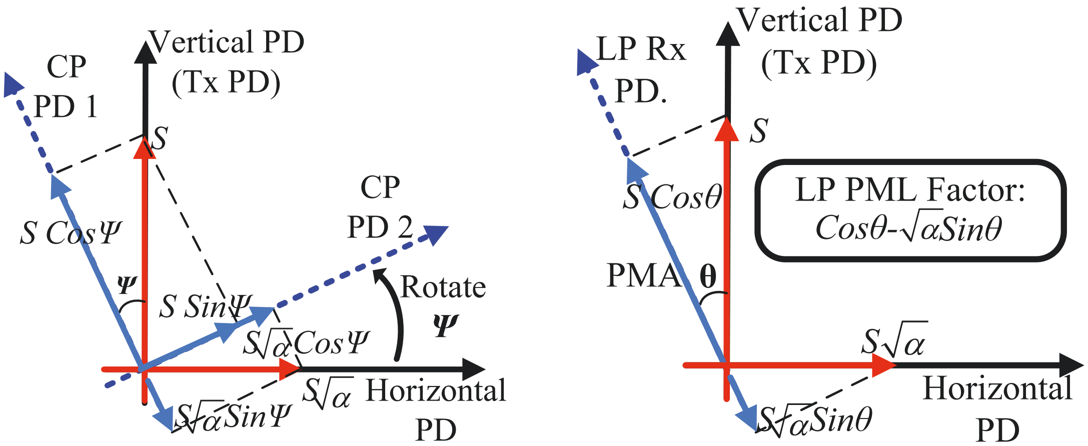

(a) CP received signals (b) LP PML

Figure 3.4: Illusion of (a) CP equivalent PDs and (b) LP PML analysis. PD denotes polarized direction and PMA is Polarized misalignment angel. $S = xh_{VV}$.

where the diversity gain for LP reception represents

$$g_l = \frac{\sqrt{2}}{2}(1 + \frac{h'_{VV}}{h_{VV}}) \quad . \tag{3.3}$$

As the CP receiving directions have an equivalent rotation angle Ψ when comparing to LP reception shown in Fig. 3.4(a), the received signals are equivalent to multiply a rotation matrix $\mathbf{R}_{cp} = \mathbf{R}(\Psi) = \begin{bmatrix} \cos\Psi & -\sin\Psi \\ \sin\Psi & \cos\Psi \end{bmatrix}$. Due to the mismatch between LP Tx and CP Rx, the output of single CP antenna is weakened by $\sqrt{2}$ in amplitude [149, 156] shown as:

$$\mathbf{Y}_{CP} \quad = \tfrac{\sqrt{2}}{2}\mathbf{R}_{cp}(\mathbf{H}x + \mathbf{N}_d) \quad . \tag{3.4}$$

Similarly, the CP-diversity EGC output represents

$$\begin{aligned} y_{CP-Diversity} &= \tfrac{1}{\sqrt{2}}(\|\mathbf{Y}_{CP}\| + \|\mathbf{Y}'_{CP}\|) \\ &= \tfrac{\sqrt{2}}{2}(xg_c h_{VV}\sqrt{1+\alpha} + n) \end{aligned} \tag{3.5}$$

where the diversity gain for dual-branch CP reception is

$$g_c = \frac{1}{\sqrt{2}}(1 + \frac{\| \mathbf{Y}'_{CP} \|}{\| \mathbf{Y}_{CP} \|}) = \frac{\sqrt{2}}{2}(1 + \frac{h'_{VV}}{h_{VV}}\frac{\sqrt{1+\alpha'}}{\sqrt{1+\alpha}}) \quad . \tag{3.6}$$

It is found that the signal level for CP reception is independent of the CP polarization rotating angle. Compared to LP diversity output (2), the CP signal level is improved by the XPD gain

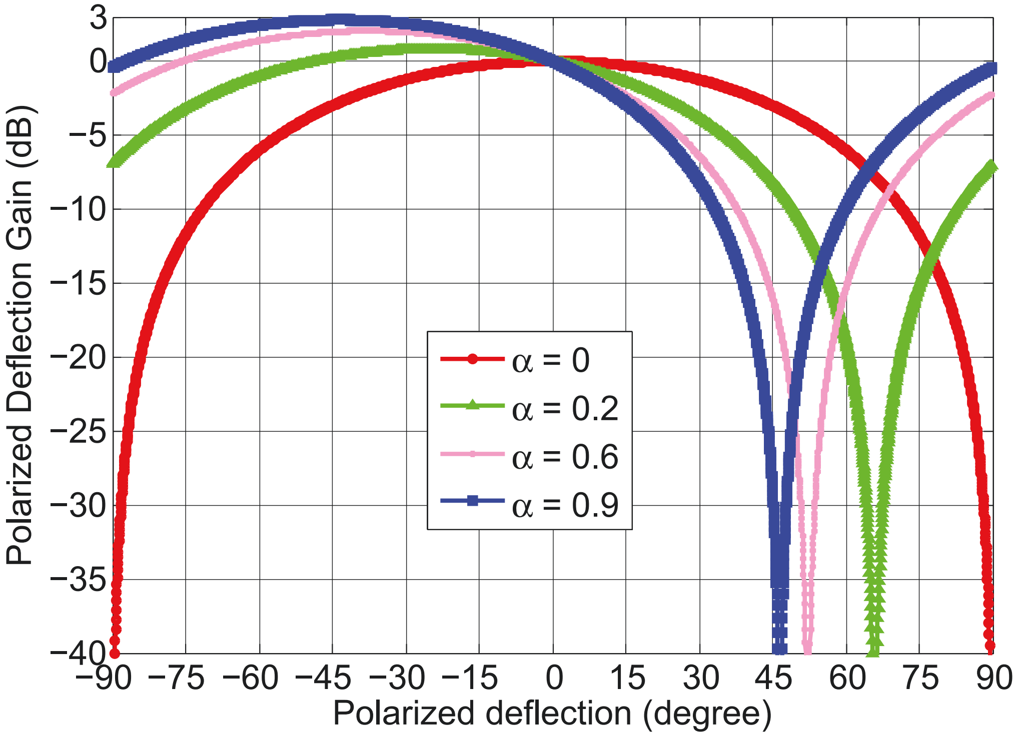

Figure 3.5: The polarization misalignment loss for LP reception with polarized misalignment angle ranging from - 90 to 90 degree.

factor $\sqrt{1+\alpha}$ in (5). That reflects the physical insights of CP reception to pick up the signals in horizontal polarized directions which is neglected by LP reception.

3.4.2 Polarization Misalignment Effect

As the polarization misalignment between the Tx-Rx antennas (e.g. the subject's small deflection, slight wrinkle of textile antennas and Tx-Rx inclination) has significant effect on reception results [148].

Fig. 3.4(b) shows the PML analysis for LP reception. Similar to (1), the signal received by a LP antenna is equivalent to multiply a matrix $\mathbf{R}_{PM} = \mathbf{R}(\theta)$ shown as

$$\tilde{\mathbf{Y}}_{LP} = \mathbf{R}_{PM}(\mathbf{H}x + \mathbf{N}_d) \quad . \tag{3.7}$$

Then, the LP EGC output affected by PML is

$$\begin{aligned} \tilde{y}_{LP-Diversity} &= g_l \tilde{\mathbf{Y}}_{LP}(1) \\ &= x g_l h_{VV}(\cos\theta - \sqrt{\alpha}\sin\theta) + n \end{aligned} \tag{3.8}$$

The comparison of LP-diversity signal levels with and without PML is shown as

$$\frac{\tilde{y}_{LP-Diversity}}{y_{LP-Diversity}} = \cos\theta - \sqrt{\alpha}\sin\theta \quad . \tag{3.9}$$

Fig. 3.5 shows the PML for LP reception among four XPD values with (3.9). Except XPD = 0 (always power loss), the PML for LP reception at other XPDs are characterized by great power loss but slight power gain between -∞ and 3 dB. For example, when XPD = 0.2 and misalignment angle is 15 degrees, the PML is -1.42 dB while the gain is only 0.68 dB.

Similarly, the signal level of single CP receiving antenna with a polarized misalignment angle θ is shown as

$$\tilde{\mathbf{Y}}_{CP} = \tfrac{\sqrt{2}}{2}\mathbf{R}_{PD}\mathbf{R}_{CP}(\mathbf{H}x + \mathbf{N}_d) \quad . \tag{3.10}$$

The CP EGC output with polarization misalignment is

$$\begin{aligned} \tilde{y}_{CP-Diversity} &= \tfrac{\sqrt{2}}{2}(\|\tilde{\mathbf{Y}}_{CP}\| + \|\tilde{\mathbf{Y}}'_{CP}\|) \\ &= y_{CP-Diversity} \quad . \end{aligned} \tag{3.11}$$

Equation (11) shows that the polarization misalignment makes no difference to the signal levels of CP reception. The big PML fluctuation for LP reception can provide an explanation for its larger variances of small-scale parameters than CP diversity.

To compare the combined signals between CP and LP receptions, the LP-CP signal-level difference is (noise is neglected)

$$\frac{\tilde{y}_{LP-Diversity}}{\tilde{y}_{CP-Diversity}} = \frac{g_l}{g_c}\frac{\sqrt{2}(\cos\theta - \sqrt{\alpha}\sin\theta)}{\sqrt{1+\alpha}} \quad . \tag{3.12}$$

3.4.3 Signal-level simulation for CP and LP diversity receptions

2000 Monte Carlo simulations for the signal levels of LP and CP receptions are performed according to the CP, LP and LP-CP signal level models of (5) (8) and (12). The measurement-based CIR of any single off-body link is modeled as a Rayleigh random variable with the standard variation $\sigma = 4.21 \times 10^{-4}$. The XPD is modeled as a normal random variable with the mean value $\mu = 6.5\ dB$ and standard variation $\sigma = 1.5$ [149]. The polarization misalignment angles are randomly selected from -18 to 18 degrees [158].

The cumulative distributions functions (CDF) of diversity gains for the LP and CP receptions are shown in Fig. 3.6 with their diversity gains of 90% reliability are both 2.3 dB, consistent with [159]. No significant difference is found between LP and CP diversity gains, except the slight large proportion of high diversity gains for CP reception due to the effect of XPD gain factor in (6). On the other hand, the normal CDFs of both the measured and simulated LP-CP signal-levels are also shown in Fig. 3.6. According to the 0.8 dB mean values of both CDFs, the signal levels of LP diversity seems to be slight stronger than CP ones. However, if the 3 dB polarization mismatch loss (LP Tx and CP Rxs) for CP diversity reception is removed [156], the CP signal levels are expected to be 2.1 dB higher than the LP ones. It can be explained that the normal-distributed XPD gain factor ($\mu = 0.92, \sigma = 0.28$) strengthens the received signal of CP diversity to 0.9 dB while the PML weakens the LP signal levels by around 1.2 dB. The PML for LP reception is fitted by the truncated student-t distribution with an upper bound of 1.7 dB ($\mu = 0.05, \sigma = 1.51, \nu = 1.26$) which is characterized by a long negative-power tail [160]. The XPD gain factor and LP PML can provide an explanation why the small-scale variation (e.g. signal levels, DS and MPC NUMBER) is reduced when the proposed solution is used.

It is noted that the measured 2-branch EGC signal follows normal logarithmic distribution. And Rayleigh distributed is found by attaching a single antenna to each part of the human bodyčňmore detailed parameter values are thus obtained. Although, the direct LOS Tx-Rx signal tends to be the distribution of Rice, the actual fitted result in WBAN is Rayleigh distribution. One explanation is that due to the influence of human body, the Fresnel between

TX-RX is shielded too much, resulting its LOS path is not dominating. This is where WBAN differs significantly from traditional short-range communications because antennas have never been so close to a human during the whole communication period.

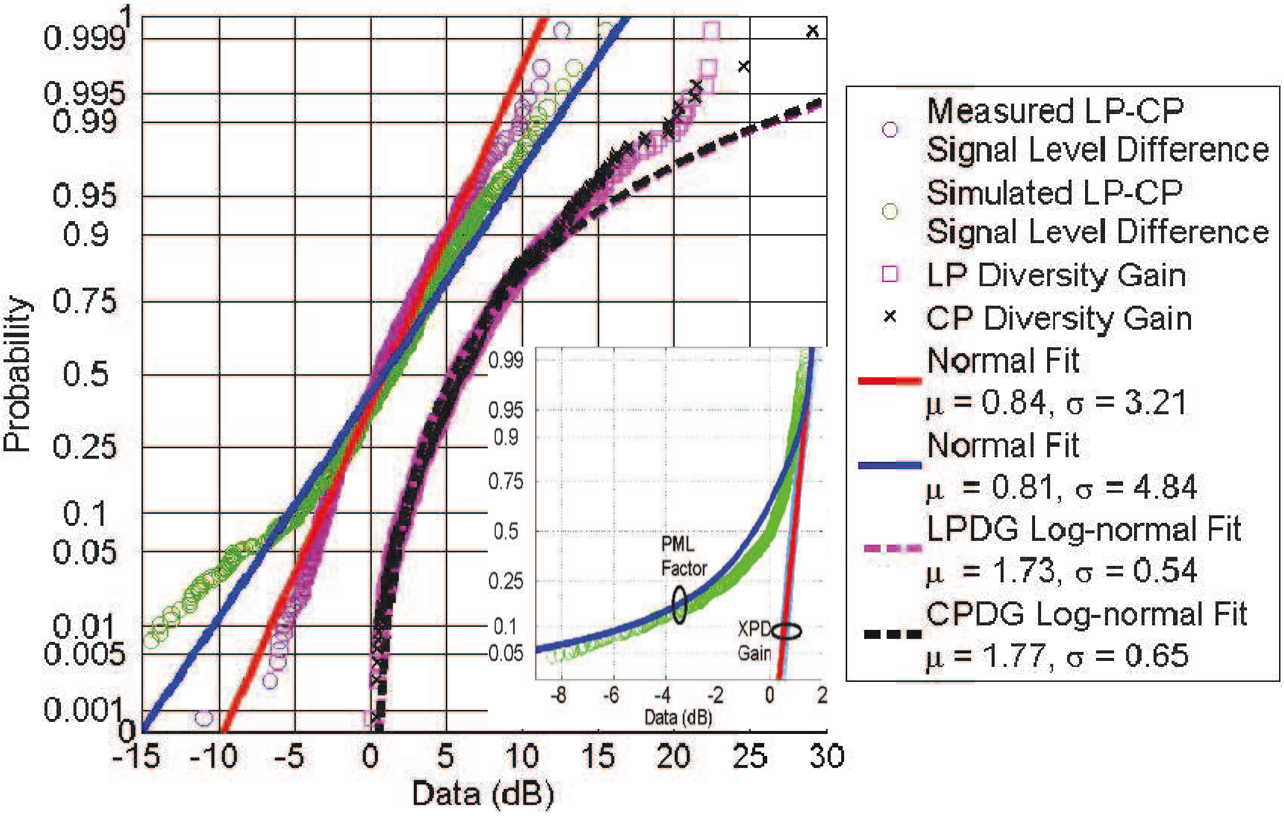

Figure 3.6: The simulation of LP-CP signal-level difference and diversity gains for LP and CP receptions.

3.5 Conclusion

In this letter, a novel low-complexity CP spatial diversity reception solution is proposed to reduce the body-height dependent fading. It is found that comparing to two typical LP diversity schemes, the MPC numbers, RMS delay spread and their variations over measured locations and different volunteers for the proposed solution can be greatly reduced. Further, the EGC LP-CP signal level difference model is derived as the functions of diversity gains, CP XPD gain factor and LP PML factor. The CP XPD gain and LP PML factors which have clear physical insights are best fitted by normal and truncated student-t distributions, respectively. On one hand, when comparing to traditional LP schemes, the received signal for proposed solution is averagely improved by 2.1 dB due to XPD gain and PM loss. On the other hand, the DS and RMS variations for proposed solution are greatly mitigated due to its ability to receive strong multipath components of arbitrary polarization, which are easy to be ignored by LP reception. The presented results can be used to design the physical layer for body-centric communication systems.

Chapter 4

MIMO Body-related Channel Measurement and Analysis

4.1 Introduction

Massive MIMO is becoming an essential technology in mobile and WiFi networks [161, 162]. In recent years, extensive measurement and evaluation activities have been carried out on massive MIMO systems, focusing on three directions. The first is on the properties of outdoor large arrays such as array aperture, decoupling effect, and anti-interference [161, 163]. The second is on distributed multiuser (MU) massive MIMO [164, 165]. The third is on practical problems in using massive MIMO systems, e.g., the spherical wave induced by large-scale arrays, the polarization characteristics and the coupling characteristics within the Rayleigh distance [161, 166, 167].

However, there are limited results reported for indoor massive MIMO channels, and the impact of human body on such channels when the person is using a hand-held device or next to a standalone wireless device. Several important problems for such channels are yet to be investigated. For example, the wide-sense non-stationary or stationary characteristics (or power imbalance) along transmitter (Tx), receiver (Rx) arrays and Tx-Rx domains, pros and cons of multipath on massive MIMO system performance, and the degree of mitigation of human blockage effect by massive MIMO. It is also important to understand the capacity gap between real channels and theoretical ones, particularly for indoor channels where line-of-sight (LOS) and non-LOS (NLOS) propagation may have significant impact on channel correlation across antennas.

In this chapter, we investigate the propagation property and the impact of human body on the propagation for a 32x8 Uniform Planar Array (UPA) MIMO system in an indoor environment with measurements obtained in multiple indoor LOS/NLOS, Body/NoBody scenarios. We first introduce the measurement setup in Section II. We then propose a method in Section III for evaluating the power imbalance and channel popularity in LOS/NLOS, Body/NoBody cases. In Section IV, we analyze the capacity, correlation and angular power spectrum for channels in multiple scenarios.

4.2 Measurement Setup

Our measurement campaign was conducted in a typical office environment as shown in Fig. 4.1 (a) and (b). A large UPA which contains 128 antenna elements is used to emulate the Base Station (BS) and an 8-element UPA is used to emulate the Mobile Station (MS), as shown in Fig. 4.1 (c) and (d). During the measurement, only 32 Radio Frequency (RF) chains are active, as shown in Fig. 4.1 (d). The Synchronous Massive MIMO Measurement sounding system (S3M) [162, 168] is used to generate 1200-subcarrier signals with 0 dBm transmitting power in each transmitting port. The central frequency is 3.5 GHz with 20 MHz bandwidth and the sampling rate is 30.72 MHz.

The centre of transmitting and receiving arrays are kept at the same height during the measurement. Nine grids across the office are chosen to deploy the 8-element handset array with the transmitter-receiver (Tx-Rx) distances ranging from 1 to 5 meters. In order to assess the impact of human body on MIMO channels in an indoor environment, at each grid we did measurements for four scenarios: line-of-sight (LOS) connection with a handset fixed on a tripod, LOS with someone holding the handset in a calling gesture, non-LOS (NLOS) with the handset placed on a tripod, and NLOS with the handset held by a person. We denote the

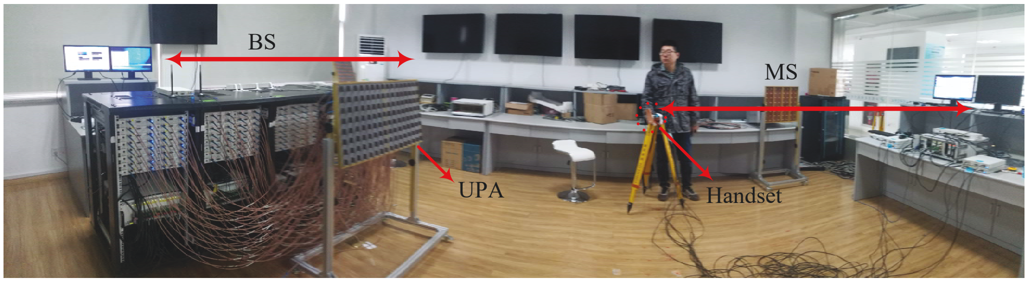

(a) Real office environment and measurement system.

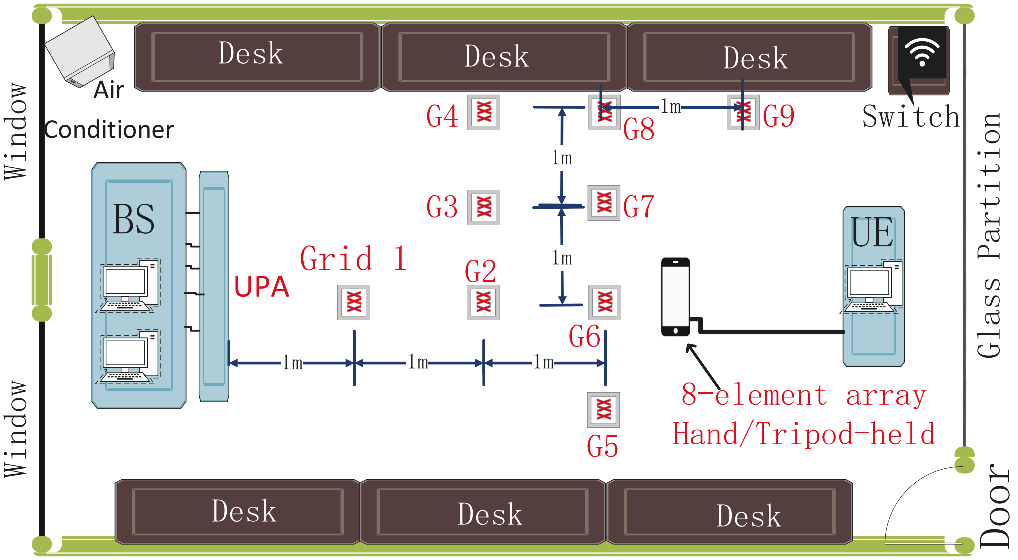

(b) Real office environment and measurement system.

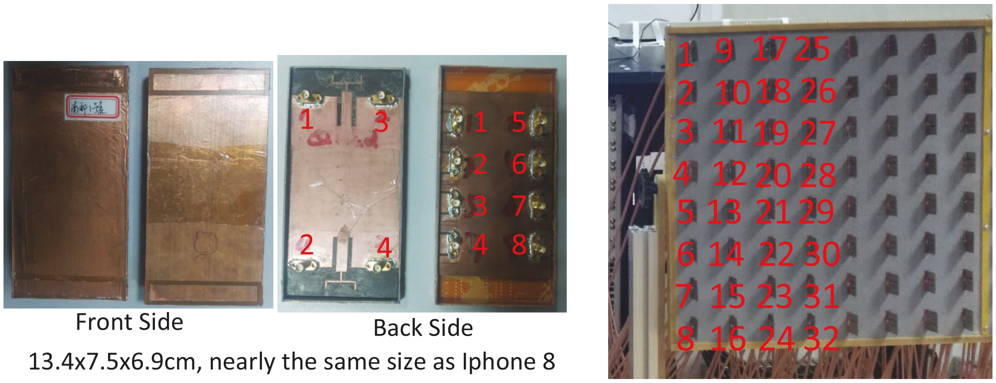

(c) Handset Antenna array

(d) BS antenna array

Figure 4.1: The illusion of (a) Real office environment and measurement system (b) MS Antenna array (c) BS antenna array and Indices.

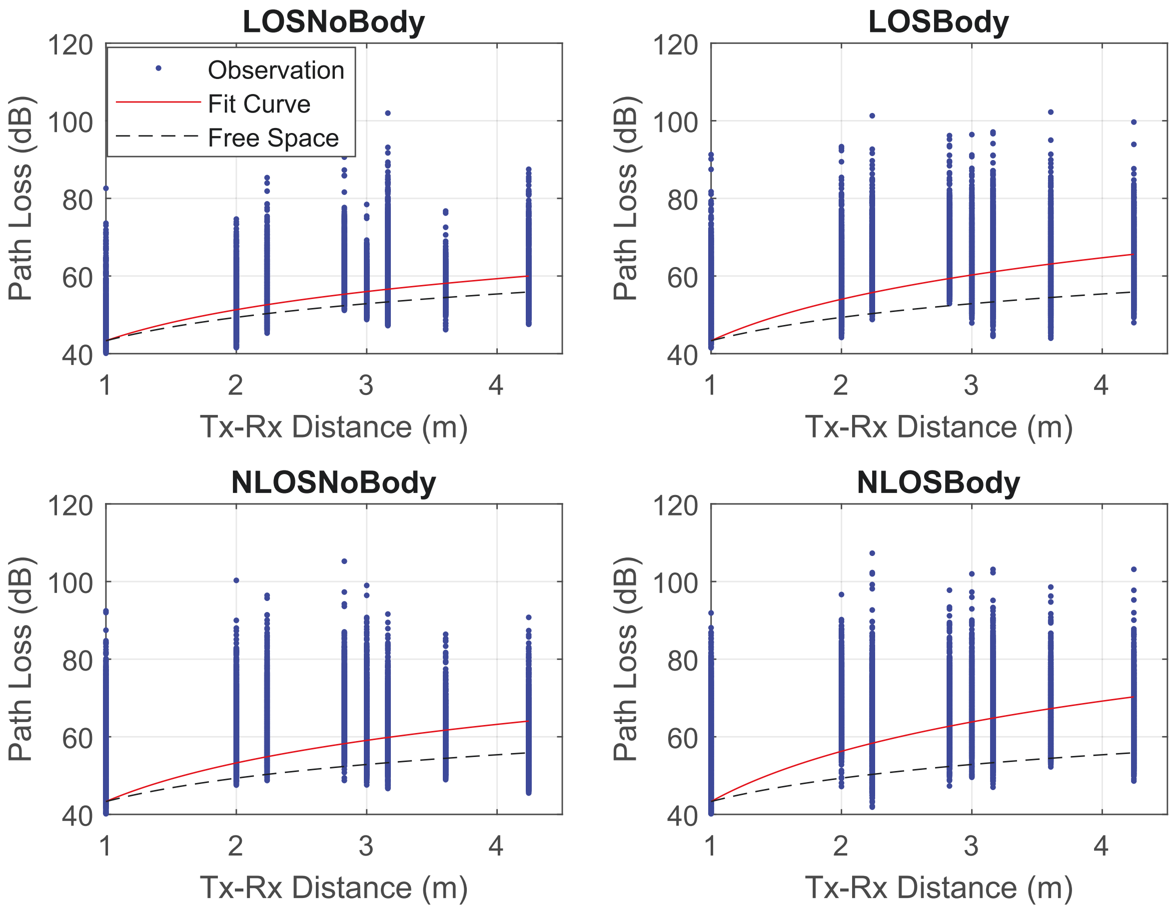

Figure 4.2: Path loss curves for 4 typical scenarios with path loss values averaged over Tx and Rx array.

four scenarios as LOS_NoBody, LOS_Body, NLOS_NoBody and NLOS_Body, respectively. The S3M system synchronously records 300 snapshots for each Tx-Rx link at each grid. Each snapshot contains 12 complex data from subcarriers evenly distributed over 20 MHz bandwidth. Thus, we obtain a 5-dimensional datasets $\mathbf{H}_{t,f,d,m,n}^{Case}$ for each scenario, with the data amount of 8294400 complex values (300x12x9x32x8). In $\mathbf{H}_{t,f,d,m,n}^{Case}$, the parameters t, f, d, m, n represent the indexes of snapshots, subcarriers, grid points, receive and transmit antennas, respectively. More details about the measurement campaigns and S3M system can be referenced to [169, 170].

4.3 Channel Imbalance Characteristics

4.3.1 Path Loss Models

In order to evaluate the effect of adjacent human body on path loss and signal coverage, we adopt the widely used log-distance path loss formula to model all measured signals at different grids as

$$\overline{PL(d)} = PL_0 + 10 \times k \times log_{10}(d) + \overline{\delta_X} \tag{4.1}$$

where PL_0 is the free-space path loss at 1 meter (43.3 dB in our work), k is the Path Loss Exponents (PLE) and $\overline{\delta_X}$ is the mean-zero Gaussian shadowing variable averaging across Tx and Rx UPA domains.

Note that (4.1) can only predict the average power across Tx-Rx arrays. The specific power prediction for each Tx-Rx antenna pairwise $PL(d, m, n)$ is dependent on the power imbalance in Tx and Rx array and other domains. We introduce the concept of *array shadow factor* $\delta_X(m, n, d)$ to characterize this effect. Due to its wide non-stationary property [163], it is tricky to evaluate this parameter.

Table 4.1 shows the parameters for all scenarios obtained using curve fitting technologies. It can be observed that the path loss is affected by both the LOS/NLOS condition and human proximity. Path loss model for the LOS_NoBody case has the minimum PLE and shadow values while NLOS_Body has the maximum values. Human proximity in LOS is equivalent to NLOS state except that the RMSE in NLOS case is obviously larger. Compared with the typical value of 3 for standard shadow deviation and 5 for RMSE of the conventional single-link channels, the key parameters for the measured massive MIMO channels here are slightly larger. The main reason is that massive scatters for large aperture system is about 1-8.5 m in this work and within the Fresnel zone (Rayleigh distance) according to

$$0.62 * \sqrt{D^3/\lambda} < d_{\text{Fresnel}} \leq 2 * D^2/\lambda \tag{4.2}$$

where D and λ are the antenna aperture and wavelength of central working frequency. This means we can not view the tested massive MIMO channels as wide sense stationary over multi dimensions.

Table 4.1: Path Loss Parameters for 4 typical scenes($PL_0 = 43.3$ dB)

Cases	PLE	shadow δ_X	RMSE
LOS NoBody	2.7	4.6	5.3
LOS Body	3.6	5.8	7.5
NLOS NoBody	3.3	5.7	9.2
NLOS Body	4.3	6.3	9.5

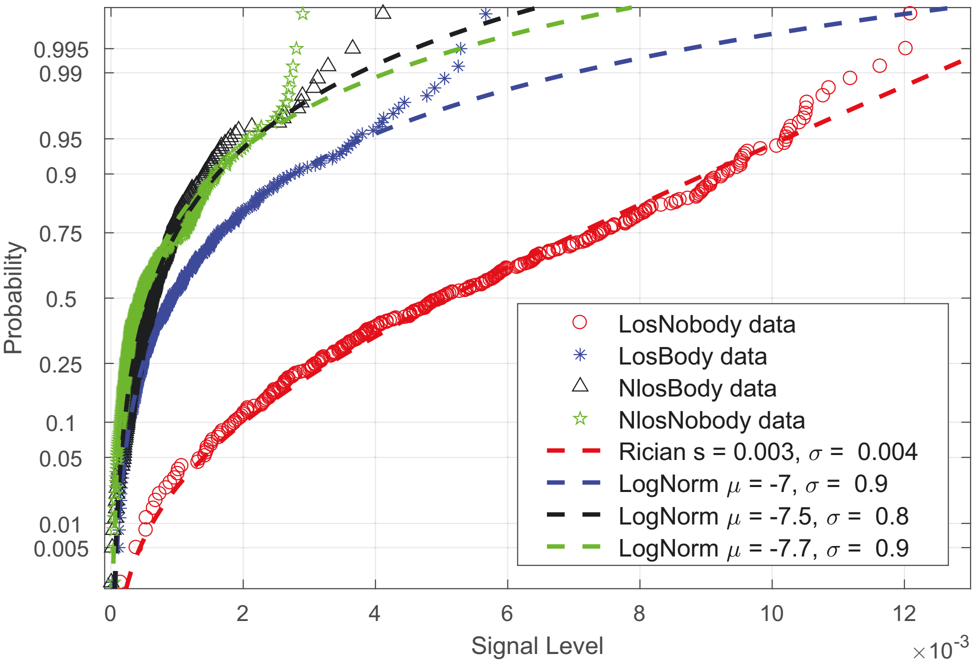

Figure 4.3: Cumulative probability distributions of signal levels under four scenarios using the same random chosen Tx-Rx antenna pairwise at the same grid 2.

4.3.2 Signal Level Distributions

Fig. 4.3 depicts the cumulative probability distributions of signal levels under four scenarios using the same randomly chosen Tx-Rx antenna pairwise at the grid 6 (G6). Only channels in the Los_Nobody case best follows the Rice distribution while the others follow Log-normal distributions. It seems that under the LOS cases, "UE" held by human evidently reduces the mean signal level to 1/5 of the Nobody case. This causes that distributions having larger tails such as Log-normal and Weibull fit the signal levels of massive MIMO channels under real environments better (LOS_NoBody is just too idealistic in practice).

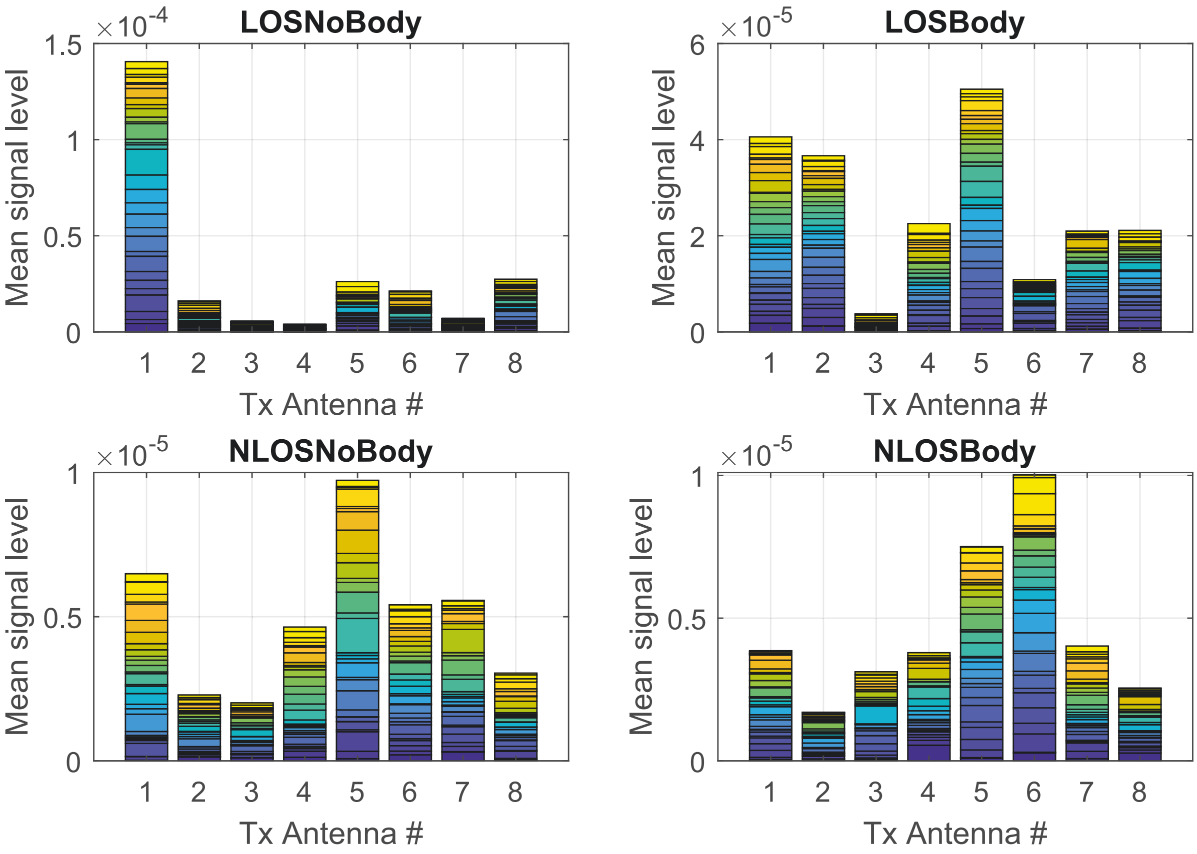

Figure 4.4: Stacked received signal strength across Tx antenna array.

It is noted under all 4 cases that the measured data diverge significantly from the analytical distribution curves at higher signal level. One explanation is that the environment (walls, floor, and ceiling) compensates for weak reflections and diffraction, while the strong signal areas are mainly from direct and body diffraction.This is also the case where NLOS is more deviated than LOS, where the compensating signal is more significant.

4.3.3 Signal Level Variation among Tx/Rx Antenna Array

To explore the impact of adjacent human on none-wide sense stationary features across Tx arrays, we average the signal levels across temporal, frequency and spatial dimensions and stack each received signal according to the transmitting antenna number shown in Fig. 4.4. Antenna 1 in LOS_NoBody contributes over 70% effective transmitting power. Human proximity in the

Table 4.2: Power imbalance values of four scenarios on five different dimensions (Units are all dB, except for SVS.)

Dimensions	LosNB	LosBody	NLosNB	NLosBody	Mean
Rx Antenna	5.6	6.5	4.0	4.6	5.0
Tx Antenna	4.1	4.9	3.5	3.6	4.0
SVS(Tx-Rx)	13.5	14.0	12.0	12.9	13.1
Time	6.1	8.1	5.5	6.4	6.5
Frequency	7.4	4.1	5.3	6.1	5.7

LOS case greatly reduces such imbalance while in NLOS there is no such function.

4.3.4 Power Imbalance among Different Domains

To quantitatively analyze such power imbalance over different domains, we calculate the standard variation along specific domain to obtain its power imbalance. Take the power imbalance in the temporal domain as an example,

$$\begin{split}\mathrm{PI}_{Time} =& \boldsymbol{std}_{Time}(\frac{1}{FDMN}\sum_f\sum_d\sum_m\sum_n \\ & 20 * log_{10}(||H(t,f,d,m,n)||)),\end{split} \tag{4.3}$$

where $\boldsymbol{std}_{Time}$ means to obtain the standard variation along the time domain, and F, D, M, N are the total numbers of subcarriers, measured grid points, receive and transmit antennas, respecitively. Define the *Singular Value Spread* (SVS) of channel transfer matrix $\mathbf{H}_{t,f,d}(m,n)$ as the condition number of this matrix, i.e. the ratio between the maximum and minimum singular value of the matrix $\lambda_{\max}/\lambda_{\min}$. Since the correlation between Tx and Rx domains has a great impact on channel stability and channel performance, we use SVS as the power imbalance indicator for Tx-Rx (Transceiver) domain.

Table 4.2 depicts the power variations across 5 dimensions. Interestingly, imbalances in the NLOS cases are nearly all less than those in LOS cases. This means that unlike conventional channels, the massive MIMO channels in LOS in indoor environment are more stable and popular. The imbalance increases in the order of NLOS_NoBody, NLOS_Body, LOS_NoBody and NLOS_Body, which corresponds to the order of descending performance as will be shown

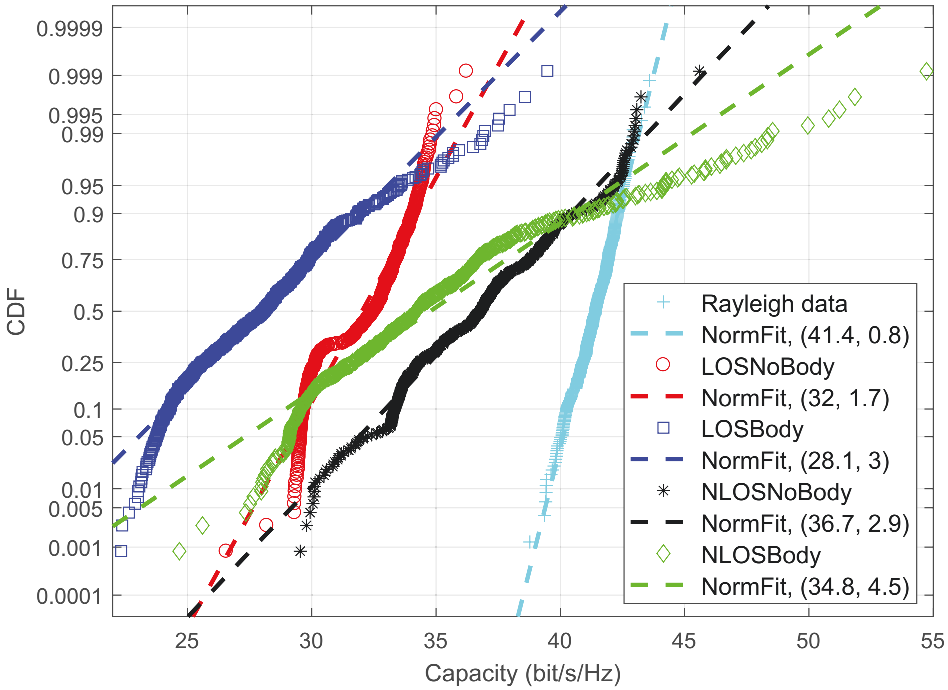

Figure 4.5: Distributions of capacity at 6 th measurement grid.

later.

4.4 Capacity and Impact of factors

4.4.1 Capacity VS Number of Antennas

There exists large capacity gaps between i.i.d Rayleigh and channels in four measurement cases. Fig. 4.8 shows that channels in all cases best follow the Normal distributions while their ergodic capacity varies. When the number is 8, in relation to the capacity for Rayleigh, the capacity for NLOS_NoBody (36.7 bps/Hz) is 90%, and in the worst case, capacity for LOS_Body (28.1 bps/Hz) is only 69%. Human proximity causes capacity loss of about 12% in LOS and 5% in NLOS cases. Comparatively, the SVS shown in Fig. 4.6 shows the opposite trends.

Fig. 4.7 and Fig. 4.8 depict the ergodic capacity for 4 cases when randomly choosing Rx and Tx numbers separately. Ergodic capacity approximately linearly increases with the number of Rx/Tx antenna increasing. It is found that the ratio between the capacity for the

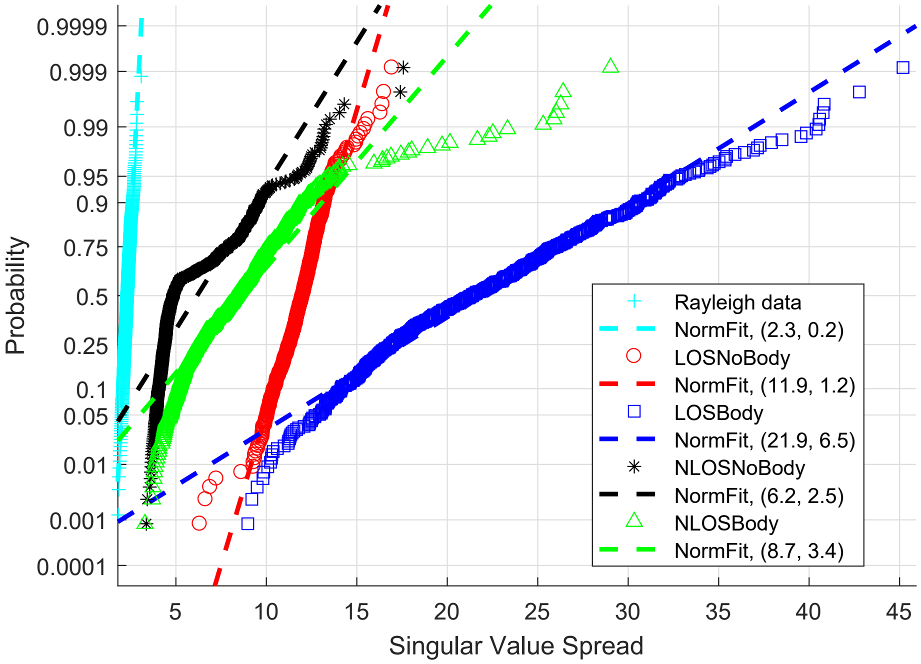

Figure 4.6: Distributions of Singular Value Spread (SVS) for all scenarios at the 6th grid.

“worst” LOS_Body cases and Rayleigh almost remains as 69% with the number of BS antennas increasing, while it decreases rapidly with the number of UE antennas increasing. This means that the human adjacent effect is negligible for mobile devices with multiple antennas.

It is noted that there is an cross of curves (6,29) in Fig. 4.8 between the two cases of NLOS. When the number of antennas is less than 6, more obstruction tends to improve the actual capacity; however, when the number of antennas is more than 6, body obstruction contributes negatively to capacity increasing. One possible explanation is that body occlusion is nonuniform (anisotropic) compared with environmental obstruction, leading to rank deficit of MIMO channel matrix. After the minimum number of antennas at the Tx and Rx reaches a critical point, this rank deficit will dominate, making the capacity gap between the Body and NonBody obstruction cases bigger and bigger. Such rank deficit is one of the main reasons why the capacity slope of the body obstruction case is significantly lower than that of the non-obstruction scene, under both LOS and NLOS scenarios.

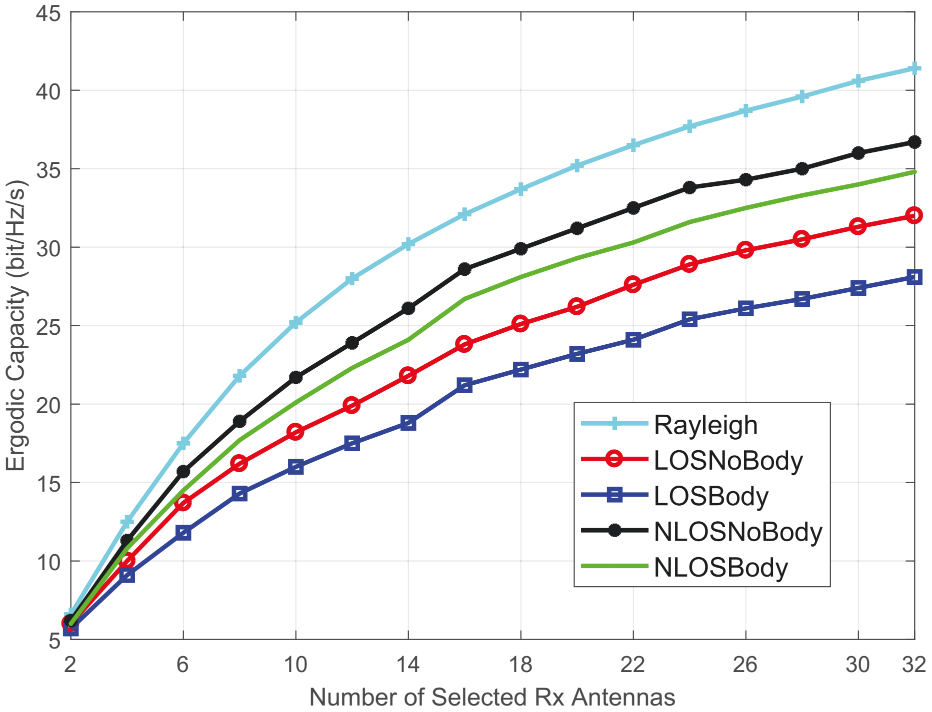

Figure 4.7: Capacity variation with numbers of Rx antennas for all scenarios, $N_{Tx} = 8$, $SNR =$ 10 dB.

4.4.2 Channel Popularity Indices

The sub-linearly increasing rate of capacity for measured channels is important for designing and evaluating massive MIMO systems. We propose an empirical capacity prediction method and a parameter of *Channel Popularity Indices* (CPI) for MIMO system design based on least square curve fitting. The empirical capacities, which are obtained via fitting the curves of Shannon capacity, are given by

$$\begin{cases} C_{Rx}(case, m) = a(case) \times m^{\frac{1}{2}} \\ C_{Tx}(case, n) = 9 \times n^{b} \\ C_{Tx,Rx}(case, m, n) = \sqrt{C_{Rx}(case, m) \times C_{Tx}(case, n)} \\ \qquad\qquad\qquad\qquad\quad = \sqrt{9a \times m^{\frac{1}{2}} n^{b}} \end{cases} \tag{4.4}$$

where $C_{Rx}(case, m)$, $C_{Tx}(case, n)$ and $C_{Tx,R}(case, m, n)$ represent the capacity as a function of the antenna numbers of the Rx, Tx and Rx-Tx pairwise for a given channel scenario/case,

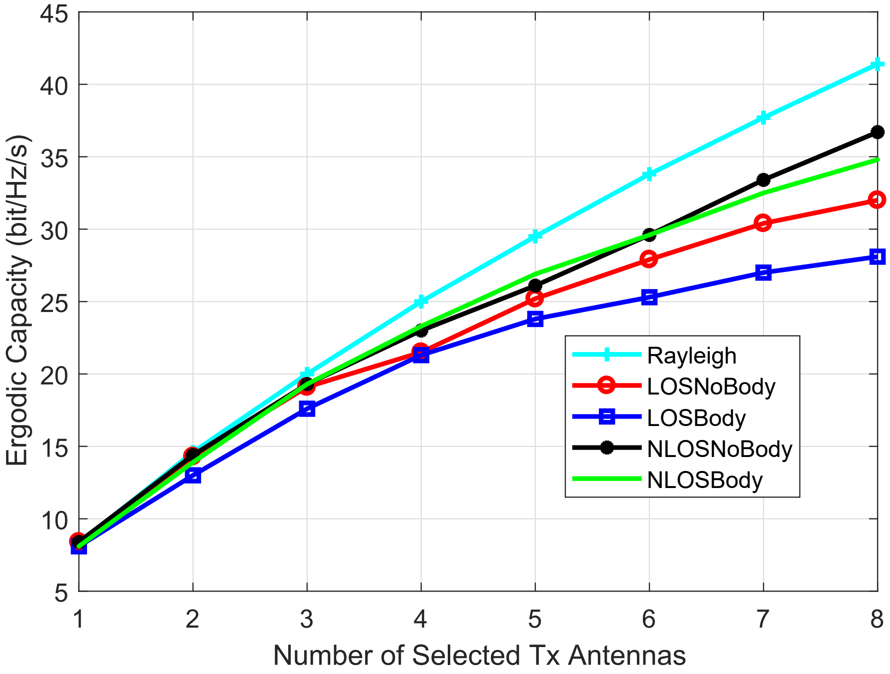

Figure 4.8: Capacity variation with number of Tx antennas for all scenarios, $M_{Tx} = 32$, $SNR = 10$ dB.

respectively. The coefficients of the power functions can be changed according to the scenario. The CPI is expressed as,

$$CPI = \sqrt{\frac{a(case)}{a(Rayl)} \times \frac{b(case)}{b(Rayl)}} \tag{4.5}$$

where $a(case)$ and $b(case)$ are the feature parameters for specific measurement case, $a(Rayl)$ and $b(Rayl)$ are parameters of i.i.d Rayleigh MIMO channels. Table 4.3 shows the fitted parameters for the empirical capacity prediction and CPI. An example for the measurement at grid 6 is also provided. Both the CPI and empirical capacity formula are very simple but works well. It is useful for estimating the performance of practical large-scale MIMO communications.

4.4.3 Correlation Characteristics

The correlation coefficient is averaged over 100 of the 1000 received signals in each receiving or transmitting channel to mitigate the effects of specific values and time periods. Each array is separated by half a wavelength. During all signals received in each scene, the array inclination

Table 4.3: Parameters for empirical capacity formula and CPI

Cases	a	b	CPI	$\frac{C(case,32,8)}{C(Rayl,32,8)}$
i.i.d Rayleigh	7.6	0.74	1	1
LOS NoBody	5.8	0.63	0.80	77%
LOS Body	5.1	0.57	0.72	72%
NLOS NoBody	6.8	0.67	0.90	90%
NLOS Body	6.3	0.66	0.86	86%

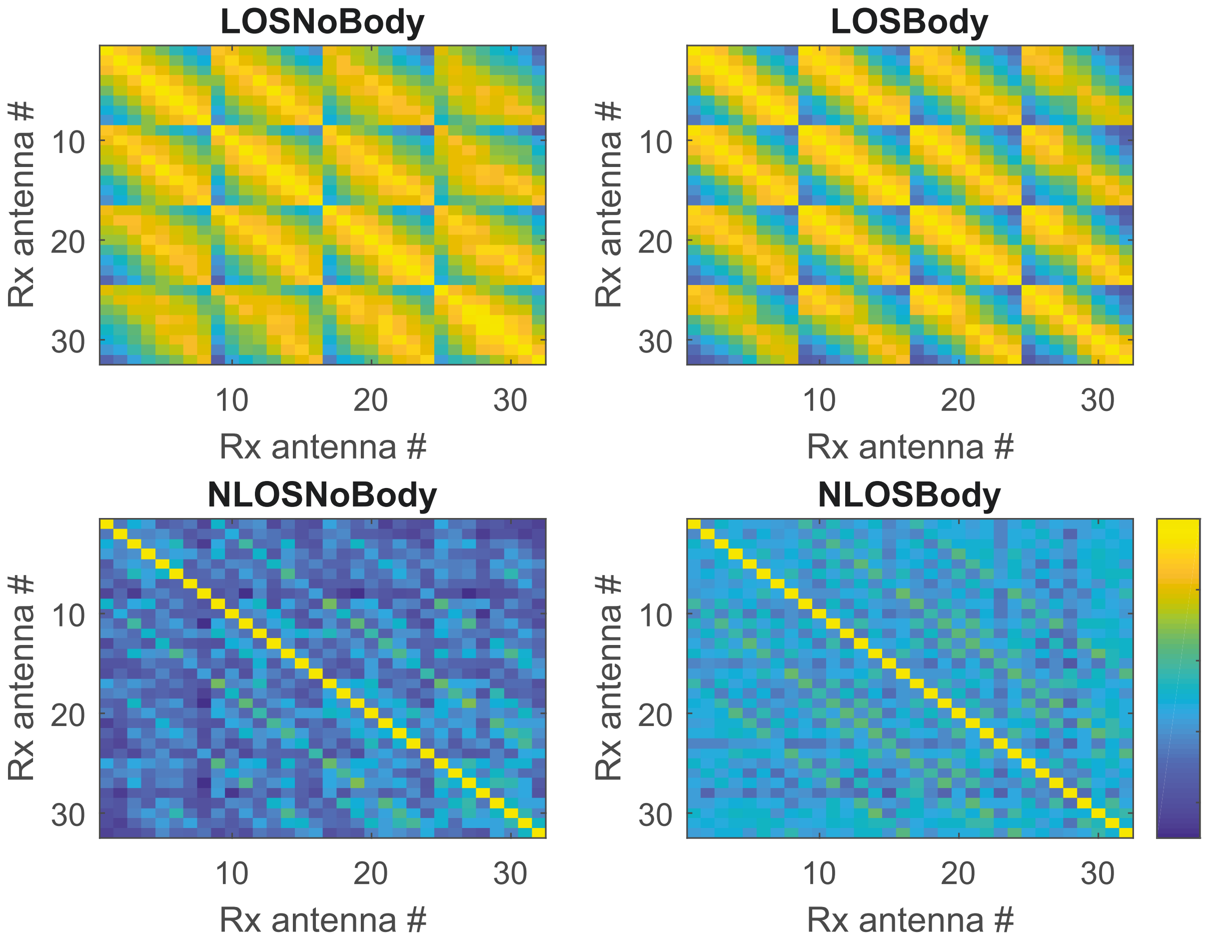

Figure 4.9: Typical inter-channel correlation map across receiving array on measurement grid 2 for all scenarios. Mean correlation 0.73, 0.69, 0.37, 0.46.

is maintained at 30 degrees with the same orientation.Array spacing, dip, and type of antenna polarization all affect correlation, but at that time it is an another separate and interesting topic.

The inter-channel correlation of indoor massive MIMO channels along 5 domains is found to

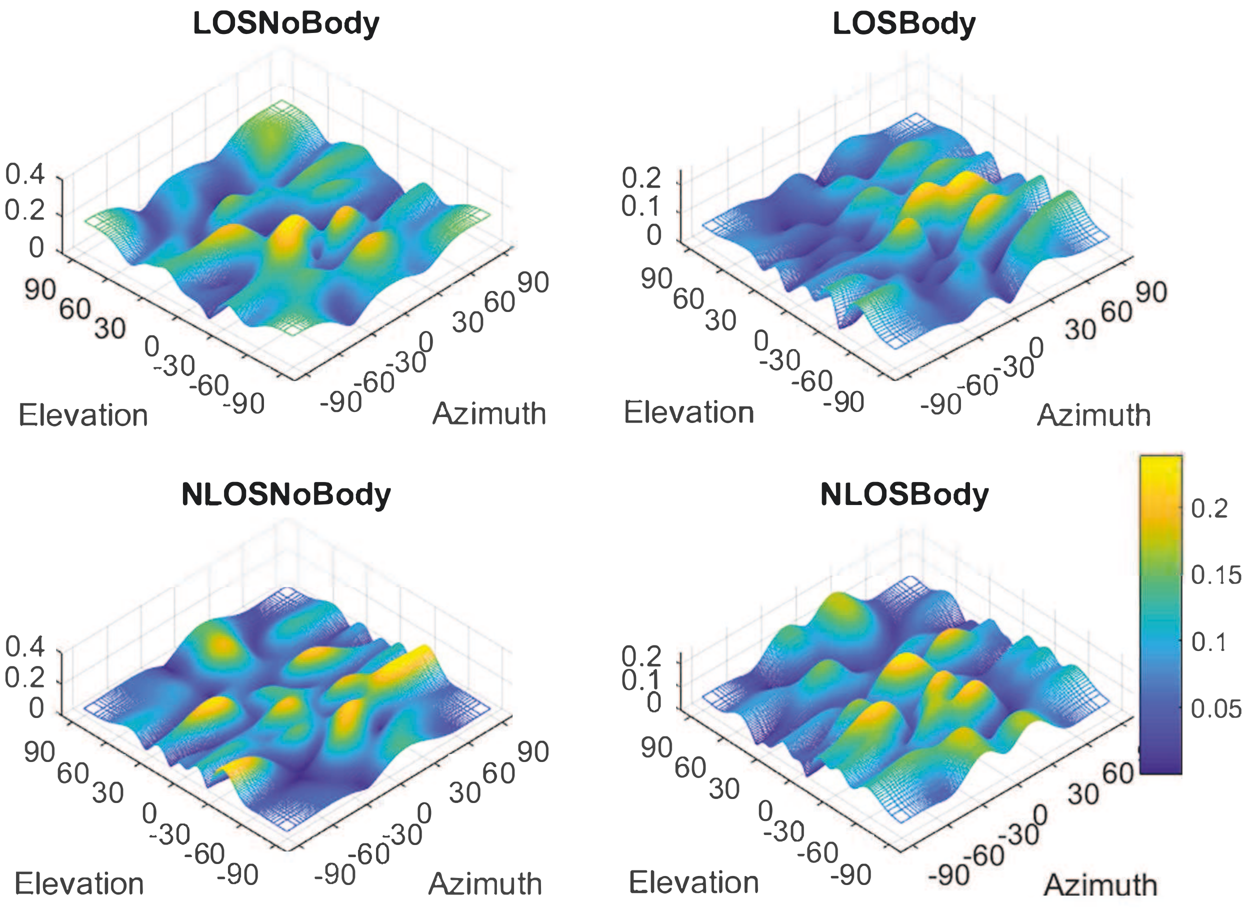

Figure 4.10: Arriving angular power spectrum across received antenna array for randomly chosen snapshot, subcarrier and measurement location.

be very high. For example, the mean correlation over the Rx array domain is between 0.35 and 0.8, and it is 0.77, 0.72, 0.55 and 0.74 for the other four domains. The individual correlation varies at different measurement grids.

Fig. 4.9 shows a typical Rx inter-channel correlation map at grid 2. The Rx correlations for NLOS cases are much smaller than those for LOS, which is consistent with the widely known acknowledged fact. The correlations within 8 antennas in each column are larger than those across columns. The correlations within each row in the Rx array are also significantly larger than the inter-row correlations. This makes the correlation map present multiple symmetric and parallel diagonal peaks ribbons forming similar “salmon streaks".

4.4.4 Angular Power Spectrum

Angular power analysis is the basis for 3D MIMO channel modeling. By using the DFT based angular analysis method in both elevation and azimuth directions, the angular profiles are obtained for the measurements over snapshots, grid points and subcarriers for four cases, as shown in Fig. 4.10. We find that the number of significant clusters in two NLOS scenarios are generally twice as many as those in LOS. Meanwhile, the presence of adjacent humans decreases the amplitude of significant clusters nearly by half. The significant clusters which are widely observed are another important reason why the expected capacity and anti-fading ability in NLOS scenarios are superior to those in LOS.

4.5 Conclusion

This chapter presents experimental studying results for the impact of human body on massive MIMO indoor channels. It is found that human body has a great influence on both LOS and NLOS channels. It can increase the path loss exponents by 1 and reduce the ergodic capacity by 12% in LOS and 5% in NLOS cases. In LOS cases, such degradations are mainly due to the large power loss, and no significant improvement is observed in the correlation across Rx array and angular power maps. In NLOS cases, such degradations can partially be explained by the increasing power imbalance in multiple dimensions, the reduced Rx correlation and the attenuation of significant clusters caused by human body. Therefore, the influence of human body is significant in indoor massive MIMO channels and shall be considered in massive MIMO system design.

Chapter 5

SMV Off-Body Sparse Analysis and Channel Modeling

5.1 Introduction

This chapter devotes to SCM for centimetre-wave channels, using both practically measured and simulated single-input single-output dense multipath channels in the frequency band from 6 to 8.5 GHz. This frequency band is selected for the following reasons: (1) This band is proposed for being used in wireless body area networks in IEEE 802.15.6; (2) It is superior for demonstrating time-domain channel sparsity with the dense multipath channels resulted from its large bandwidth; and (3) There is a strong commonality for different bands from 3 to 10 GHz in terms of channel propagation properties [171, 172], and hence our work in this chapter can be generalized to other frequency bands, such as the WiFi and 5G mobile ones. With a 2 GHz bandwidth, the channels consist of a large number of resolvable multipath taps in the time domain, which can be represented directly by the TDL model. The original channel impulse response (CIR) can be downsampled with a low-pass filter to generate channels for systems with lower bandwidth if needed. In this chapter, we work on the high-resolution dense multipath directly and will show that there are great sparsity if we represent the CIRs using different dictionaries (aka, bases). One main challenge for SCM is that a sparse model can be affected by quite a few factors, such as the used dictionary, the reconstruction algorithm, and the required accuracy of modeling. Actually, the TDL model can also be treated as a special sparse model when insignificant multipath taps are ignored according to the desired accuracy. The dictionary will be a (partial) identity matrix in this case if represented in the time domain, or a partial Discrete Fourier Transform (DFT) matrix if represented in the frequency domain. But it is not an efficient sparse representation when the channel is rich in multipath. The sparsity is also largely affected by the used reconstruction algorithm with various complexity and the desired accuracy. Hence a good trade-off between sparsity, accuracy and complexity needs to be achieved. This trade-off will be investigated in detail in Section 6.2.

In this chapter, we provide a methodology for sparse modeling of time-domain channels and establish statistical sparse channel models. We aim to model (dense) multipath channels in a sparse and compact way, i.e., finding the base functions (called atoms in this chapter) and representing channels as a linear combination of these atoms, and using as fewer atoms as possible for a targeted modeling accuracy. The main advantages of our models can be summarized in the following three aspects: (1) High sparsity and efficiency owing to the use of dictionaries with balanced resolution and coverage in the time-domain; (2) Simplicity and easy to understand owing to the usage of model parameters analogous to conventional TDL models and the linkage of these parameters to physical properties of the channel; and (3) Flexibility with the usage of these decoupled channel parameters in channel modeling and simulation. Our main contributions are as follows:

- We provide a systematic methodology for centimetre-wave time-domain SCM based on compressive sensing techniques. It consists of the selection of dictionary and reconstruction algorithm, characterization of the statistics of sparse coefficients and verification of the developed statistical sparse model;

- We introduce a *triple equilibrium principle* to characterize the trade-off between sparsity, modeling accuracy, and reconstruction complexity in SCM setting. Using both measured and simulated channel datasets, we quantitatively demonstrate and practise the triple equilibrium principle in SCM. This principle provides an important guidance to selecting dictionary and reconstruction algorithm in SCM;

- We develop comprehensive statistical sparse channel models, including channel sparsity, dependency of sparsity on channels, magnitude decaying profile, sparse coefficient distribution, and sparse atomic index distribution, which are analogous to those in the conventional TDL model. Novel methods using ordered sparse coefficients and atomic index separation are proposed for statistical modeling;
- We mathematically establish the connection between parameters in the sparse channel model and conventional TDL model;
- We propose three channel synthesis methods for generating simulated SCM channels using the developed channel models. The effectiveness of the established sparse channel models is validated by comparing these generated channels with those actual ones.

The rest of this chapter is organized as follows. In Section II, we describe the channel datasets and our sparse modeling methodology. In Section III, we introduce the triple equilibrium principle and discuss the selection of the dictionary and reconstruction algorithms used for SCM in this chapter. In Section IV, we present detailed SCM results and investigate the connection between parameters for sparse and conventional channel models. In Section V, methods for generating simulated channels from the established sparse models are presented, and the generated channels are compared to the actual ones to verify the effectiveness of the sparse models. Section VI concludes the paper. Italic text is used to highlight important observations in this chapter.

5.2 Channel Datasets and Sparse Modeling Methodology

In this section, we introduce the channel datasets used in this work and present our sparse modeling methodology.

5.2.1 Tested Channel Datasets

We conduct the channel sparse modeling using two datasets, i.e., the practically measured off-body CIRs [49,173] and simulated wireless CIRs following the channel model proposed by IEEE 802.15.3a working group in [96].

Measured dataset

The channel data is measured in a typical hospital-type room with a few items of furniture. An omnidirectional monopole antenna is used to emulate the external access point (AP), and a wearable loop-dipole antenna worn on different positions of the volunteer is used to emulate the receiver (Rx). A vector network analyzer (cf. VNA Agilent 8720) is used to generate a 0 dBm, 801-point sweeping signal with the frequency ranging from 6 to 8.5 GHz. The off-body CIRs are observed in different body-worn parts and large-scale measurement locations. More details on the channel dataset and measurement can be found in [49,173].

According to the factors affecting the large-scale fading, the measured off-body channels are classified into three classes of datasets: body-parts-dependent (denoted as BAN_Parts), distance-dependent (BAN_Dis) and height-dependent (BAN_Hei) CIRs. Each CIR is denoised and normalized to unity energy. In one class of datasets, there may be measurements under different scenarios, for example, for BAN_Parts, there are measurements obtained from different body parts, and for BAN_Hei, measurements are from the AP placed at different heights.

Simulated CIRs

The simulated CIRs are generated from both the cluster-based model and TDL model. The cluster-based model follows the SV model in [97], and the TDL model is given by

$$h(t) = \sigma_0^2 \sum_{l=0}^{L-1} \alpha_l e^{-lT_s/\tau_{\mathrm{RMS}}} \delta(t - \tau_l), \tag{5.1}$$

where L is the total number of propagation taps, τ_l is the delay of l-th tap, τ_{RMS} is the Root Mean Square (RMS) delay spread and T_s is the sampling time, α_l is the fading coefficient of the l-th tap, and $\sigma_0^2 e^{-lT_s/\tau_{RMS}}$ represents an exponential power delay profile (PDP) of the taps, with $\sigma_0^2 = \frac{1-e^{-T_s/\tau_{RMS}}}{1-e^{-(L+1)T_s/\tau_{RMS}}}$ ensuring the average CIR energy is unity.

The simulated CIRs include four typical Case Models (CM), i.e., CM1 for 0-4 meters and Line of Sight (LOS), CM2 for 0-4 meters and none Line of Sight (NLOS), CM3 for 4-10 meters and NLOS, and CM4 for extremely bad NLOS with RMS delay spreads of 5.28, 8.03, 14.28 and 25 nanoseconds [96]. We consider various fading such as Rayleigh, Rician and Nakagami fading for the fading coefficients α.

5.2.2 Methodology for Sparse Channel Modeling

For a given sparse channel coefficient vector $\mathbf{x}_0$ of length N, *channel sparsity* here is referred to as either the absolute number of non-zero elements in the vector, given by $K = \|\mathbf{x}\|_0$, or the ratio given by K/N. We will use these two optional definitions interchangeably hereafter. If K or K/N is small (or large), we say the signal is sparser (or less sparse) and the sparsity is small/low (or large/high).

For any given samples of single-channel CIR $\mathbf{y} \in \mathbb{R}^M$, we can formulate the CS representation of the channel as

$$\mathbf{x}_s = \arg\min_{\mathbf{x}} \|\mathbf{x}\|_1, \quad \text{subject to } \mathbf{y} = \mathbf{\Phi\Psi x} + \mathbf{r}. \tag{5.2}$$

where $\mathbf{x}$ is the sparse coefficient vector, $\|\mathbf{x}\|_1$ is norm-1 of $\mathbf{x}$, i.e., the sum of absolute values of the elements in $\mathbf{x}$, $\mathbf{\Phi} \in \mathbb{R}^{M\times N}$ $(M \leq N)$ is the measurement/sensing matrix, $\mathbf{\Psi} \in \mathbb{R}^{N\times N}$ is the dictionary, and $\mathbf{r}$ is the residual vector representing noise and/or residual errors in the sparse approximation. There are a number of CS algorithms such as Orthogonal Matching Pursuit (OMP), L1-minimization and Bayesian compressive sensing, that can be applied to solve the optimization problem in (5.2). Different algorithms have different complexity and different reconstruction accuracy.

We have full datasets for the originally simulated and measured channels, sampled at the Nyquist rate. We can design the sensing matrix $\mathbf{\Phi}$ with M much smaller than N, to mimic what is in the practical channel estimation situation. However, this may make the SCM results lose generality. So instead, we use all the channel samples in $\mathbf{y}$ directly for SCM, without using $\mathbf{\Phi}$.

Our SCM methodology consists of three major stages, which are summarized next and will be detailed in the following sections.

- The first stage is the *selection of dictionary and reconstruction algorithms*. From the formulation in (5.2), we can see that the sparsity k is closely related to three factors, the product $\mathbf{\Phi\Psi}$ (or just the dictionary $\mathbf{\Psi}$ in this chapter), the reconstruction algorithm, and the constraint of residual vector $\mathbf{r}$ (i.e., the desired the accuracy). Understanding the trade-off between these factors is an important step in SCM. In Section 6.2, we introduce the triple equilibrium principle to elaborate the trade-off and discuss how to select appropriate dictionaries and CS reconstruction algorithms.
- The second stage is *sparse channel modeling* as will be detailed in Section 5.4. In this stage, analogous to the parameters in the TDL model including significant MultiPath Components (MPC), PDP, small-scale fading, and delay, we analyze the statistics for sparsity, Magnitude Decaying Profile (MDP), distribution of sparse coefficients, and distribution of atomic indexes. Thus a complete statistical sparse channel model is established.
- The third stage is *sparse channel validation*, as will be detailed in Section 5.5. During this stage, we stochastically generate the sparse coefficients and atomic indexes using the developed statistical sparse channel models, and compare the generated channels with the original measured and simulated channels from which the statistical sparse models are developed. This process is used to validate the effectiveness of the developed models.

5.3 Triple Equilibrium Principle and Selection of Dictionaries and Reconstruction Algorithms

In this section, we first introduce the *triple equilibrium principle* for characterizing the trade-off between sparsity, modeling accuracy and complexity in SCM. We then discuss how we select the dictionary and reconstruction algorithms to achieve a trade-off under the guidance of the principle, by investigating the actual impact of the trade-off on SCM.

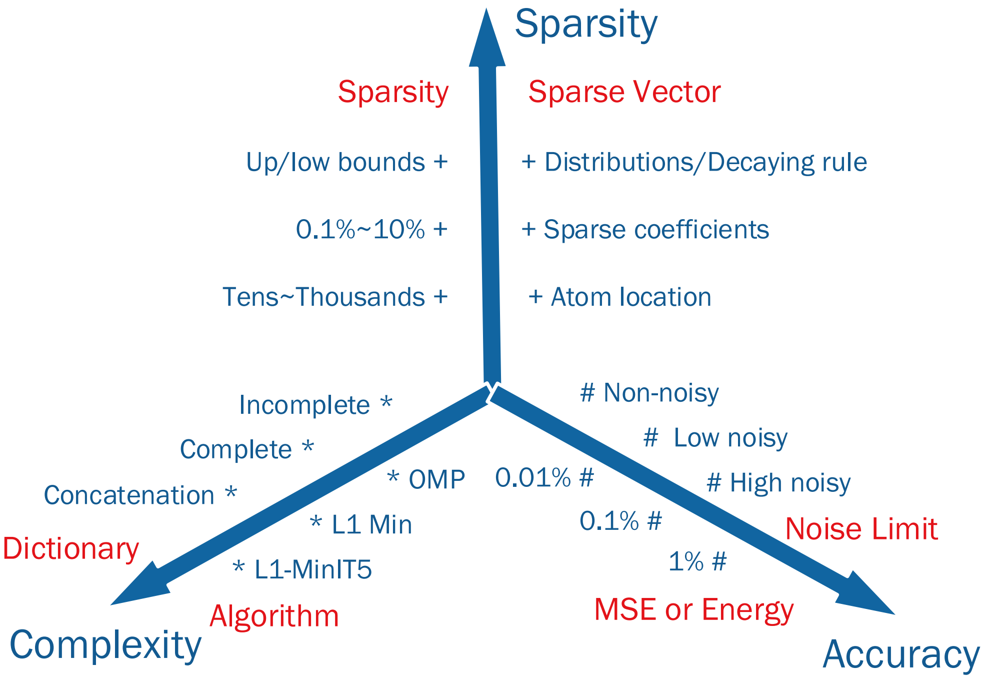

Figure 5.1: The triple equilibrium relationship among sparsity, complexity and accuracy.

5.3.1 Triple Equilibrium among Sparsity, Complexity and Accuracy in SCM

In the sparse channel modeling, we will consider the interaction and tradeoff between channel sparsity, reconstruction complexity and accuracy. Reconstruction complexity and accuracy are associated with, e.g., the reconstruction algorithms, times of iterations used in the algorithms, the adopted dictionary and its size, and the number of measurements. According to many important research results on compressive sensing including the classic work in [100], the sparsity, reconstruction complexity and accuracy interact with each other. Generally, the sparsity of practical signals can change with the required reconstruction accuracy and the affordable complexity and the changes can be significantly different for different signal sources.

For sparse channel modeling, we hence keep in mind the triple equilibrium relationship among sparsity, complexity, and accuracy as illustrated in Fig. 5.1. Firstly, the achievable channel sparsity is expected to grow from smaller to larger when the required reconstruction accuracy increases and/or the required complexity decreases. Secondly, to achieve a given sparsity level, e.g., 5% sparsity ratio, the sparser the actual signal is, the lower the reconstruction complexity will be to attain certain reconstruction accuracy. Thirdly, there is a tradeoff of computing complexity between the selected recovering algorithm and dictionary. Fig. 5.1 lists the incomplete, critical complete, concatenation dictionaries and recovering algorithms such as greedy algorithm (like OMP), optimization algorithm (ℓ1-Minimization denoted as ℓ1-Min.) and the iterative algorithm (5 step reweighted ℓ1-Minimization denoted as ℓ1-MinIT5) from low to high complexity. It is observed in [174] that with 3 to 5 concatenation dictionaries, even the simplest OMP algorithm can achieve better performance than the optimal algorithm such as iterative ℓ1-MinIT5. Finally, it is noted that the de-nosing ability of CS algorithms can also have a great impact on the reconstruction accuracy. Measurement noise can be the upper limit of sparse processing ability.

The triple-equilibrium relationship in sparse channel modeling will be explored in detail in Section 5.4.1 and 5.3.3.

5.3.2 Impact of Dictionary on Sparse Channel Modeling

Dictionary can have a significant impact on the sparsity and reconstruction accuracy of a general CS problem, as well as our sparse channel modeling. For example, in our experiments, it is widely observed that to achieve similar modeling accuracy, the sparsity for recovering the same BAN_Part CIR using the ℓ1-Min algorithm are 17, 18, 72, 94 and 210 for the symlet 4 level 5 wavelet (denoted as *symlet 4-5* hereafter), exponential, truncated cosine wave, Fourier and random Gaussian dictionaries, respectively. The wavelet and exponential dictionaries exhibit much lower sparsity than the others. This is because their fast-fading atoms adapt to the sparse properties of significant clusters, i.e., the properties of compact support and locality have advantages in representing the cluster characteristics. The observation here is consistent with the quantitative dictionary selection formula and the results shown in [175]. So we will mainly present the sparse channel modeling results using wavelet and exponential dictionaries in this chapter.

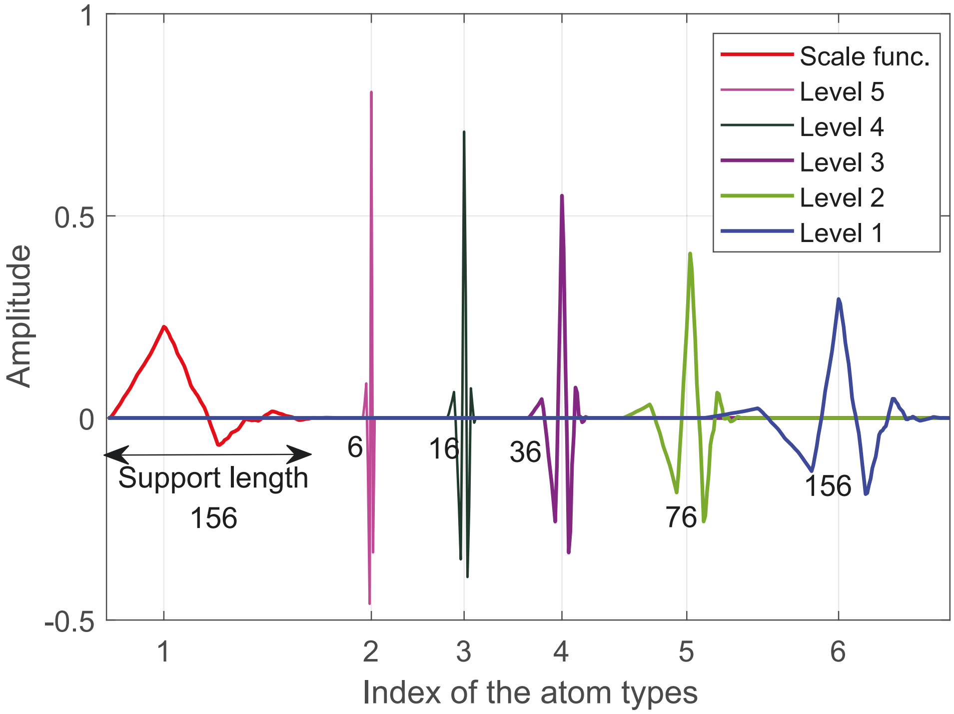

Figure 5.2: Waveforms for six types of atoms in the symlet 4-5 dictionary. For the index of atom types, the first (with index 1) is the father wavelet, the last (with index 6) is the mother wavelet and the child wavelets ranging from level 2 to 5 are indexed as type 5 to 2. The number next to each waveform denotes the support length of the wavelet.

The k-th atom in the exponential dictionary is defined as

$$d_k(t) = \begin{cases} \sqrt{1-\beta^2}e^{-\beta t}, \ t \geq k \\ 0 \qquad\qquad\quad ,0 \leq t < k \end{cases} \tag{5.3}$$

where the fading parameter β decides the shape of the atom. Different exponential dictionaries have different values of β. Hence all atoms in the same exponential dictionary are time-shifted version of a basic one and have the same waveform. Fig. 5.2 depicts the compact support length and waveforms for six atoms of the symlet 4-5 dictionary. Waveform 1 is the scale (father) wavelet of Symlet 4, and waveforms 2 to 6 are the different scales of level 5 to 1 of the mother wavelet. These waveforms also have good quasi-orthogonal characteristics. Such versatile waveform combinations make wavelet dictionary adapt to different signal types including the clustered channels.

Fig. 5.3 and 5.4 illustrate the original, recovered and residuals of one BAN_Part CIR using

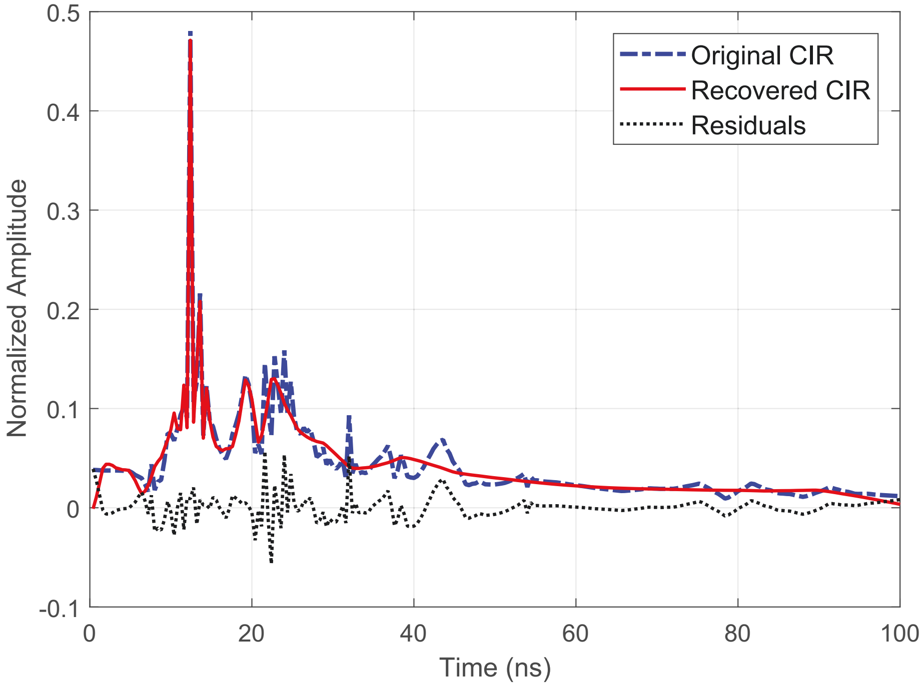

Figure 5.3: Comparison of original, recovered and residual signals using wavelet dictionary and OMP algorithm (Sparsity $K = 20$).

different dictionaries and CS algorithms. The combination of wavelet-OMP and exponent-$\ell1$-Min both perform well, achieving similar sparsity levels around 20 under the same MSE of 10^{-4}. It is noticed that the exponential dictionary achieves less accurate results in the segment of the primary cluster, compared to the wavelet dictionary. This is mainly caused by the inflexibility of using fixed waveform in the exponential dictionary. The channels in the segment of the primary cluster usually change rapidly. Hence exponential functions with a fixed waveform cannot approximate such channels well. Comparatively, wavelet atoms of different width can be flexibly "selected" to approximate the channels, achieving higher accuracy.

Of course, the single-shape exponential dictionary also has its unique advantages. For example, if using combined exponential dictionaries with three different β values, the sparsity can be reduced to 10 taps [176]. This mainly benefits from the introduced dynamic resolution capability by the combined dictionaries. But the problem is that it is hard to know which β values and dictionaries should be combined, unless some prior information on the β values is available. In contrast, the improvement is insignificant by combining multiple wavelet dictionaries. This is

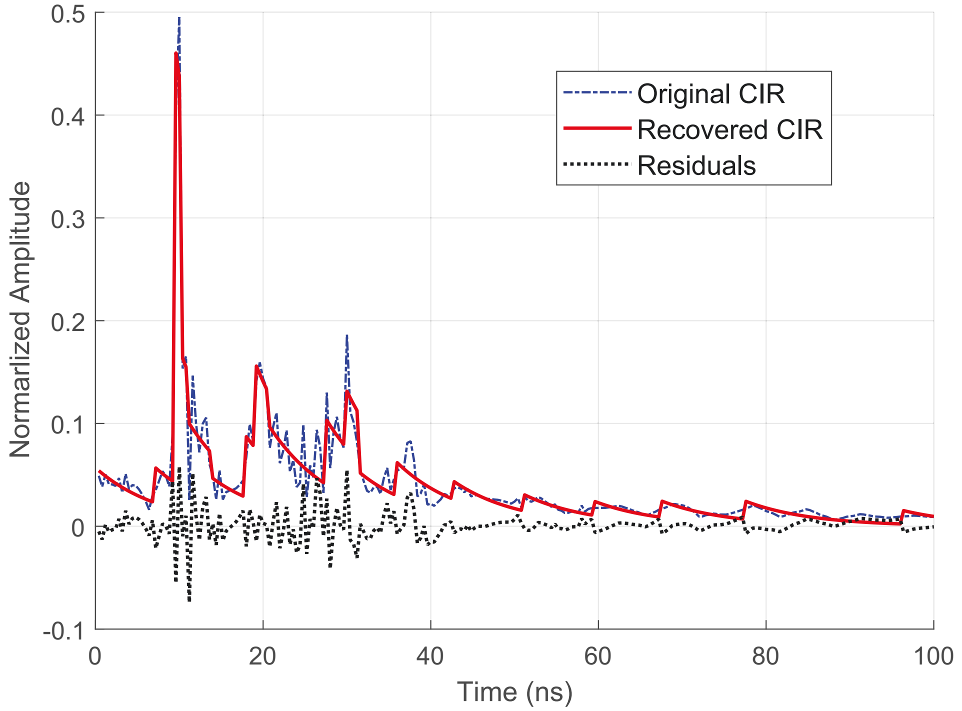

Figure 5.4: Comparison of original, recovered and residual signals using an exponential dictionary and ℓ1-Minimization algorithm (Sparsity $K = 18$).

because a wavelet dictionary is already well defined with excellent complementary completeness and multi-scale characteristics. The benefit of improved fitting accuracy with using additional wavelet dictionaries can be counteracted by the high atom correlation they introduce. Thus, it is important to select/train adaptive projection atoms to form dictionaries for specific signals.

The reason why we chose linear unit over logarithmic expression is that sparse model expects to fit strong principal diameter signal, while logarithmic unit expression weakens the main signal and emphasizes small signal components, which will lead to misleading in many sparse representing scenarios, as the main component is good enough and the weak tail signals needs to be improved.

5.3.3 Sparsity-Complexity Relationship Under Fixed Accuracy

The achievable channel sparsity can be affected by different reconstruction algorithms for the same residual error, according to the sparsity-accuracy analysis in Section 5.4.1. Different algorithms, or the same algorithm with different iterations, can have very different complexity. Here, we quantitatively analyze the complexity associated with sparse channel modeling and reconstruction, using the $\ell 1$-Min and its iterative algorithms as examples. The required multiplications for $\ell 1$-Min and $\ell 1$-Min ITq are $O(qMN^2), O((T+1)qMN^2)$, where T is the number of iteration or reweight times, and $T = 0$ for $\ell 1$-Min [88].

Fig. 5.5 depicts sparsity variations for many BAN_Parts CIRs, using $\ell 1$-Min reconstruction algorithms with iterations ranging from 0 to 10. For all datasets, the mean sparsity decreases as the iteration number increases, and the first iteration always achieves the largest sparsity reduction. The average sparsity value for a particular dataset also quickly converges, and further increasing the number of iterations only leads to a negligible reduction on sparsity. For all datasets, the number of iterations up to 5 is shown to be sufficient. We can also see that all CIRs under LOS conditions have lower sparsity than those under NLOS cases. Similarly, experimental results for simulated CM1-4 channels lead to an average sparsity of 7, 9, 14 and 25 taps, respectively, which is in line with the trend of the increasing RMS delay spread (5, 8, 14, 25 nanoseconds). The connection between the average sparsity and RMS delay will be mathematically shown in 5.4.4.

5.3.4 Summary of the Triple Equilibrium Principle

It is found that the residual error in sparse modeling exponentially decreases with the desired sparsity increasing, and the desired sparsity can be reduced up to certain bounds at the cost of linearly increasing complexity. The triple equilibrium among sparsity, complexity, and accuracy is thus qualitatively verified. It is nearly impossible to improve any one without impacting the other two.

In the next section, we use the selected wavelet and exponential dictionaries and the algorithm sets (OMP, $\ell 1$-Min and $\ell 1$-Min ITq) to conduct SCM for both measured and simulated CIRs.

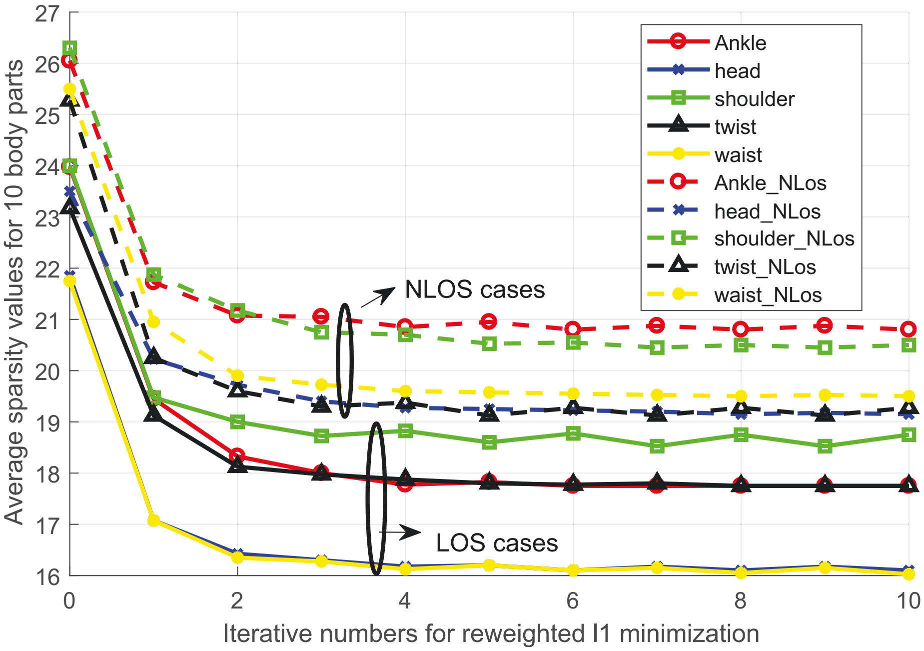

Figure 5.5: Sparsity variation for ten body parts CIRs reconstructed using the symlet 4-5 dictionary and reweighted $\ell 1$ minimization algorithms with 0 to 10 iterations.

5.4 Sparse Channel Modeling

In this section, we conduct detailed sparse channel modeling, focusing on sparsity, MDP ("cluster fading rule") and atomic index distribution (cluster occurrence time), which have analogies in conventional TDL modeling. We will also investigate the dependency of sparse coefficients on channel parameters.

Ideally, we would like to investigate the MDP and fading for each sparse coefficient corresponding to each atom (column) in the dictionary. This will give us the results directly analogous to the TDL modeling. However, this is hard to do for the following reason: the size of the dictionary could be very large and there are frequently insufficient samples for a number of coefficients due to limited measured datasets. The fluctuation of atomic indexes can largely reduce the reliability of obtained sparse statistics. Some dictionaries do not have clear physical meanings, which also makes direct processing not necessary. On the other hand, organizing the non-zero taps in proper order is found to be able to better reveal the statistics of sparse signals [177]. Therefore in this chapter, we organize the obtained sparse channel coefficients in descending order according to their magnitudes and conduct MDP and fading analysis based on the ordered coefficients. At the same time, we collect the atomic indexes for these coefficients and propose an *atom-index-division method*, which will be detailed in Section 5.4.3, to obtain the statistical distribution for the indexes of these ordered coefficients.

5.4.1 Sparsity

We characterize the channel sparsity and investigate its dependency on accuracy and types of channels. We will demonstrate in Section 5.4.1 that the sparsity and reconstruction accuracy are bonded, and their relationship can be well characterized by an exponential function. We will show in Section 5.4.1 that the sparsity also varies from channel to channel as expected, and is dependent on statistical fading distributions.

Dependency of Sparsity on Reconstruction Accuracy

The required sparsity in channel modeling has a direct impact on the accuracy, and vice verse. In [176], it is theoretically proved that the residual energy for any sparse approximation is linearly bounded by the residual of the best sparse approximation. Such a boundary constraint, however, is often very loose for practical sparse reconstruction algorithms, and is also dependent on the actual dataset. In our work, to understand this relationship and its impact on sparse channel modeling, we conducted various signal recovery experiments using different sparsity constraints, different datasets, dictionaries and recovery algorithms. Next, we present some exemplified results.

Fig. 5.6 shows the relative energy of the reconstructed signal and the residual (error) between the reconstructed and original signals, normalized to the original signal power. The dataset includes 400 measured BAN_Dis CIRs. The sparse signal is reconstructed using the symlet 4-5 dictionary and the OMP algorithm. Due to the unit energy constraint and the Restrict Isometric Property (RIP) property of wavelet dictionary, the energy of the reconstructed signal, represented by the sparse coefficients, increases with the sparsity increasing steadily, while the residual error steadily declines.

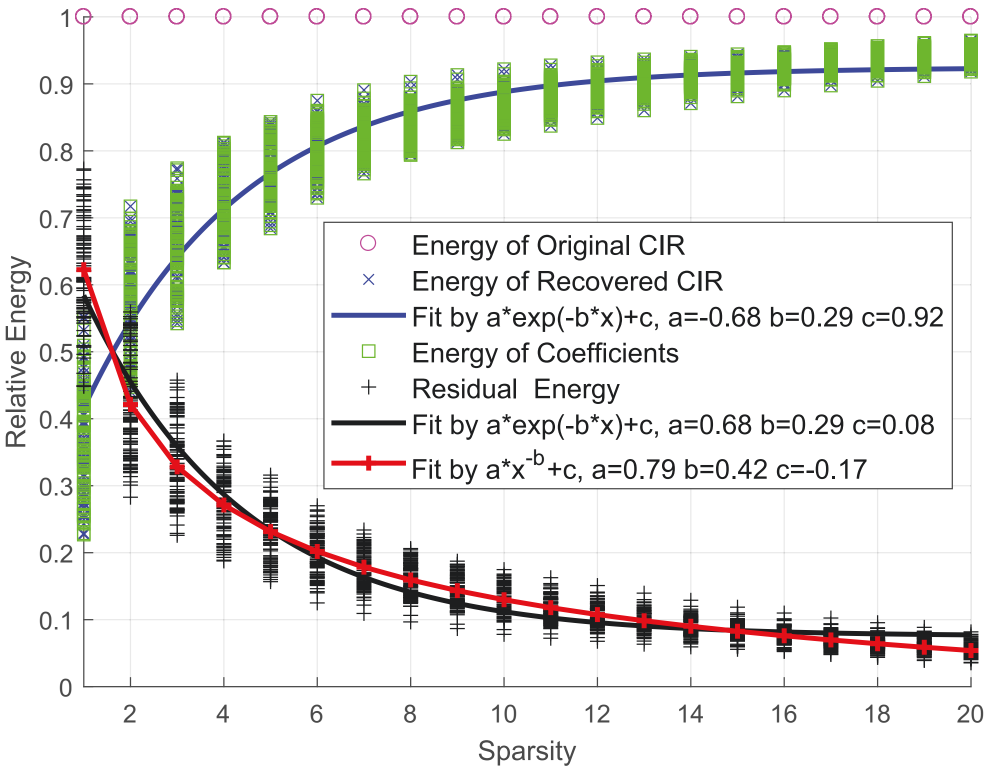

Figure 5.6: Relative energy of reconstructed and residual signals for measured BAN_Dis CIR subset using wavelet dictionary and OMP algorithm.

Table 5.1: Parameters of exponential fitting function for residual energy for different dictionaries and algorithms.

Cases	Dictionary	Algorithm	a	b	c
BAN_Parts	Wavelet	ℓ1-Min	0.51	0.11	0.12
BAN_Hei	Wavelet	ℓ1-Min	0.58	0.14	0.15
BAN_Dis	Wavelet	ℓ1-Min	0.49	0.12	0.12
	Wavelet	OMP	0.68	0.29	0.08
	Exponent	OMP	0.43	0.25	0.08
Sim_Rayl	Wavelet	ℓ1-Min	0.39	0.20	0.05
	Wavelet	OMP	0.76	0.45	0.07
	Exponent	OMP	0.35	0.50	0.06
Sim_Rice	Exponent	OMP	0.27	0.65	0.08
Sim_Naka	Exponent	OMP	0.28	0.61	0.06

Plotted together in the figure are the exponential and polynomial curve fitting functions. Using the Akaike Information Criteria (AIC) [178], it is found that the relative signal and residual energy can both be well fitted by the exponential function given by

$$\delta_{Res} = ae^{-bk} + c, \tag{5.4}$$

where δ_{Res} is the residual energy and k is the desired sparsity. The polynomial (or power) function $\delta_{Res} = ak^{-b} + c$, which is widely used to bound residuals [176], is also found to provide good fitness here.

To summarize, it is found that *the exponential function can fit well with the residual energy for almost all measured and simulated datasets*, for different channel fading distributions, dictionaries or algorithms. Table 5.1 presents the parameters of the exponential fitting function for the residual energy for different dictionaries and algorithms. In our experiments, we observed that for simulated channels, the fitting accuracy is low when the sparsity is large when larger decaying exponents (parameters b in (5.4)) are obtained, especially for Rician or Nakagami fading channels. This indicates that simulated channels with simpler multipath structures such as a dominating LOS component usually leads to smaller residual-sparsity product and hence better recovery performance.

According to the MSE metric $E_{\mathrm{MSE}} = E_{Res}/M$, $E_{\mathrm{MSE}} = 10^{-4}$ is equivalent to the residual energy of 5% with the number of measurements $M = 500$ in most cases. Fig. 5.6 indicates that the 5% residual error corresponds to an average sparsity between 18 and 20, or 4% sparsity ratio. We use 4% sparsity ratio ($E_{\mathrm{MSE}} = 10^{-4}$) as a baseline for distribution analysis in this chapter. The CIR modeling for all pairs of residual error and sparsity can be implemented as long as they are above the asymptotic line indicated by (5.4).

Dependency of Sparsity on Channels

Fig. 5.7 presents the Cumulative Probability Distributions (CDFs) of reaching the desired sparsity for different algorithms. Results for using all the measured data sets and for using specific data sets (waist only and ankle only) are presented for comparison. Each curve is obtained from over 4000 sparse reconstruction experiments. When all the measured datasets are used, the curves for algorithms ℓ1-Min, ℓ1-Min IT1 and ℓ1-Min IT5 using the same wavelet 3-5 dictionary can be well fitted by Gaussian functions with decreasing mean and variance

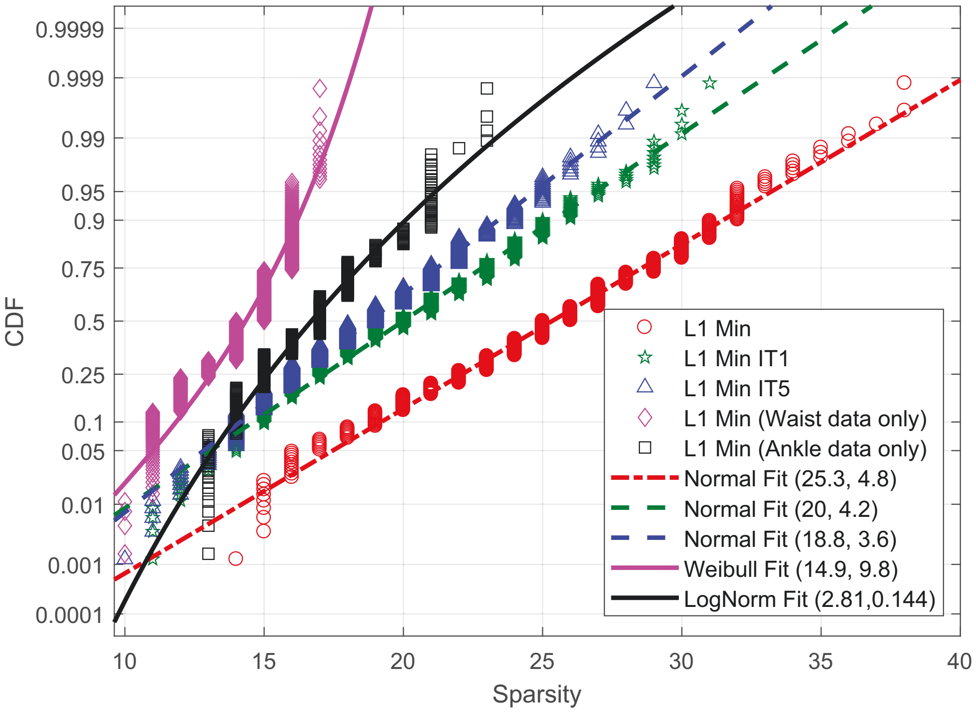

Figure 5.7: CDFs of the recovered sparsity for different reconstruction algorithms and measured channel data using Symlet 4-5 dictionary. For the first three curves (ordered according to the legends), all measured datasets are used; while for the rest two, only specific datasets for waist and ankle are used respectively.

values. We can also see that using recovery algorithms with more iterations can effectively reduce the mean sparsity and reduce the fluctuation of sparsity. Generally the smaller the sparsity fluctuation is, the smaller the modeling error will be. Thus for a selected dataset, there is a tradeoff between the complexity of the recovery algorithm and the accuracy of the modeling. For waist only and ankle only dataset, the CDF follows distinct distributions due to reduced variation of the sparsity. For example, the CDF for waist and ankle datasets follows Weibull and Log-Normal distributions respectively. Compared to the results of full dataset, the sparsity is reduced as can be seen from the CDF curves.

Fig. 5.8 compares the CDFs for simulated Rayleigh, Rice and Nakagami fading channels using the same wavelet dictionary and OMP algorithm. The sparsity of Rayleigh fading channels has a maximum mean value of 17 taps and the largest sparsity variation. The mean sparsity for Rician fading CIRs gradually decreases from 17 taps (nearly the same with Rayleigh fading

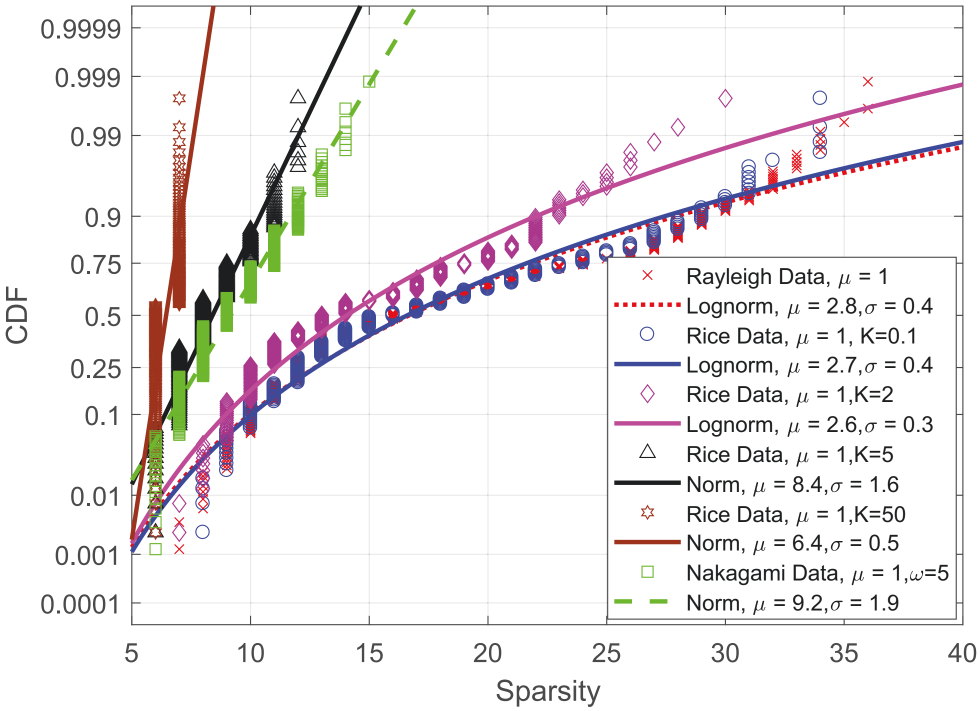

Figure 5.8: CDF of the sparsity for simulated fading channels with different parameters.

channel) to only 7 taps, with the Rician K-factor changing from 0.1 to 50. Under the same LOS condition, Nakagami fading channel is less sparse than similar Rician channels (curves marked in black triangles). It seems that the channel condition has a notable effect on sparsity distributions, and channels with larger LOS components demonstrates lower sparsity.

As a summary for the sparsity of studied channels, it is found that *an average sparsity of 25 for the measured CIRs and 20 for simulated cases are the least values for most cases* with different dictionaries, algorithms and channel conditions. The maximum sparsity is 38, which correspond to the sparsity ratio of 7.6%, for a total of $M = 500$ samples. This reflects the great advantage of compressed channel sampling over traditional Nyquist sampling method.

5.4.2 Statistics of Sorted Sparse Coefficients: MDP and Coefficient Distribution

We now characterize the statistics of the sorted sparse channel coefficients, including the *MDP* and *coefficient distribution*. There are good analogies between them and the statistics of conventional TDL model. The MDP and coefficient distribution correspond to the power delay profile (PDP) and small-scale fading in TDL models, respectively. The main difference is that the statistics of sparse coefficients could be dependent on the dictionaries and is also slightly related to the reconstruction algorithms.

The MDP of sorted sparse channel coefficients can be well described by the following exponential function of the index of these coefficients:

$$C_i = a\, e^{b\, i} + c \tag{5.5}$$

where $i \in [1, K]$ is the index of the i-th largest sparse coefficient, and a, b and c are respectively the intercept, attenuation rate and attenuation residual parameters that can be obtained via curve fitting. Note that (5.5) is different to (5.4) in the physical meaning of these parameters. As have been shown in Fig. 5.6 in Section 5.4.1, the energy of the coefficients for different atoms (i.e., columns in a dictionary) are very unbalanced. The maximal non-zero coefficient (generally the first output in the OMP algorithm) contains around 40% of the total energy, but the 10-th only occupies 0.2%. This is mainly due to the exponential decaying laws for sorted sparse coefficients as discussed in Section 5.4.1. In Fig. 5.9, we show another example for sorted sparse coefficients for four typical channel datasets, using different reconstruction algorithms. The figure shows that, for all measured and simulated channels, their MDPs can be well characterized by exponential functions. For the two measured channels, different reconstruction algorithms have an insignificant impact on the decaying speed.

Since the coefficients in the exponential function are found to be very similar for different datasets in the same class, we aggregate the sparse coefficients in the same class for analysis, to make the model more general. Fig. 5.10 shows the MDP of the sorted sparse coefficients for the aggregated BAN_Dis datasets. They are shown to be well fitted by three exponential functions with similar parameters. More advanced algorithms, such as L1_IT5 generally achieves better

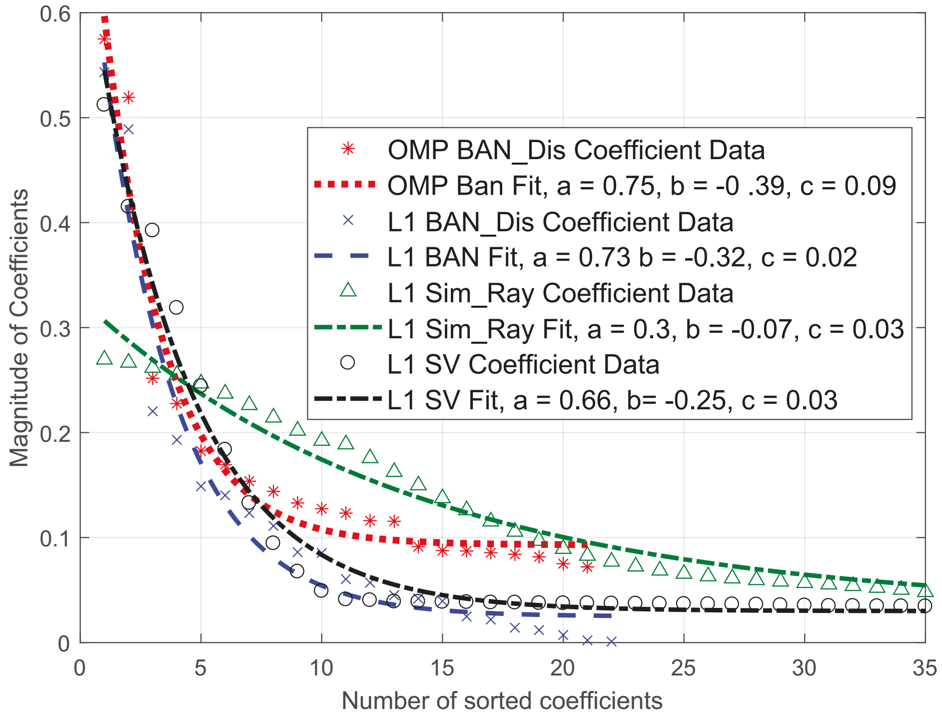

Figure 5.9: Exponential fitting for sorted sparse coefficients in different datasets and algorithms using symlet 4-5 dictionary.

fitness with a smaller tail.

The sparse coefficients with the same index for the same class of datasets are also found to have similar CDFs. Hence we also aggregate all the datasets in each class and analyze their CDFs. Fig. 5.11 illustrates the CDF for the 10-th largest sparse coefficient in different classes of datasets. The figure shows that for all datasets and all reconstruction algorithms, the CDF can be well approximated by that of Normal distribution. Similar matching distribution has been observed for other sparse coefficients. This indicates that *the magnitude of sparse channel coefficients experience "Gaussian fading" - the variation of magnitude can be characterized by a Gaussian function.*

5.4.3 Statistics of Atomic Indexes for Sparse Channel Coefficients

Corresponding to the ordered sparse channel coefficients, we study the statistical properties of their atomic indexes. Due to the large size of the sparse vector, there could only be a small

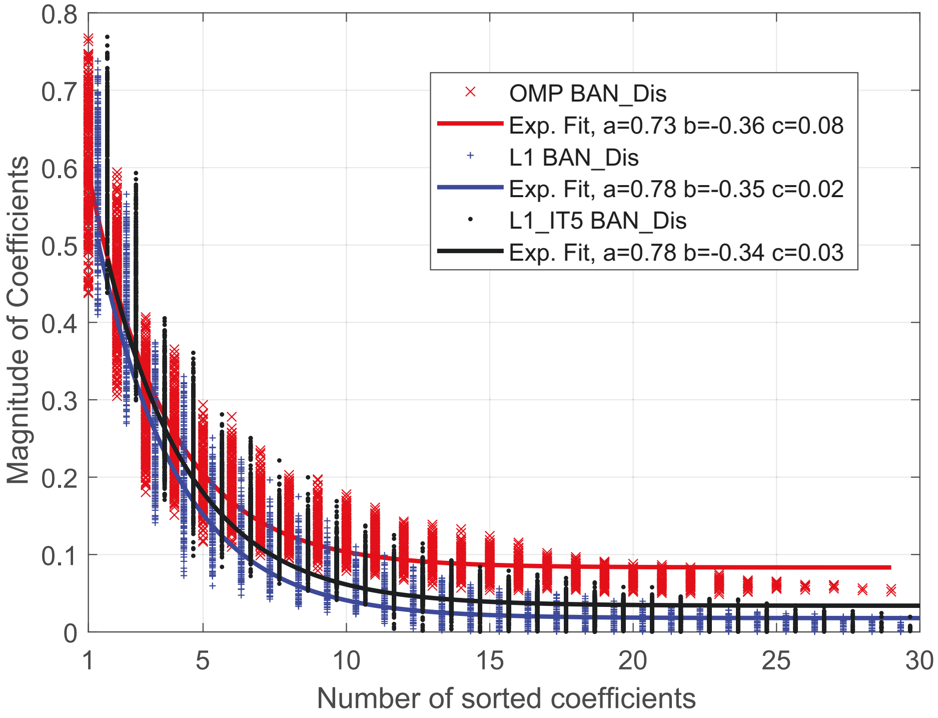

Figure 5.10: MDP of aggregated datasets and the fitting by exponential functions for three reconstruction algorithms with the symlet 4-5 dictionary.

number of samples for each index associated with the ordered channel coefficients. For example, for a channel of length 500, the index set for the 3rd sorted sparse coefficients is found to be concentrated on atom 1 and 6, i.e., father wavelet and level-1 mother wavelet in (5.2). Therefore directly looking into the statistics for each index will lead to inaccurate results.

Instead, inspired by the wavelet structure, we propose an atom-index-division method which splits any atomic index into a *shape factor* and a *location ratio factor*. This is represented by

$$\omega_i = \gamma_i \, \iota_p + \iota_p^{\mathrm{Beg}} \tag{5.6}$$

where ω_i is the original atomic index corresponding to the i-th sorted non-zero sparse coefficient, p is the shape factor, γ_i is the corresponding location ratio factor, and ι_p and ι_p^{Beg} are the length and the beginning number of Shape p atoms. It is found that different dictionaries in the same wavelet class only causes slight changes to the specific values of ι_p and ι_p^{Beg}, without significantly affecting the statistics of the two factors. Similarly, concatenating another sub-dictionary to the existing dictionary (such as wavelet 3-5) only adds 1 to the shape factor, without dramatically

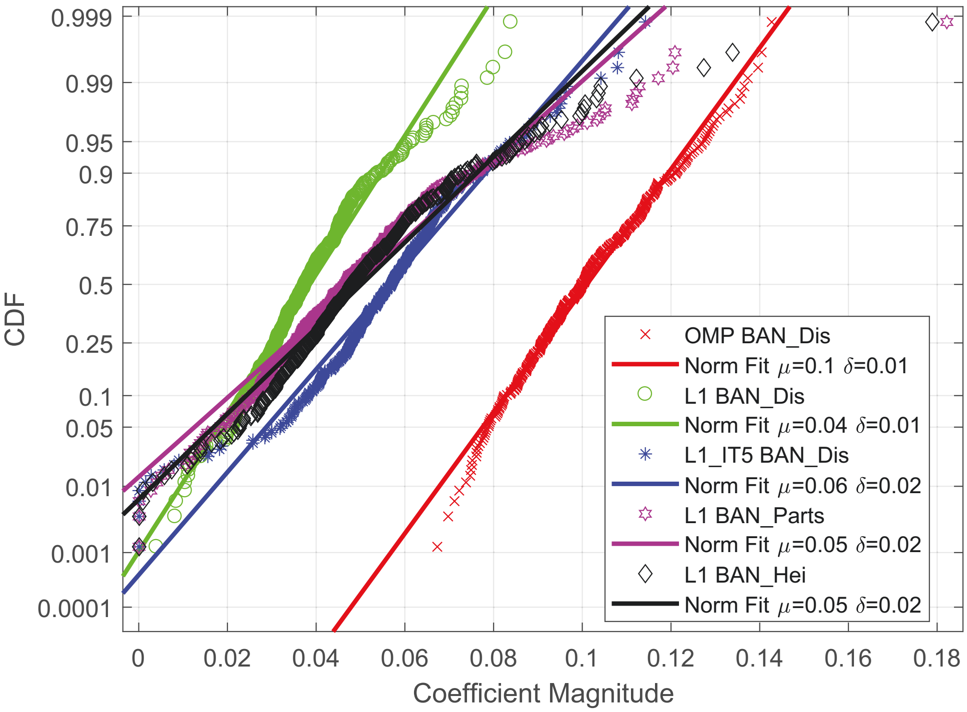

Figure 5.11: CDF of the 10-th ordered sparse channel coefficient for different classes of datasets and algorithms using symlet 4-5 dictionary. “Norm Fit” is short for fitting with Normal (Gaussian) distribution.

changing the ranging and mean value of the two factors. This is partially due to that different dictionaries in the same wavelet class have similar waveform, vanishing moment and supporting length. More importantly, this is a result of the parameter-decoupling effect achieved by the proposed SCM method, where the shape, occurrence time and energy of the channel clusters are separately mapped into the atom index shape factor, location ratio factor and non-zero sparse coefficients. This leads to robust models that are insensitive to small variation of channels or dictionaries.

To better illustrate this concept, in Fig. 5.12 we provide an example for the atom-index-division method using the symlet 4-5 dictionary. The selected atomic index is 225 in the whole dictionary, and it belongs to the Shape 2 atom types and locates at the 0.8 ratio in all Shape 2 atoms. Thus, the atomic index of 225 is divided into the shape factor $p = 3$ and the location factor $\gamma_i = 0.8$.

Compared to directly working on the statistics of non-zero atomic indexes, the proposed

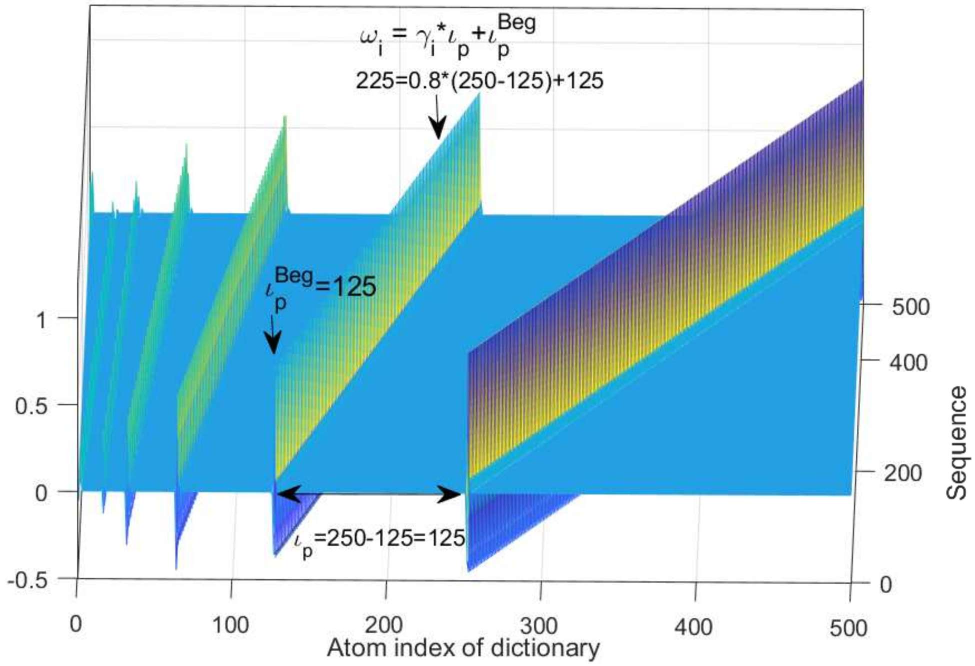

Figure 5.12: An example of the atom-index-division method using the symlet 4-5 dictionary. The selected atomic index is 225 in the whole dictionary with the shape factor $p = 3$ and the location factor $\gamma_i = 0.8$.

atom-index-division method has three advantages: 1) It needs fewer samples but provides better distribution fitness; 2) It can provide more stable statistical results for scalable dictionaries; and 3) It provides deeper insights into propagation characteristics (e.g., the location ratio factor can be transformed to tap delay of a specific atom).

Figs. 5.13 and 5.14 depict the statistics of shape factor and location ratio factor for wavelet 3-5 dictionary under different scenarios, respectively. The shape values for different scenarios and recovery algorithms all follow half-Normal distributions. Compared to the OMP algorithm, the $\ell 1$-Min and its iterative methods tend to have a higher probability of selecting shape-1 wavelet atom (i.e., father wavelet) and lower probability of selecting high-level wavelets. No significant distinctions are observed among different scenarios. Similarly, the location ratio factors for different algorithms and different datasets all follow the log-Normal distribution very well. Compared to the OMP algorithm, the $\ell 1$-Min iterative algorithms have a higher probability of generating high location-ratio-factor values. This is likely caused by the different

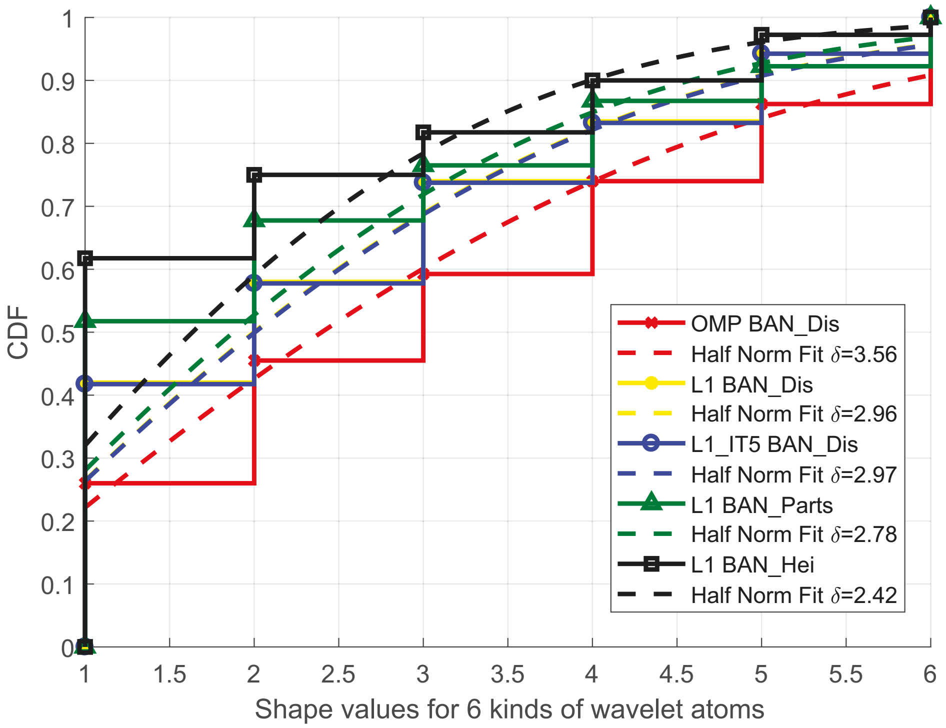

Figure 5.13: Distributions of the shape-factor values of the 10-th sorted sparse coefficient for different datasets and algorithms using the symlet 4-5 dictionary.

properties of the two CS algorithms. The OMP algorithm finds non-zero solutions serially, starting from the larger sparse coefficients. Since multipath/clusters with larger power arrive earlier in the time domain, they will be picked up earlier by the OMP algorithms, compared to those arriving later with smaller power. Comparatively, the ℓ-1 iterative algorithm finds the non-zero coefficients in a parallel way, and during this process, there is no prejudice to high-power cluster/multipath. Therefore, the location-ratio-factor values obtained by OMP, which correspond to the occurrence time of clusters, tend to be larger than those obtained by ℓ-1 iterative algorithm.

5.4.4 Relationship between Sparse Coefficients and Propagation Parameters

There are some close correlations between the significant sparse coefficients and some major propagation parameters, such as the significant MPCs, mean delay and RMS delay in the TDL

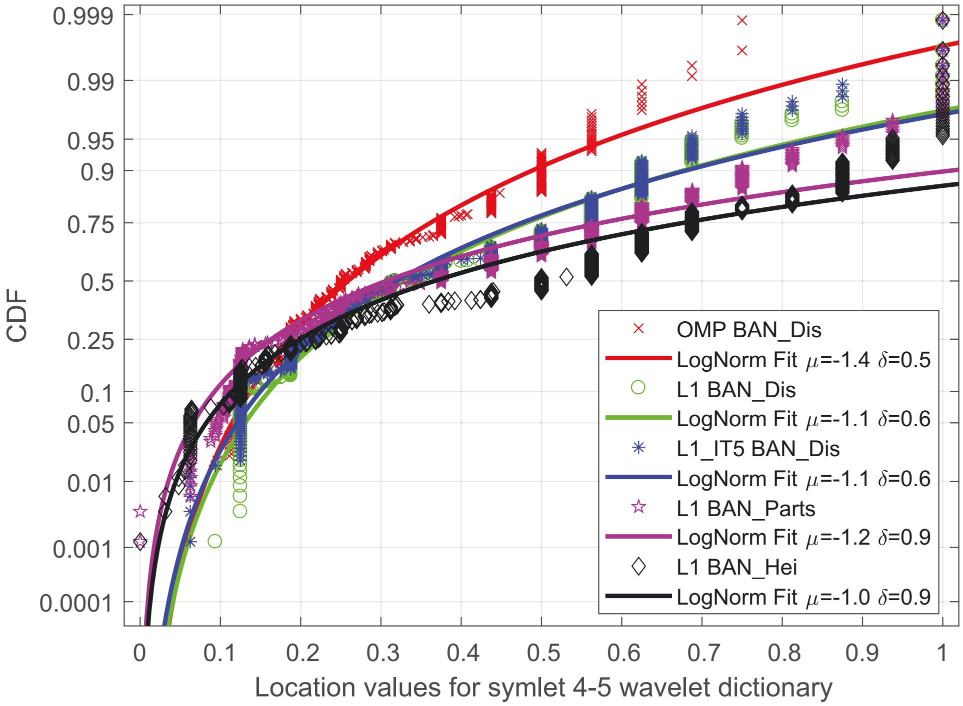

Figure 5.14: Distributions of the location-ratio-factor values of the 10-th sorted sparse coefficient for different datasets and algorithms using the symlet 4-5 dictionary.

model. The significant MPCs are defined as the number of multipath in the TDL model with a power larger than the set threshold. The correlation between the channel sparsity and the mean delay and RMS delay can be mathematically established below.

According to the TDL and sparse channel models, we can relate the mean delay to the sparse parameters via

$$\begin{aligned}\overline{\tau} = \frac{\sum \tau_i P(\tau_i)}{P(\tau_i)} &= \frac{r_0 \mathbf{Tr}(\mathbf{D_M}(\mathbf{Ax})(\mathbf{Ax})')}{1-\delta_{Res}} \\ &= \frac{r_0 \mathbf{Tr}(\mathbf{xx'A'D_M A})}{1-\delta_{Res}} \\ &\approx \frac{r_0 (\mathbf{x'D_M x}) \mathbf{Tr}(\mathbf{A'A})}{1-\delta_{Res}} \\ &\approx \frac{r_0 \mathbf{Tr}(\mathbf{A'A})}{1-\delta_{Res}} \sum_{j=1}^{K} \omega_j x_j^2, \end{aligned} \tag{5.7}$$

where $P(\tau_i)$ is the power of the i-th tap, r_0 is the time resolution for sampled CIR signals, $\boldsymbol{D}_M$ is a diagonal matrix with the diagonal elements $\{1, 2, ...M\}$, x_j^2 is the non-zero sparse coefficient and its corresponding atomic index is ω_j.

The RMS delay spread can be represented by

$$\begin{aligned}
\tau_{\text{RMS}} &= \sqrt{\frac{\sum \tau_i^2 P(\tau_i)}{P(\tau_i)} - \overline{\tau}} \\
&= \sqrt{\frac{r_0^2 \mathbf{Tr}(\mathbf{D_M^2}(\mathbf{Ax})(\mathbf{Ax})')}{1-\delta_{Res}} - \overline{\tau}} \\
&= \sqrt{\frac{r_0^2 \mathbf{Tr}(\mathbf{xx'A'D_M^2A}) - r_0 \mathbf{Tr}(\mathbf{xx'A'D_MA})}{1-\delta_{Res}}} \\
&\approx \sqrt{\frac{(r_0^2 \mathbf{x'D_M^2x} - r_0 \mathbf{x'D_Mx})\mathbf{Tr}(\mathbf{A'A})}{1-\delta_{Res}}} \\
&\approx \sqrt{\frac{\mathbf{Tr}(\mathbf{A'A})}{1-\delta_{Res}}} \sqrt{\sum_{j=1}^{K} r_0\omega_j(r_0\omega_j - 1)x_j^2}.
\end{aligned} \tag{5.8}$$

Referring to (5.7) and (5.8), the correlation between channel sparsity and mean delay can be explained intuitively as follows. According to the RIP in CS [100] and the desired reconstruction accuracy, the square sum of sparse coefficients is nearly a constant $\sum_{j=1}^{K} x_j^2 \approx 1 - \delta_{Res}$ for a given channel, no matter what the specified sparsity K is. The trace of a properly selected dictionary is also nearly a constant, i.e., trace$(\mathbf{A'A}) \approx M$, due to the low coherence requirement between different atoms. Thus, the mean delay in (5.7) is mainly determined by the weights ω_j. Generally, a dispersive channel generates more well-spaced multipath taps which result in more non-zero sparse coefficients. This is why complex NLOS or fast fading channels tend to show larger mean delay and larger sparsity compared to LOS or flat fading channels. The connection between RMS delay and sparsity can be explained in a similar way.

Table 5.2 presents the correlation between sparsity and the three TDL parameters, which is obtained by averaging over different datasets and algorithms. The correlation is defined as

$$r_{s,p} = \frac{N\sum s_i^{d,a} p_i - \sum s_i^{d,a} \sum p_i}{\sqrt{N\sum (s_i^{d,a})^2 - (\sum s_i^{d,a})^2}\sqrt{N\sum p_i - (\sum p_i)^2}}, \tag{5.9}$$

where i represents the i-th selected CIR profile, d and a are indexes of the dictionary and algorithms used for sparse analysis, respectively, $s_i^{d,a}$ represents the sparsity of the i-th CIR reconstructed by using the d-th dictionary and the a-th algorithm, and p_i is one of the studied channel statistics for the i-th CIR.

Table 5.2: Correlation between Sparsity and Propagation Parameters.

Cases	Types	MPC #	RMS τ_{RMS}	Mean Delay
Simulated	Rayleigh	0.90	0.95	0.93
	Rice (K=3)	0.80	0.89	0.91
	SV	0.49	0.53	0.71
Measured	Distance	0.43	0.62	0.56
	Body Parts	0.54	0.61	0.50
	Heights	0.43	0.57	0.50

The average correlation for simulated channels is about 0.8, while it is about 0.5 for the measured channels. The correlation coefficients between sparsity and the mean delay and RMS delay spread are greater than the one between sparsity and significant MPC numbers. This is because the MPC number is directly related to the sparsity, while the delay and RMS delay spread are related to the sparsity indirectly via the matrix $\boldsymbol{D}_M$.

It is worth noting that the first and second-order channel parameter characteristics in the temporal, frequency and spatial domains have similar mathematical forms. Thus, this relationship can be easily extended to other domains. Such connections between sparse parameters and traditional TDL-model-based first- and second-moment parameters can have valuable applications in sparse processing and performance evaluation areas. For example, using such correlations, RMS delay spread can be used to estimate channel sparsity roughly. On the other hand, the known sparsity can also be used to evaluate the singular value spread or the ergodic capacity of MIMO applications.

Therefore we can see that our proposed SCM model provides a compact and efficient representation for dense multipath channels, and most important parameters of a real channel can be derived from it. It not only provides direct connections to key statistical channel parameters such as mean delay and RMS delay spread, but also interprets cluster statistics such as cluster occurrence time, cluster shapes and energy via the parameters of index location ratio factor, shape factor and sparse channel coefficients.

5.5 Validation and Simulation

In this section, we use the obtained sparse channel models to generate simulated channels and compare them with the originally measured/simulated ones, in order to verify the effectiveness of the sparse channel models.

5.5.1 Generating Simulation Channels Using SCM Results

Using the statistics of sparsity, MDP and the atomic indexes in the developed sparse models, we can simulate channels with high accuracy particularly in the cluster structure with a limited number of parameters. Mathematically, the major steps for the proposed SCM model can be represented in the set of equations below,

$$\begin{cases} \widehat{\mathbf{y}_N} = \sqrt{P_0/P_L}\;\boldsymbol{\Psi}_{\widehat{\boldsymbol{\omega}}}\widehat{\mathbf{x}}, \\ \widehat{\boldsymbol{\omega}} = \{\widehat{\omega}_i\} = \{\widehat{\gamma}_i \times \iota_{\widehat{p}} + \iota_{\widehat{p}}^{\mathrm{Beg}}\}, \\ \widehat{\gamma} \sim \mathit{LogNorm}(\mu_\gamma, \sigma_\gamma), \\ \widehat{\mathbf{p}} \sim \mathit{Round}(\mathit{HalfNorm}(0, \sigma_p), \\ \widehat{\mathbf{x}} \sim \mathit{Norm}(\mu_{\widehat{x}}, \sigma_{\widehat{x}}), \end{cases} \tag{5.10}$$

In (5.10), P_0 is the transmission power and P_L is the predicted path loss (e.g., (1) in [49]); $\widehat{\mathbf{x}}$ is the sorted non-zero coefficient vector in descending order; $\widehat{\omega}_{\mathbf{i}}$, $\widehat{\mathbf{p}}$ and $\widehat{\gamma}$ are the randomly generated atomic index, shape and location ratio factors corresponding to (5.6); $\boldsymbol{\Psi}_{\widehat{\boldsymbol{\omega}}}$ means taking the atoms/columns with indexes $\widehat{\boldsymbol{\omega}}$ from $\boldsymbol{\Psi}$; $\mathit{Norm}(\cdot)$, $\mathit{LogNorm}(\cdot)$, and $\mathit{HalfNorm}(\cdot)$ represent Normal, Log-Normal, and half-Normal distributions, respectively; and $\mathit{Round}(\cdot)$ denotes the rounding operation.

Noted that sparse modeling is more suitable for small scale modeling, while large scale modeling is sufficient for simple regression. The large-scale selection is closely related to the environment, and the proposed sparse model is fully compatible with the large-scale changes of these different scenes.

So the process of channel generation mainly includes two steps: Firstly generating the sorted sparse coefficients $\widehat{\mathbf{x}}$ using Normal distributions and then generating corresponding sparse coefficient index set $\widehat{\omega}$. The atom shape factor set $\widehat{\gamma}$ and location ratio factor set $\widehat{\mathbf{p}}$ are individually generated by Log-Normal and half-Normal variables. For a given shape factor, the beginning index $\iota_{\widehat{p}}^{\mathrm{Beg}}$ and the total number $\iota_{\widehat{p}}$ of shape atoms $\widehat{\mathbf{p}}$ can be determined. Thus, the index set is generated and the CIR set is finally synthesized.

The basic method described in (5.10) can be simplified by using the prior information on, e.g., the exponential decaying rules of the sorted sparse coefficients. We present two examples next.

Firstly, assuming that $\widehat{\mathbf{x}}$ can be approximated by a negative exponential decaying function, the sorted coefficients $\widehat{\mathbf{x}}$ can be generated at a reduced complexity using the following function instead of the Gaussian function in (5.10)

$$\widehat{\mathbf{x}} = (a\,e^{-b\mathbf{k}} + c)(1 + \sigma_x), \tag{5.11}$$

where σ_x is the shadowing variable of the sorted non-zero sparse coefficients, and $\mathbf{k}$ is the sparse sequence set $\{1, 2, ...K\}$. By replacing the last equation in (5.10) with (5.11), an improved SCM predicted sparse coefficients (*SCM-PSC*) model is obtained. It is called “predicted” because these coefficients can be determined once the exponential function is selected.

Secondly, when modeling any new scenario with exponential decaying but unknown parameters a, b and c, we can estimate these parameters. To reduce the error between the estimates and the statistically optimal values for given channels, we propose a scheme called SCM Fitted Sparse Coefficients (*SCM-FSC*), which exploits both the sparse coefficient distribution and MDP attenuation for estimation. SCM-FSC only requires to use two sorted sparse coefficients. Without loss of generality, let them be the first and k-th sparse coefficients. The parameters for the exponential decaying can be obtained by solving the following ternary equation set

$$\begin{cases} x_1 = a\,e^{-b} + c, \\ x_k = a\,e^{-b\,k} + c \approx c, \\ \sum_{i=1}^{k} (a\,e^{-b\,k} + c) = 1 - \delta_{Res}. \end{cases} \tag{5.12}$$

The solution to (5.12) is shown in (5.13). Once the parameters are obtained, we can then generate all sorted coefficients for $\widehat{\mathbf{x}}$.

By exploiting the magnitude decaying rules, the *SCM-PSC* and *SCM-FSC* schemes reduce the coefficients to be statistically generated from K taps to only 1 or 2 taps. This can largely

$$\begin{cases} a = \frac{y_1 - y_k}{e^{-b}}, \\ b = -\ln \frac{y_k(y_1 - y_k) + \sqrt{y_k^2 (y_1 - y_k)^2 + (1 - \sigma_{Res} - k y_k)^2 (1 - \sigma_{Res} - y_1^2 - (k-1) y_k^2)}}{(1 - \sigma_{Res} - k y_k^2)^2}, \\ c = y_k, \end{cases} \tag{5.13}$$

Table 5.3: System Setup for Simulation

System models	SCM/ SCM-PSC/ SCM-FSC
Key parameter distributions	Sparse coefficients $\widehat{x}$: Gaussian Atom shape factor $\widehat{p}$: Half Gaussian Location ration factor $\widehat{\gamma}$: Log-Normal
MDP (a, b, c)	SCM-PSC : dependent on scenario SCM-FSC : dependent on sparse coefficients
Path loss model	$PL(d) = 48.6 + 10N(h) \times log_{10}(d) + BOF^{[17]}$ $N(h) = 1.33h^2 - 2.64h + 3.52$
CS dictionary	Symlet 4-5
CS algorithms	OMP/ ℓ1-Min/Iterative
Scenarios	Measured and simulated channels
Dataset size	432,000 (measured); 50,000 (simulated)

simplify channel simulation, particularly for high dimensional channels such as massive MIMO channels.

5.5.2 Sparse Channel Validation

In order to verify the effectiveness of the developed sparse channel models, we conduct Monte Carlo simulations for each dataset with the system setup shown in Table 5.3 . The height-dependent log-distance model is selected as the path loss model [49]. All three proposed SCM channel generation schemes are implemented. The widely used statistical TDL (STDL) model is also implemented for comparison [94, 95].

We developed and shared a channel simulator on Github for this work [1]. Fig. 5.15 depicts the Matlab based Graphic User Interface (GUI) with the corresponding modeling program can be accessed on Github. By setting up the parameters of sparse analysis and modeling modules, the statistics for sorted non-zero coefficients, and shape and location ratio factors are extracted. An example is shown in the left bottom table in Fig. 5.15. The generated CIRs corresponding to the selected scenario and extracted statistical parameters are shown in the module of modeling

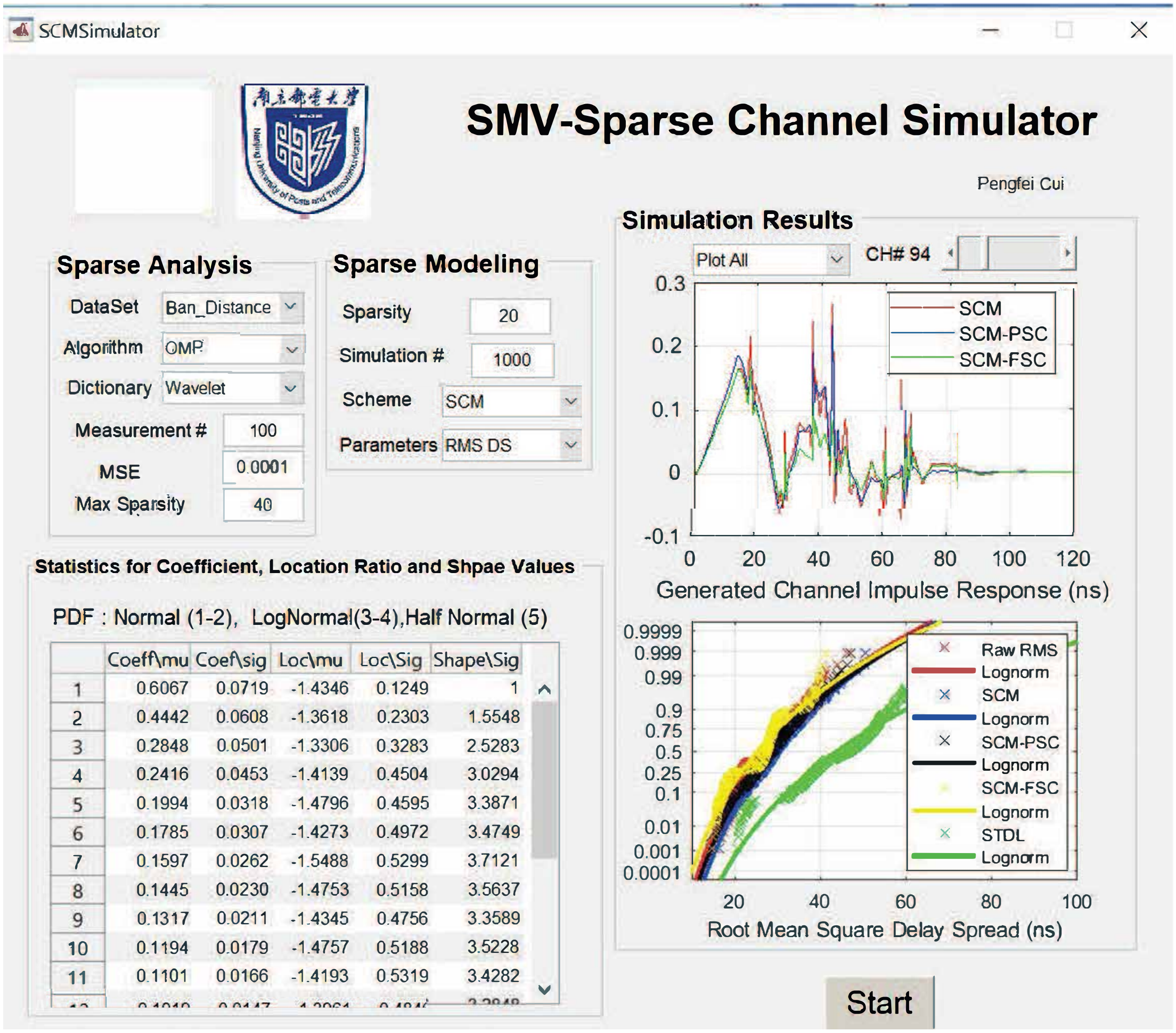

DataSet: Ban_Distance
Algorithm: OMP
Dictionary: Wavelet
Measurement #: 100
MSE: 0.0001
Max Sparsity: 40

Sparsity: 20
Simulation #: 1000
Scheme: SCM
Parameters: RMS DS

Statistics for Coefficient, Location Ratio and Shpae Values

PDF : Normal (1-2), LogNormal(3-4),Half Normal (5)

	Coeff\mu	Coef\sig	Loc\mu	Loc\Sig	Shape\Sig
1	0.6067	0.0719	-1.4346	0.1249	1
2	0.4442	0.0608	-1.3618	0.2303	1.5548
3	0.2848	0.0501	-1.3306	0.3283	2.5283
4	0.2416	0.0453	-1.4139	0.4504	3.0294
5	0.1994	0.0318	-1.4796	0.4595	3.3871
6	0.1785	0.0307	-1.4273	0.4972	3.4749
7	0.1597	0.0262	-1.5488	0.5299	3.7121
8	0.1445	0.0230	-1.4753	0.5158	3.5637
9	0.1317	0.0211	-1.4345	0.4756	3.3589
10	0.1194	0.0179	-1.4757	0.5188	3.5228
11	0.1101	0.0166	-1.4193	0.5319	3.4282

Figure 5.15: Graphic user interface for our developed single-measurement-vector sparse channel simulator that is available from Github [1].

results. By changing the plotting drop-down menu and channel number slider, one can configure the desired illustration results. The right upper figure in Fig. 5.15 shows an example. Three significant clusters which are widely observed in selected BAN_Distance dataset can be seen from generated CIR in 10, 40 and 70 nanoseconds. Such cluster-structures are hard to be simulated by traditional modeling methods with limited parameters.

The accuracy of the model is expressed by comparing the parameters of log-normal dis-

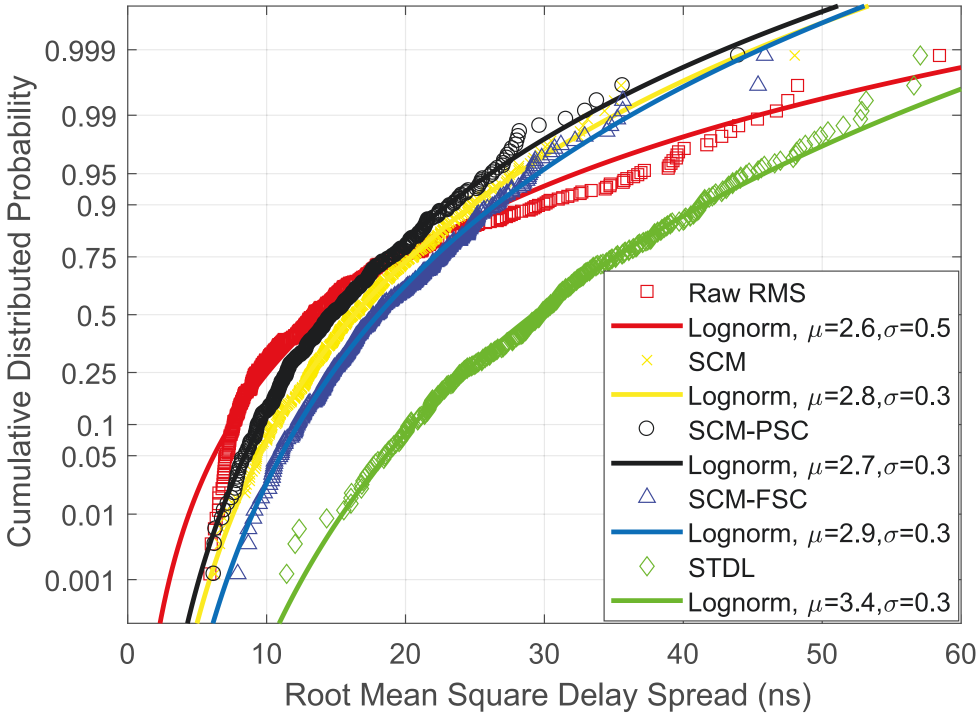

Figure 5.16: Model validation for the distributions of the generated root mean square delay spread of BAN_BONBO dataset.

tribution, and most of the parameter values are logarithmic expressions of signals. The main comparison object focuses on the amplitude, because the phase modeling is not always the focus of attention and is relatively easy to simulate, so it is not introduced much.

Three Key Performance Indicators (KPIs), including RMS delay spread, mean delay and signal levels, can be chosen on the sparse modeling panel. The right bottom figure in Fig. 5.15, which is also enlarged in Fig. 5.16, shows the CDF of the RMS delay spread for the generated CIRs using the standard SCM, SCM-PSC, SCM-FSC and STDL models, for the measured CIRs in BAN_Dis and BAN_Parts. The sparsity is about 20. All RMS delay spreads are best fitted by log-Normal distributions with parameters μ and σ. Referring to the measured RMS delay spread, three SCM schemes all achieve better accuracy than the STDL model. No significant difference is observed among three SCM schemes. This validates the effectiveness of replacing the sorted non-zero coefficients with their prediction or fitting values.

Table 5.4 summarizes the parameters of fitting Log-Normal distribution for Monte Carlo

Table 5.4: Extracted parameters for the fitting Log-Normal distribution for the CDF of root mean squared delay spread.

Cases	Dataset	Alg.	Real		SCM		SCM-PSC		SCM-FSC		STDL [95]	
			μ	σ	μ	σ	μ	σ	μ	σ	μ	σ
Meas.	Parts	OMP	3.17	0.38	3.22	0.26	3.13	0.30	3.14	0.27	3.59	0.30
		ℓ1-Min	3.17	0.38	3.21	0.26	3.18	0.27	3.14	0.28	3.72	0.23
	Dist.	OMP	3.29	0.22	3.39	0.19	3.35	0.21	3.36	0.19	3.79	0.24
		ℓ1-Min	3.29	0.22	3.38	0.20	3.39	0.20	3.26	0.24	3.79	0.17
	Height	OMP	3.32	0.51	3.42	0.35	3.34	0.44	3.38	0.39	3.87	0.20
		ℓ1-Min	3.32	0.51	3.42	0.37	3.37	0.40	3.18	0.59	3.84	0.20
Simul.	SV [97]	OMP	2.23	0.16	2.66	0.35	2.64	0.38	2.38	0.38	2.97	0.28
		ℓ1-Min	2.99	0.20	2.51	0.41	2.57	0.42	2.72	0.42	3.17	0.29
	Rayl. [96]	OMP	2.17	0.47	2.45	0.45	2.42	0.51	2.06	0.39	2.79	0.34
		ℓ1-Min	2.24	0.36	2.35	0.52	2.46	0.51	2.23	0.53	2.98	0.37

experiments for three measured and two simulated channel datasets, using the SMV-Sparse channel simulator tool. All the three SCM schemes are found to perform better than the STDL model. It is interesting to see that the SCM-PSC and SCM-FSC models perform better than the basic SCM scheme. This reflects the high accuracy of the exponential decaying function in modeling the MDP. SCM-FSC performs best in simulated cases, which indicates the effectiveness of exploiting both sparse channel statistics and MDP information. Generally, SCM with the ℓ1-Min algorithm performs better than that with OMP. These results indicate that the proposed SCM schemes work well for different channels, dictionaries, and recovery algorithms.

We can also see that for SCM there exists a small gap for the values of the channel parameters μ and σ between the actual and model-generated channels. For example, for μ, the gaps are in average 5%. This is much smaller than the 15% gap for STDL. Such a small gap is likely caused by severe fading and using aggregated data from different body positions in SCM. It is generally acceptable and has an insignificant impact on both system simulation and design. This gap is also expected to be reduced for channels with smaller bandwidth and less body shadowing. We also note that channel modeling is a problem of signal synthesis, where the requirement for accuracy is not as high as that in signal recovery. Pursuing very high modeling accuracy could require too many fitting parameters and lead to the over-fitting problem.

5.6 Conclusion

In this chapter, we highlighted the trade-off between sparsity, modeling accuracy and reconstruction complexity in SCM, and introduced a universal three-stage methodology for SCM. We also developed comprehensive statistical sparse channel models, using both measured and simulated channel datasets representing ultra-wideband channels over the frequency band from 6 to 8.5 GHz. For both datasets, channels generated from the developed statistical models match original ones in many aspects, which demonstrates the robustness of the methodology and the developed models. A summary of important SCM results for the channel datasets in this chapter are as follows:

- The sparsity generally conforms to the Normal distribution and can be significantly affected by the channel fading types and LOS conditions;
- Average sparsity is found to be approximately 20 under a modeling accuracy of MSE=10^{-4};
- The sorted non-zero sparse coefficients, the corresponding location ratio factors and shape values follow Normal, Log-Normal and half-Normal distributions, respectively;
- The magnitudes of sorted non-zero sparse coefficients (i.e., the MDP) follow exponentially decaying rule and the decaying speed is mainly affected by channel conditions.

Our proposed models and channel simulation methods have been implemented in Matlab and shared on Github, which allows open access for promising applications in dense channel modeling, sparse channel estimation and system design.

Chapter 6

MMV Off-body Sparse Analysis and Channel Modeling

6.1 Introduction

With the emerging of 5th generation mobile communication (5G), the signal bandwidth, antenna array scale, and number of access nodes are becoming increasingly large. The estimation and modeling for the channels (in particular channel impulse responses (CIR)) in this case confronts great challenges due to the conflicts between larger signal dimension and limited computation/energy resources. Nevertheless, such channels are proved to exhibit a sparse structure and can be modeled using Compressive Sensing (CS) technologies with a limited number of significant parameters [63].

CS technologies can compress signals with inherent sparsity and then recover them using a few measurements. They have received increasing interest in the application of sparse channel estimation [64, 77, 79]. However, existing research generally assumes sparsity that is inherent in channels, and only focuses on how to estimate and reconstruct the channels. There is very limited work on assessing and modeling the corresponding channel coefficients in sparse channel models. For example, Rayleigh fading is widely used in characterizing and modeling the CIR of wireless channels. But there exists no good characterization for the statistical distribution of sparse channel coefficients.

In this chapter, using measured channel data for body area networks, we study sparse channel modeling using compressive sensing techniques. We first propose an algorithm for extracting sparse channel coefficients from real channel measurement data in body area networks [49,173], then study the statistical property/distribution of the channel coefficients, and finally propose an algorithm for generating simulation channels using the developed sparse channel models. We use multi-measurement vector (MMV) CS scheme to jointly process channels measured under similar scenarios. In this way, we hope to improve the robustness and accuracy of channel modeling by suppressing measurement noise and interference.

The rest of this chapter is organized as follows. In Section 6.2 we propose a sparse channel coefficient extraction algorithm based on MMV CS techniques. In Section 6.3, we develop statistical models for the sparse coefficients, and propose an algorithm for generating simulation channels based on the statistical model. In Section 6.4, we compare the generated channels with the actual ones and verify the effectiveness of the proposed sparse channel models. Finally, Section 6.5 concludes the paper.

6.2 Channel Coefficient Extraction Using MMV CS Algorithms

In this section, we discuss how to apply MMV CS algorithms to extract channel coefficients based on sparsity assumption, including several preprocessing steps to improve the extraction performance.

6.2.1 Channel Measurement Dataset

The channel data is measured in a typical hospital-type room with a few furnitures. An omni-directional monopole antenna is used to emulate the external access point (AP), and a wearable

---

This work is supported by National Nature Science Foundation Council (NSFC) Proposal under granted no. 61427801 and 61471204.

loop-dipole combined antenna worn on different positions of the volunteer is used to emulate the receiver (Rx). A vector network analyzer (cf. VNA Agilent 8720) is used to generate a 0 dBm, 801-point sweeping signal with the frequency ranging from 6 to 8.5 GHz. The off-body CIRs are observed in different body-worn parts and large-scale measurement locations. For detailed description of the channel dataset, the readers are referred to [49, 173].

6.2.2 Multi-channel Coefficient Extraction

As mentioned in Section 6.1, we combine multiple measurements under one scenario and apply MMV CS techniques to jointly extract the significant channel coefficients [179]. There are mainly two benefits compared to doing extraction based on a single measurement:

- There is naturally correlation between different measurements obtained under one scenario, for example, arrival time, number of clusters, and power profile. Hence jointly processing multiple measurements can potentially lead to more stable statistical results.
- Joint processing can also lead to improved coefficient estimation in the presence of measurement noise and interference, thanks to the advantage of MMV CS algorithms.

Hereafter, we will refer to such multiple CIR measurements under a common scenario as multi-channel CIRs.

For measured multi-channel CIRs $\mathbf{Y} \in \mathbb{R}^{M\times Q}$, we can formulate the channel coefficient extraction problem as a MMV CS problem

$$\min_{\mathbf{X}} \|vec(\mathbf{\Psi X})\|_1 \text{ subject to } \mathbf{Y} = \mathbf{\Phi\Psi X} + \mathbf{R} \tag{6.1}$$

where $\mathbf{\Phi} \in \mathbb{R}^{M\times N}$ $(M \leq N)$ is the measurement matrix/dictionary, $\mathbf{\Psi} \in \mathbb{R}^{N\times N}$ is the dictionary/transformation matrix, $\mathbf{X} \in \mathbb{R}^{N\times Q}$ is the sparse matrix to be estimated, $\mathbf{R}$ is the residual matrix representing noise and/or residual errors in the sparsity approximation, $vec(\cdot)$ is an operator that converts a matrix to a vector. We assume that $\mathbf{R}$ follows Gaussian distribution $N(0, I_Q)$, and $\mathbf{\Psi}$ is an identity matrix.

Algorithm 1 TA-SOMP Algorithm for Extracting Channel Coefficients in Sparse Channel Model.

```
Preparation: 1) De-noising CIRs with wavelet soft threshold 2) normalize power of each CIR to 1, record power vector $\mathbf{p}$; 3) Time alignment $\mathbf{Y} \rightarrow \widetilde{\mathbf{Y}}$, and record time-shift vector $\mathbf{t^s}$; 4) Select the best dictionary $\mathbf{\Phi}$;
Initialization: residual matrix $\mathbf{R}_0 = \widetilde{\mathbf{Y}}$, index set $\Lambda_0 = \emptyset$, iteration t=1;
repeat
    Best atom: find index $\lambda_t = arg\max_i \|\widetilde{\mathbf{Y}}^T \phi_i\|$
    Update index: $\mathbf{\Lambda}_t = \mathbf{\Lambda}_{t-1} \bigcup \{\lambda_t\}$
    Update residual: $\mathbf{R}_t = \widetilde{\mathbf{Y}} - \mathbf{\Phi}_{\Lambda_t} \mathbf{\Phi}^{\dagger}_{\Lambda_t} \widetilde{\mathbf{Y}}$
    $t = t + 1$;
until Stopping criterion: $t = t_{max}$ or $\frac{\|\mathbf{R}_t\|_F}{\|\widetilde{\mathbf{Y}}\|_F} \leq \eta$
return $\mathbf{X} \leftarrow \mathbf{\Phi}^{\dagger}_{\Lambda_t} \widetilde{\mathbf{Y}}, \mathbf{p}, \mathbf{t^s}$
```

6.2.3 Proposed Time-Aligned SOMP algorithm

Many MMV CS algorithms can be used to solve (6.1), such as cosparse analysis algorithms [180], simultaneous orthogonal matching pursuit (SOMP) [181] and MMV Bayesian compressive sensing. Considering the implementation complexity and generality in greedy algorithms, SOMP is selected for our work here.

Before applying SOMP to the measurement data $\mathbf{Y}$, we need to do some preprocessing for the data, which includes de-noising, time alignment and selection of the dictionary. For de-noising, we compared several methods and selected the best Wavelet soft threshold method. For time alignment, the main purpose is to remove timing difference between transmitter and receiver over different measurements. Dictionary affects the sparsity and reconstruction accuracy. These preprocessing will be detailed later.

The proposed time-aligned SOMP (TA-SOMP) is summarized in Algorithm 1. Note that depending on the used dictionary, the extracted channel coefficients do not necessary represent the CIR any more.

De-noising

It is important to de-noise and improve the smoothness of the measured CIRs. We compared three de-noising methods, wavelet de-noising with soft threshold [182], Kaiser-15-order window-

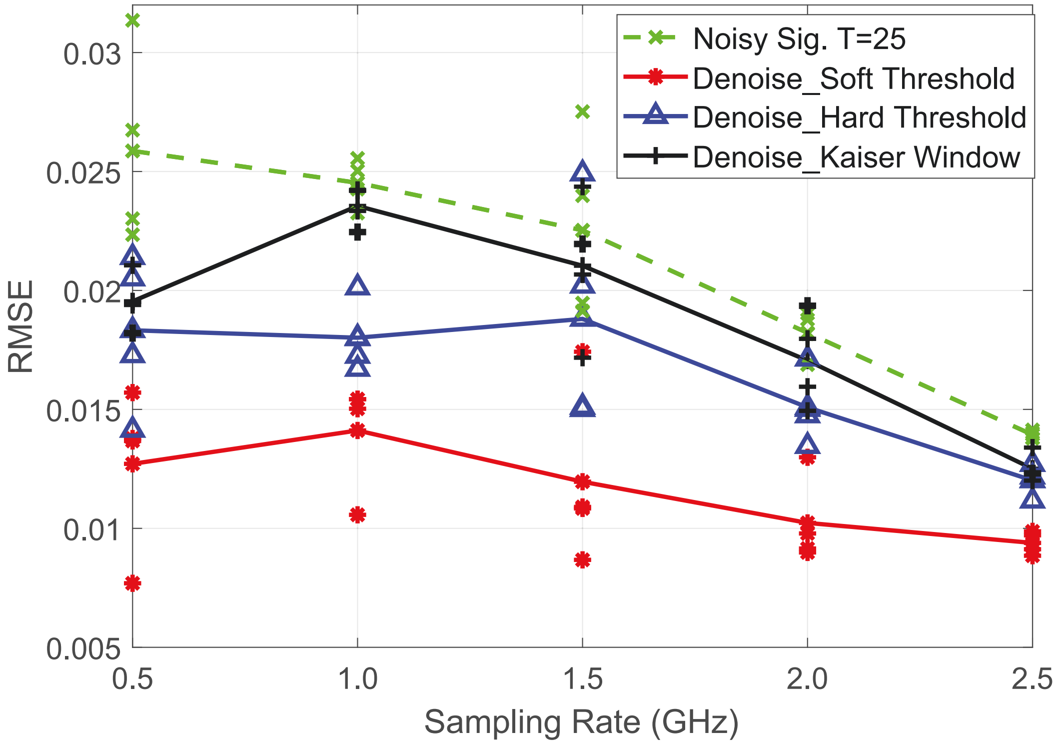

Figure 6.1: Comparison of recovery accuracy for different de-noising methods. Marks are for individual results, and solid curves denote the mean values (Notice the discrete points, which represent the true value of the corresponding curve and are omitted from the diagram).

ing filter and de-noise with a hard threshold. The de-noising results, together with the results without de-noising, are presented in Fig. 6.1, when the TA-SOMP algorithm is applied. The recovery accuracy is evaluated using the metric of rooted mean square error (RMSE) between the original and reconstructed CIRs. All three de-noising methods perform better than the case without de-noising operation. The wavelet soft threshold method performs the best, and the Kaiser-15-order filter is the least.

This figure shows that the RMSE gap between de-noising and without de-noising decreases as the sampling ratio increases. It is interesting to note that the accuracy improvement by de-noising remains nearly the same as sampling ratio increases in terms of the Frobenius norm error. The relationship between these two metrics is worthy of some further investigation, as will be presented in Section 6.2.4.

Time Alignment

For time alignment, we first randomly select a measured CIR in each group as a referene CIR, then compute the correlation between this reference CIR and any other CIR, and cyclically shift the other CIR to the timing point corresponding to the maximum correlation. As a result, the significant clusters of multi-channel CIRs can be aligned in time domain. This can generally remove variations caused by transceiver timing and small environmental changes during measurement. Record the timing shift vector $\mathbf{t}^{\mathbf{s}}$ which will be taken into consideration in subsequent channel modeling.

Fig. 6.2 compares recovery accuracy by Algorithm 1 between cases with and without time alignment. The data is from real multi-channel CIRs measured from 12 different heights of the same small-scale grid as detailed in [49, 173]. It can be seen that in nearly all cases time alignment performs better than those without time alignment. The RMSE also decreases with the iteration number increasing.

Dictionary Selection

Research for the selection of the dictionary (the measurement matrix too in this chapter) mainly focuses on 1) the properties of the measurement matrix such as spark and restricted isometry property and 2) some selection principles such as similarity and weak relevance [79, 181]. For CIR construction and modeling, we need a quantitative and easy-to-execute metric which also takes the features of observed CIRs into consideration. In this chapter, we adopt the *similarity index* which links dictionary selection to the clusters of target CIR and is defined as

$$S_{Ind} = \sum_{l=1}^{N} \frac{\|\mathbf{y}_l^{Cluster}\|_F}{\| \mathbf{y}\|_F} \max_{i\in\Omega} \phi_i^T \mathbf{y}_l^{Cluster} \tag{6.2}$$

where $\mathbf{y}_l^{Cluster}$ is the l-th cluster of the original CIR $\mathbf{y}$, ϕ_i^T is the i-th atom of the dictionary $\mathbf{\Phi}$, and Ω is the corresponding index set.

In Fig. 6.3, we present the comparison results using the metric similarity indexes for 11 commonly used dictionaries including five different wavelets (Haar, Biorthogonal, Daubechies,

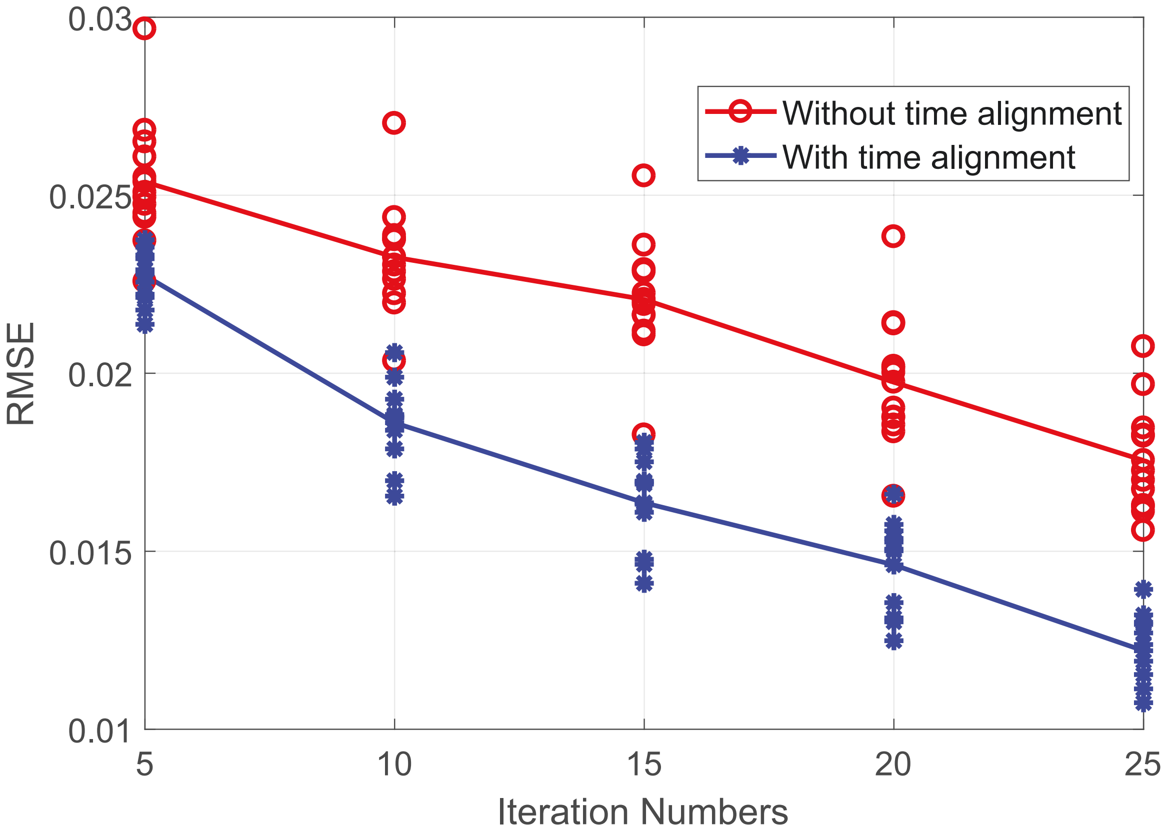

Figure 6.2: Comparison of recovery accuracy between cases with and without time alignment. Again, solid curves are for the mean of the results (Notice the discrete points, which represent the true value of the corresponding curve and are omitted from the diagram).

Coiflet, and Symlet), two random matrices (Gaussian and Bernoulli) and four others (DCT, polynomial, sin and Fourier matrices). Results show that the wavelet dictionaries have the highest similarity indexes of 0.6-0.7, followed by the two random matrices with similarity indexes of 0.4-0.45. Thus, we select the highest performing symlet dictionary for the work here. čż

6.2.4 Error metrics: Frobenius norm error versus RMSE

RMSE is a widely used metric in curve fitting and distribution analysis while Frobenius norm error is commonly used to characterize estimate accuracy. For our problem, the link between

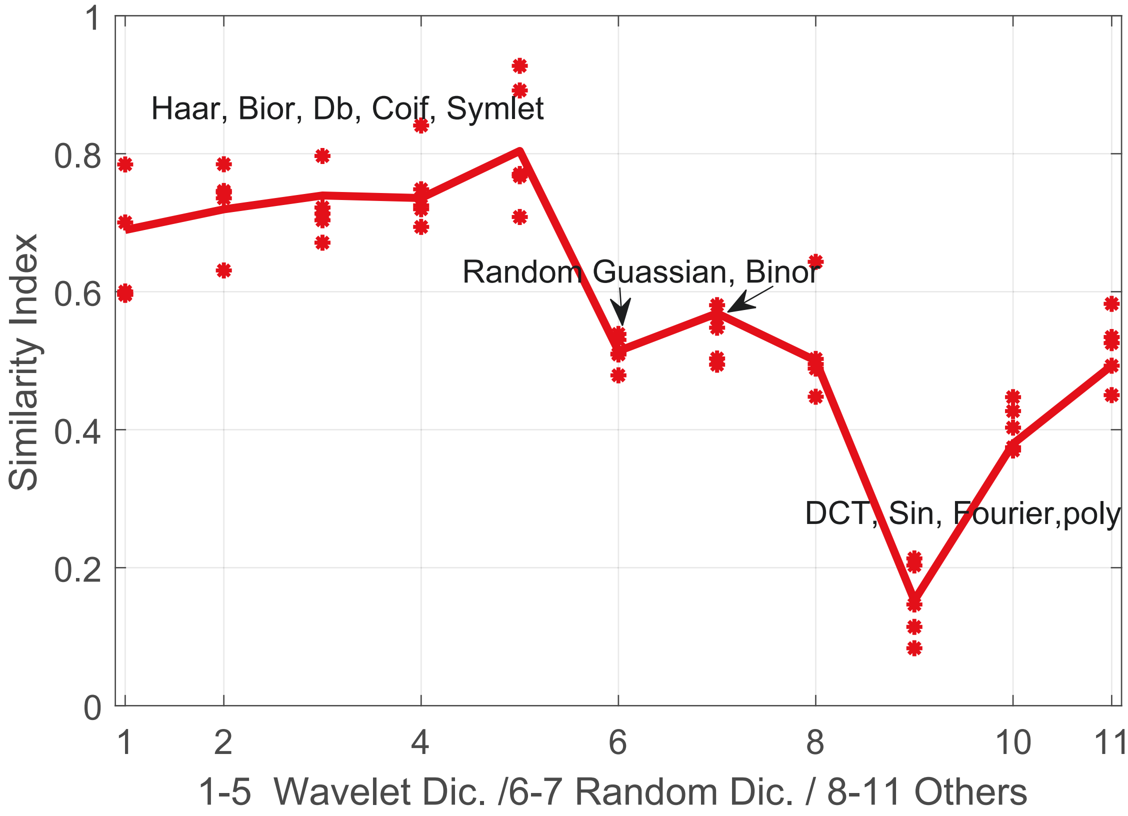

Figure 6.3: Comparison of similarity indexes for 11 commonly used dictionaries.

RMSE and Frob-norm can be established as

$$\begin{aligned} RMSE &= \tfrac{1}{Q}\textstyle\sum_j \sqrt{\tfrac{\sum_i r_{i,j}^2}{M}} \\ &\leqslant \tfrac{1}{Q}\sqrt{Q\tfrac{\sum_j \sum_i r_{i,j}^2}{M}} \\ &= \sqrt{\tfrac{\sum_j \sum_i r_{i,j}^2}{QM}} = \tfrac{\|\mathbf{R}\|_F}{\sqrt{QM}}. \end{aligned} \tag{6.3}$$

In the above, the inequality follows the Cauchy inequality, and $\|\cdot\|_F$ represents Frobenius norm. Since $|r_{i,j}|$ is generally smaller than $|a_{i,j}|$ and $\|\mathbf{Y}\|_F = \sqrt{Q}$ in this chapter, the upper bound for RMSE is given by $\frac{1}{\sqrt{M}}$ rather than 1. The relationship between Frobenius norm error $\mathbf{E}_{Frob}$ and the normalized RMSE (NRMSE) can then be expressed as

$$\begin{aligned} NRMSE &\doteq RMSE/\tfrac{\|\mathbf{Y}\|_F}{\sqrt{QM}} \\ &\leqslant \tfrac{\|\mathbf{R}\|_F}{\|\mathbf{Y}\|_F} = \mathbf{E}_{Frob}. \end{aligned} \tag{6.4}$$

Equation (6.4) indicates that the RMSE is generally smaller than the Frobenious norm error.

Note that the equality $NRMSE = \mathbf{E}_{Frob}$ holds when $\sum_i r_{i,j}^2$ is constant for different i and j. This implies that the square sum of any single CIR's residuals of the same multi-channel CIRs should remain the same. Since the power of each channel is normalized and the residuals for simultaneous channels follow the same zero-mean normal distribution, such condition can be met with a high probability. This is why the gap between Frobenious norm error and NRMSE is often less than 5% which can be negelected in practial applications.

6.3 Modeling for Sparse Channels

In this section, we study the statistical properties of the extracted channel coefficients by the TA-SOMP algorithm, and develop an algorithm for generating simulation channels using the derived statistical sparse channel models.

When running Algorithm 1, the results are obtained with the max iteration $t_{max} = 25$, simultaneous channel number $Q = 80$ and the Frob-norm error threshold $\eta = 10\%$.

6.3.1 Statistical Properties of Channel Coefficients and Wavelet levels

In Fig. 6.4, we present the statistical properties of the sparse channel coefficients for both cases with and without time alignment obtained from TA-SOMP. The best fitted distribution for coefficient bias of any multi-channel CIRs with time alignment is simplified from t-scale-location (fitted distribution cases without time alignment) to simple zero-mean normal distribution. Meanwhile, each specific tap bias also follows zero-mean normal distribution with their standard variations slightly fluctuate around the overall parameters. Fig. 6.4 shows that the minimum, overall and maximum standard variation are 0.03, 0.06 and 0.09, respectively. Note that the power variation among a large-scale area is dominated by the path loss formula as shown in [49, 183].

Similar normal distributions are observed for the sorted taps of different multi-channel CIR groups. For example, the maximum tap of averaged coefficients for various CIR groups measured from 5 different antenna body-worn parts follows the normal distribution $N(\mu = 0.02, \sigma = 0.05)$.

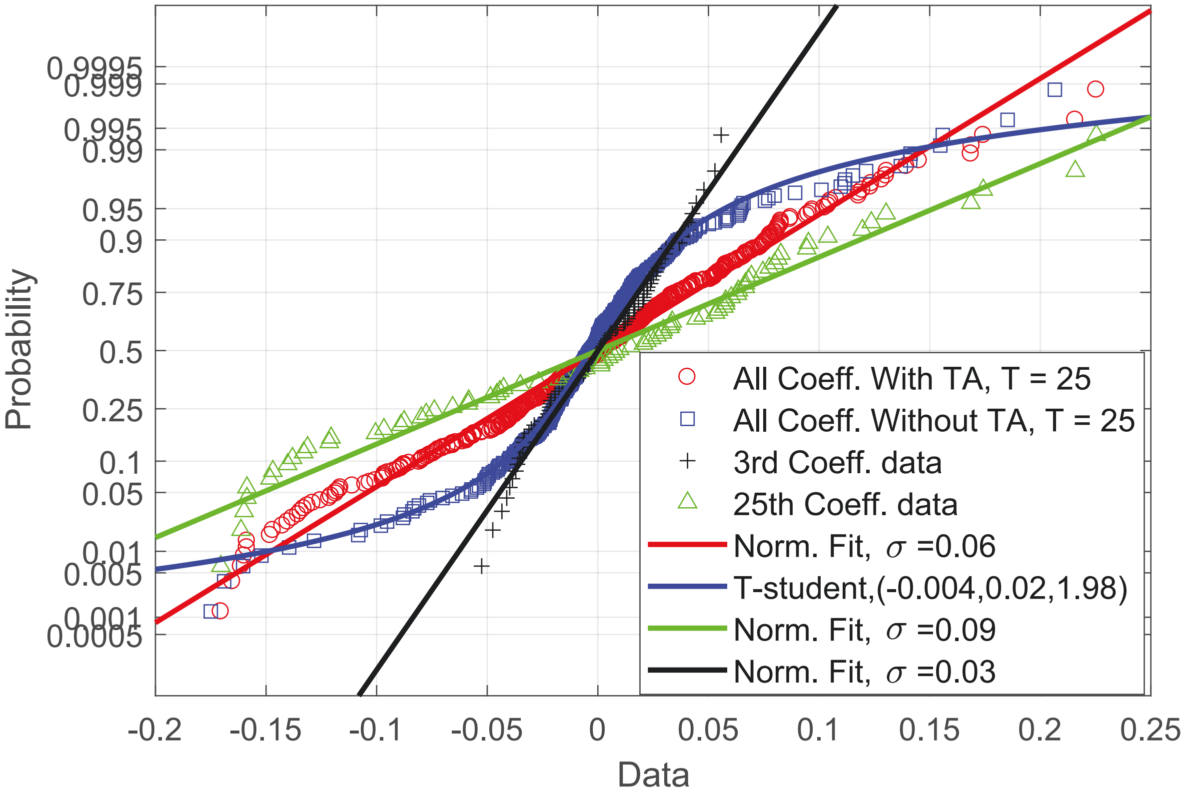

Figure 6.4: Distributions of coefficient bias values in cases with and without time alignment

Due to the multi-scale features of wavelet dictionary, the channel coefficient extraction accuracy can be further improved by separating the scale and location parameters which are given by

$$\begin{cases} \widehat{\Lambda} = S^{begin}_{L_{num}} + S^{length}_{L_{num}} \times Va, \\ \widehat{ln(Va)} \sim norm(\mu(ln(\Lambda_{Va})), \sigma(ln(\Lambda_{Va}))), \\ L_{num} \sim round(norm(\mu(\Lambda_{L_{num}}), \sigma(\Lambda_{L_{num}}))), \end{cases} \tag{6.5}$$

where $\mu(\cdot)$ and $\sigma(\cdot)$ represent the mean and standard variation obtained by the maximum likelihood estimation (MLE) method, $round(\cdot)$ and $ln(\cdot)$ represent the rounding and natural logarithm operations, respectively, $S^{begin}_{L_{num}}$ and $S^{length}_{L_{num}}$ represent the starting index number and the length of L_{num} scale in a specific wavelet dictionary, respectively. The parameters L_{num} and $Va \in (0, 1)$ represent the scale number of a specific dictionary index and its corresponding location value calculated by $Va = (\lambda - S^{begin}_{L_{num}})/S^{length}_{L_{num}}$.

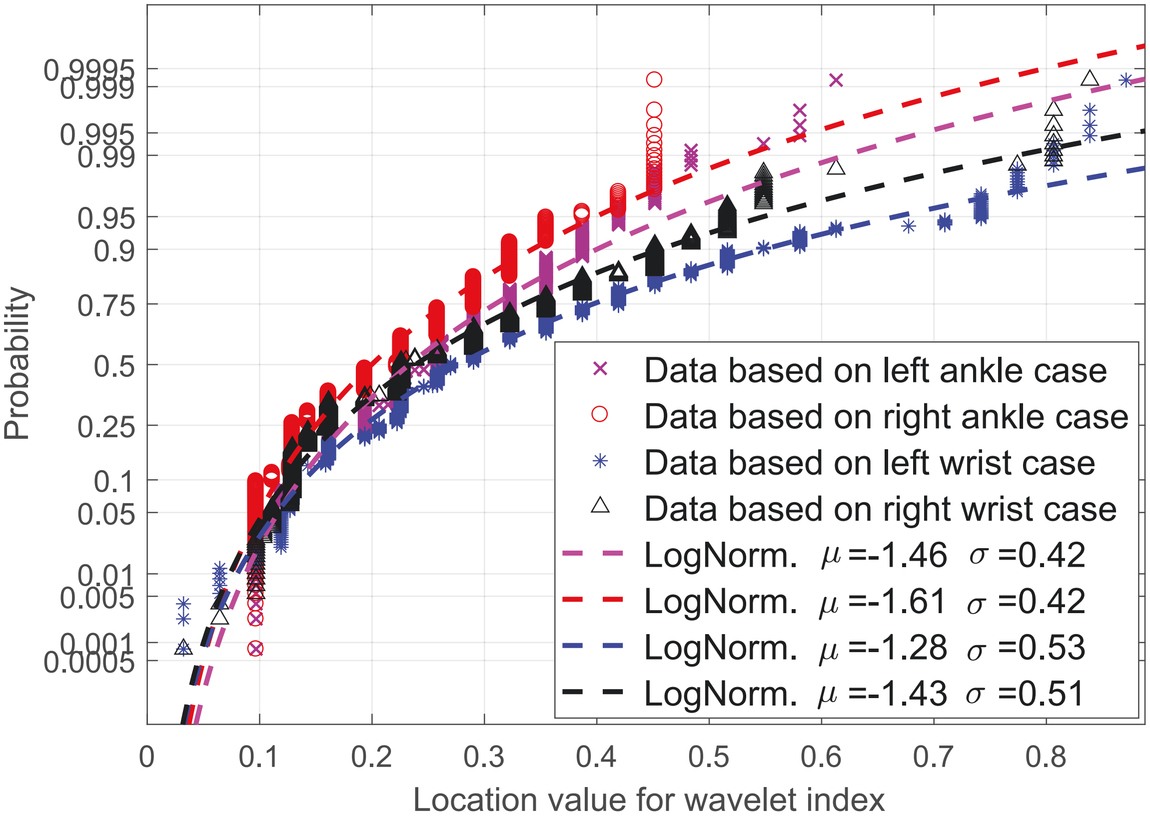

Figure 6.5: Distributions of location values for wavelet dictionary index

In Fig. 6.5, we present the distributions of location values for multi-scale dictionary index based on 4 data set. They all fit log-normal distributions very well. The extracted sparse channel coefficients from similar body parts follow nearly the same distributions. More details about the location values will be introduced in Section 6.3.2.

6.3.2 Algorithm 2: Channel Modeling and Generation

Based on the obtained statistical models, we can generate simulation channels. Combining the TA-SOMP algorithm, we now propose a complete multi-channel CIR generation algorithm - CS random variables combinational model - for establishing statistical sparse channel models and generating simulation channels from the models. Mathematically, the major steps can be represented in the equations below:

$$\begin{cases} \widehat{\mathbf{y}} = \widehat{\mathbf{y}}^{base} + \widehat{\mathbf{y}}^{bias}, \\ \widehat{\mathbf{y}}^{base} = \sqrt{P_0/PL}\ \mathbf{\Phi}_{\widehat{\mathbf{\Lambda}}}\widehat{\mathbf{x}}^{ref}, \\ \widehat{\mathbf{y}}^{bias} = \sqrt{P_0/PL}\ \mathbf{\Phi}_{\widehat{\mathbf{\Lambda}}}\widehat{\mathbf{x}}^{bias}, \\ \widehat{\mathbf{x}}^{ref} = \frac{\widehat{\mathbf{x}}}{\|\mathbf{x}\|_F}\sqrt{1-\boldsymbol{E}_{Frob}}, \\ \widehat{\mathbf{x}} \sim norm(\mu(\overline{\mathbf{X}}_{t_m}), \sigma(\overline{\mathbf{X}}_{t_m})), \\ \widehat{\mathbf{ln}(\mathbf{\Lambda})} \sim round(norm(\mu(ln(\Lambda)), \sigma(ln(\Lambda)))), \\ \widehat{\mathbf{x}}^{bias} \sim norm(\mathbf{0}, \sigma(\mathbf{X}_{t_m}^{bias})), \end{cases} \tag{6.6}$$

where P_0 is the transmitting power and PL is the path loss. Note that the base signal $\mathbf{y}^{base}$ represents the common sparse structure in specific large-scale position and is only produced once. The $t_{max} \times 1$ random variable vector $\widehat{\mathbf{x}}^{bias}$ follows zero-mean independent identically normal distribution and needs to be repeatedly generated. Thus,varying CIRs can be simply generated based on zero-mean normal random variables. This makes the proposed model superior to existing CIR generation models.

The algorithm is summarized in Algorithm 2. There are mainly 2 stages in Algorithm 2. The first stage includes the loop steps (S1 to S4) and S5, and can be called as *parameter extraction* stage. The rest can be called as *CIR generation stage*. In stage 1, the common sparse structure which exists in a group of MMV CIRs is represented by the average coefficient vector $\overline{\mathbf{X}}_i$. Then, the common sparse structure sets are statistically analyzed with the MLE method. Since the values and atom indexes of sorted cosparse coefficients in different small-scale measurement locations all follow normal distribution (with different parameters), such statistics can be readily used to generate the MMV reference coefficients and the corresponding atom indexes. Then, a base signal can be generated. Moreover, new coefficients can be easily generated by adding small-scale coefficient bias variables. a M-point CIR can then be generated by using only t_{max} zero-mean random variables.

Algorithm 2 CIR generation algorithm: CS random variables combinational model

```
Input: $\mathbf{t}_{max}, \{\mathbf{Y}_i | i \in [1...G]\}$
Initialize: $\overline{\mathbf{X}}_{\mathbf{t_m}} = \emptyset$, $\overline{\mathbf{X}}_{t_m}^{bias} = \emptyset$, $\Lambda = \emptyset$
repeat
    S1: Run TA-SOMP and get coefficients, power and time shift vectors $(\mathbf{X}_i, \mathbf{p_i}, \mathbf{t_i^s})$ =TA-SOMP$(\mathbf{Y}_i, t_{max})$
    S2: Average $\mathbf{X}_i$ over each coefficient to obtain reference coefficient vector $\overline{\mathbf{X}}_i$
    S3: Sort $\mathbf{X}_i$ and obtain $\mathbf{t}_{max}$ maximum values $\overline{\mathbf{X}}_{t_m,i}$ and the corresponding index set $\Lambda_i$. The remaining is the bias matrix $\mathbf{X}_{t_m,i}^{bias}$
    S4: Let $i = i + 1$, and combine coefficients bias matrix, mean and index vectors in rows $\overline{\mathbf{X}}_{\mathbf{t_m}} = \overline{\mathbf{X}}_{\mathbf{t_m}} \cup \overline{\mathbf{X}}_{t_m,i}, \overline{\mathbf{X}}_{\Lambda}^{bias} = \mathbf{X}_{t_m}^{bias} \cup \mathbf{X}_{t_m,i}^{bias}, \Lambda = \Lambda \cup \Lambda_i$
until $i \le G$
S5: Use MLE to estimate the normal distribution parameters for each row (coefficient) of $\overline{\mathbf{X}}_{t_m}, \overline{\mathbf{X}}_{t_m}^{bias}, \Lambda$, and obtain the mean and standard variations $\mu(\overline{\mathbf{X}}_{t_m}), \mu(ln(\Lambda)), \sigma(\overline{\mathbf{X}}_{t_m}), \sigma(\mathbf{X}_{t_m}^{bias}), \sigma(ln(\Lambda))$
S6: Randomly generate $t_{max}$ reference coefficients from $norm(\mu(\overline{\mathbf{X}}_{t_m}), \sigma(\overline{\mathbf{X}}_{t_m}))$, $t_{max}$ integer indexes from $Round(norm(\mu(ln(\Lambda)), \sigma(ln(\Lambda))))$, and $t_{max}$ rows of bias signals from $norm(\mathbf{0}, \sigma(\mathbf{X}_{t_m}^{bias}))$
S7: Obtain generated coefficients $\widehat{X}$ by adding bias matrix to the reference one, then adjust the coefficient with constraints $\|\theta\|_2 = \sqrt{1 - \boldsymbol{E}_{Frob}}$
return generated CIRs $\widehat{\mathbf{Y}} = \mathbf{\Phi}\widehat{X}$
```

6.3.3 Residual errors and coefficient constraint

The constraint $\|\theta\|_2 = \sqrt{1 - \boldsymbol{E}_{Frob}}$ in Algorithm 2 is critical for shaping the power delay profile of the generated CIRs. This constraints can be derived as follows.

As any recovered CIR $\widehat{\mathbf{y}} = \mathbf{\Phi_\Lambda}\theta_{\mathbf{\Lambda}}$ by matching pursuit algorithm is orthogonal to the residual $\mathbf{r}$, we have

$$\begin{aligned} \|\mathbf{y}\|_2^2 &= \| \ \mathbf{\Phi}_\Lambda \theta_\Lambda + \mathbf{r} \ \|_2^2 \\ &= \|\mathbf{\Phi}_\Lambda \theta_\Lambda\|_2^2 + \|\mathbf{r}\|_2^2 \\ &\le \|\mathbf{\Phi}_\Lambda\|_2^2 \|\theta_\Lambda\|_2^2 + \|\mathbf{r}\|_2^2, \end{aligned} \tag{6.7}$$

where the second inequality can be derived by using $\|\mathbf{\Phi}\|_{2,2} = sup\frac{\|\mathbf{\Phi}\theta\|_2}{\|\theta\|_2}$. Due to the weak coherence among atoms, $\|\mathbf{\Phi}_\Lambda\|_2$ is close to 1 and the two sides of inequality are actually very close to each other. Thus, it can be derived that $\|\theta\|_2 \simeq \sqrt{\|\mathbf{y}\|_2^2 - \|\mathbf{r}\|_2^2}$. Replacing $\|\mathbf{y}\|_2$ with 1, the constraint $\|\theta\|_2 = \sqrt{1 - \boldsymbol{E}_{Frob}}$ is obtained.

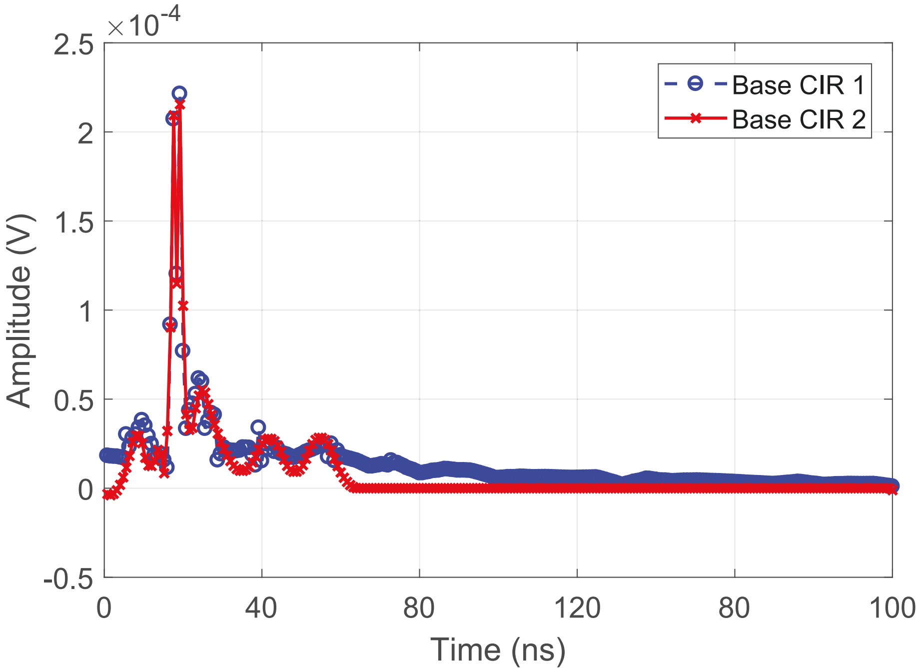

(a) Base CIR for Generation

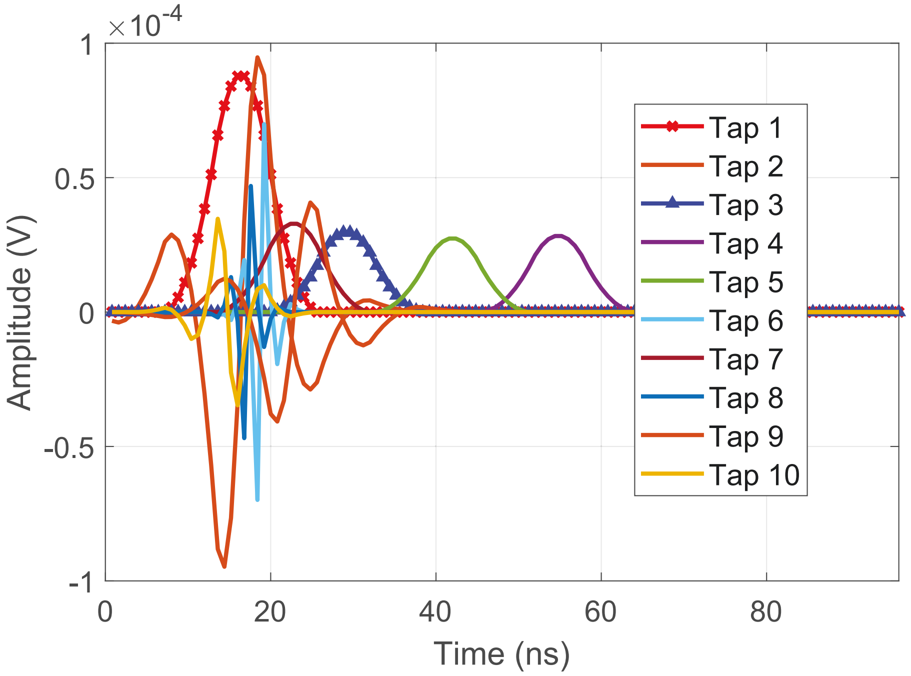

(b) Components for base CIR

Figure 6.6: Illusion of generated base CIR and their components.

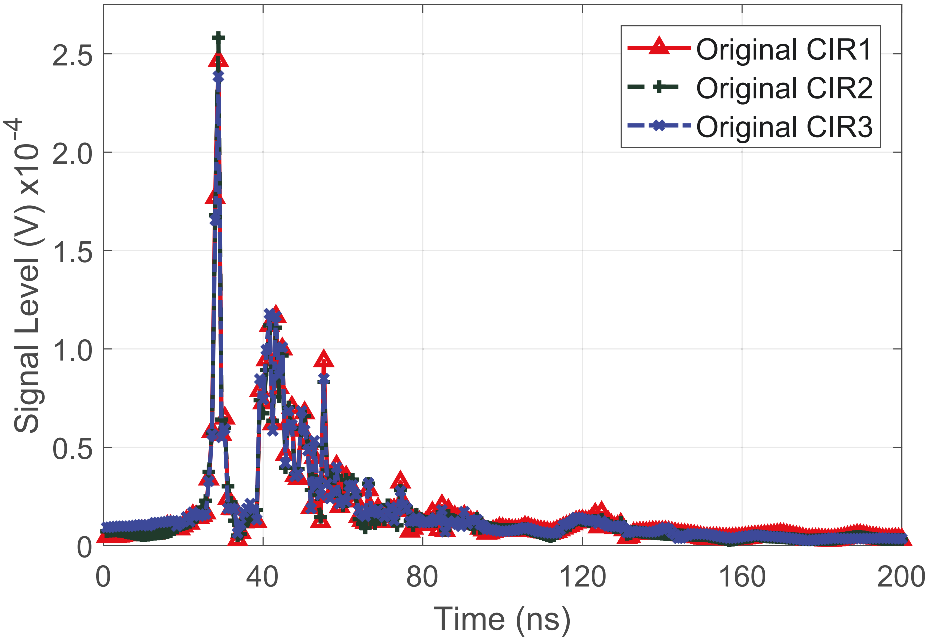

(a) Measured CIRs in off-body scenario

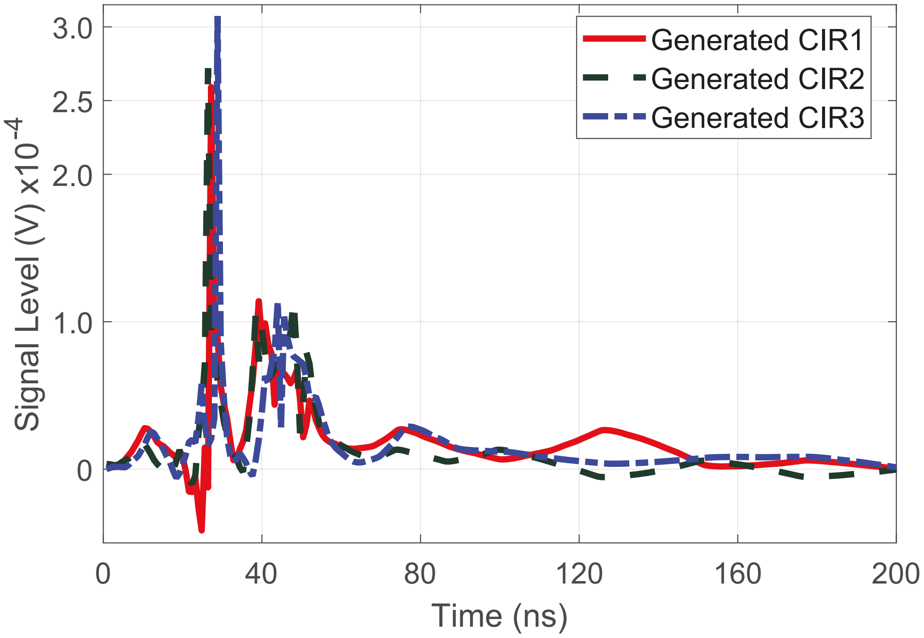

(b) Generated off-body CIRs by CS based random variables model

Figure 6.7: Illusion of generated base CIR and their components.

6.4 Simulation Results

We present some simulation results for channels generated using Algorithm 2, and compare it with real measured data.

Fig. 6.6(a) shows two base CIRs generated by a group of reference coefficients variables following $norm(\mu(\overline{\mathbf{X}}_{tm}), \sigma(\overline{\mathbf{X}}_{tm}))$, and t_{max} index variables following $Round(norm(\mu(\Lambda), \sigma(\Lambda)))$. Ten main components of the base CIR 2 are shown in Fig. 6.6(b). It can be seen that the peaks in both figures occur at around 20 ns and the sharp peak in Fig. 6.6(a) results from a linear combination from positvie/negtive taps of atoms in different wavelet scales.

Fig. 6.7(b) shows 3 CIRs generated from the base CIR 2 in Fig. 6.6(a). The channel features of cluster and power delay profile of the generated CIRs match well with the measured CIRs in Fig. 6.7(a). Note that the cluster structure in the base CIR is ery well reproduced in Fig. 6.7(b), which implies that the proposed algorithm successfully captures the cluster feature in channel modeling.

Fig. 6.8 presents the cumulative probability distributions of the mean delay and Root Mean Square (RMS) delay spread randomly selected from 2000 trials under different scenarios, including CIRs from different heights, body parts and large-scale measurement locations. The mean delay shows a reasonable match, while the difference in RMS delay spread is large [184].

6.5 Conclusion

We presented a scheme for sparse channel modeling using practically measured channel data. The CIRs of the measured channels are characterized by the proposed TA-SOMP algorithm and re-generated by the proposed CS based random variable model. The time alignment operation and coefficient constraint for the analysis and regeneration of multi-channel CIRs are found to play a key role in improving recovery accuracy and simplifying the distributions of coefficients. The proposed methods can be used in sparse analysis and physical layer signal processing in wireless networks.

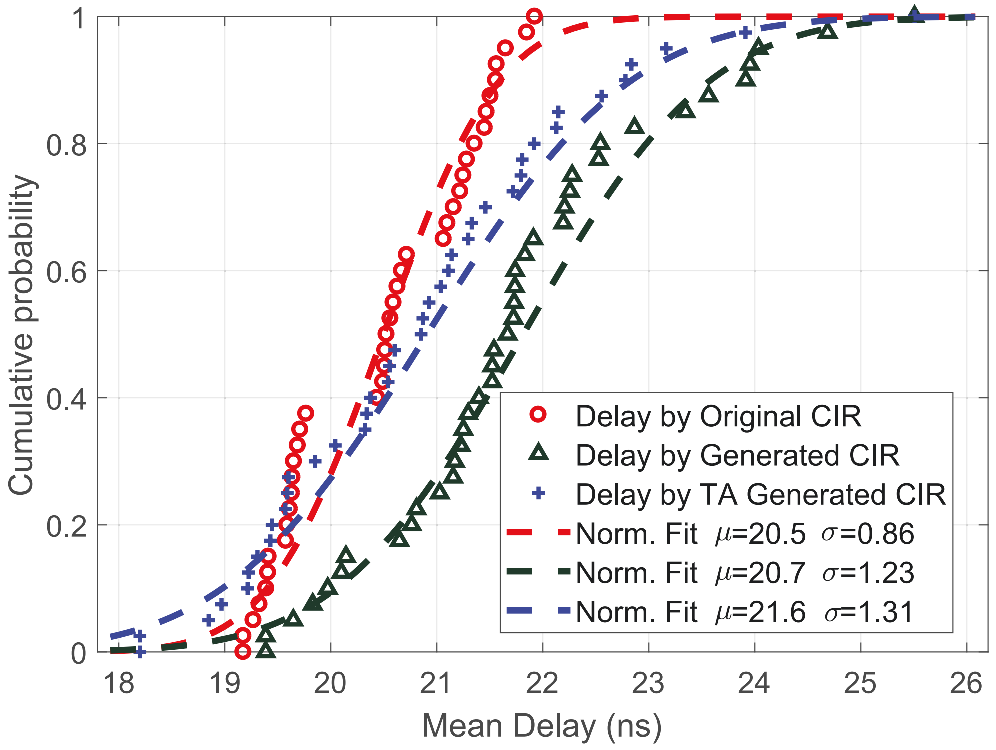

(a) Mean delay comparison

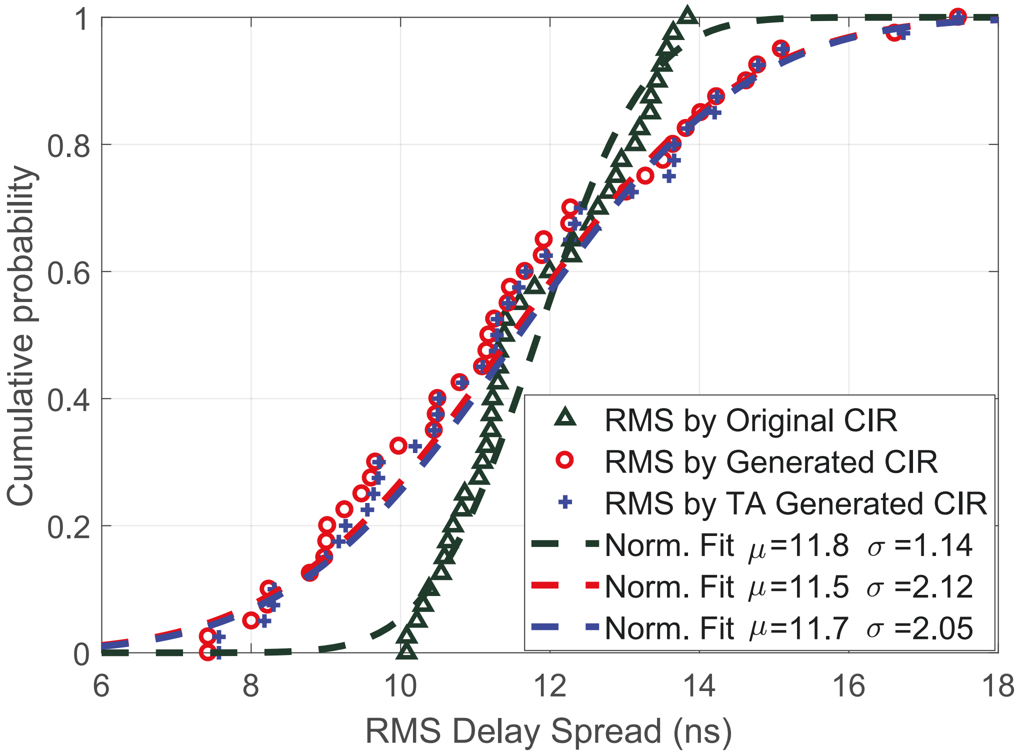

(b) RMS delay spread comparison

Figure 6.8: Comparison of mean delay and RMS delay spread distributions which separately calculated from measured CIRs, generated CIRs with and without time alignment cases.

Chapter 7

Conclusion

Off-body channel propagation characteristics and off-body diversity scheme design are the research hotspots of off-body communication at present, while sparsity analysis and modeling are emerging frontier research directions. They are all important components of 5G deployment and B5G research, and have attracted keen attention from academia, industry and standardization organizations. Therefore, the research of off-body channel has good theoretical exploration value and broad market application prospect. In this chapter, the propagation characteristics analysis and modeling of off-body channel with variable wearable position and variable AP height, spatial diversity of circular polarization, MIMO body-influenced channelčňsparse analysis of off-body channel of single measurement vector based on compressive sensing, and off-body synchronization multi-channel modeling based on multi-measurement vector are studied. This chapter summarizes the main work and looks forward to the future research direction.

7.1 Summary of Contributions

The main work of this thesis can be divided into the following five aspects:

- **SISO off-body channel with variable height and wearing position**
  A two-factor integrated path loss model with variable body worn locations and variable AP height is established to provide a solution of accurate path loss prediction for off-body

channel under complex hospital scenarios. The power loss exponents are modeled as a quadratic function of AP height factor, and the body-worn position loss is considered as a look-up table for covinent extension and easy parameter update. Comparing to traditional large-scale models, the proposed two-factor path loss model is equipped with wider application range, stronger scenario adaptability and deeper insights. Numeric simulation shows that it predicts path loss more accurately than the logarithmic distance height gain model.

- **SIMO circularly/linearly polarized off-body channel**
  A highly reliable circular polarization diversity access scheme is proposed, and a diversity signal model considering the combined gain and polarization mismatch loss is established to provide a robust access solution for wearable networks. By comparing the measured propagation characteristics of traditional Patch and PIFA linear polarization diversity scheme and the proposed circular polarization scheme as well as the theoretical derivation of the diversity signal model, it is found that the proposed circular polarization scheme has significant advantages and can counter the serious receiver and transmitter polarization mismatch loss in wearable communication. Monte carlo simulation further verifies the advantages of the proposed scheme and found that the average received signal strength increased by 2.1dB.

- **MIMO body-related channel analysis and modeling**
  It is found that the impact of human body on indoor massive MIMO channels, using practically measured channel data for a 32x8 massive MIMO system in complex office environment. A parameter of Power Imbalance (PI) indices is introduced to estimate the wide-sense none-stationarity in multiple domains and another parameter of Channel Popularity Indices (CPI) to predict the popularity of MIMO channel. In most cases, the presence of human body still has non-negligible negative impact. It decreases the ergodic capacity by about 8% and increases the path loss exponent by 1. In average, the ergodic capacity for NLOS channels is 15% higher than that for LOS.

- **SISO off-body sparse characteristics analysis and statistical modeling**

  The pulse response model of isolated channel based on single measurement vector compressive sensing (smv-cs) is established, and the compressive sensing framework was innovatively introduced into the channel modeling field to solve the problem that the description of TDL model is not accurate enough and the statistical modeling of SV cluster model is too complex and inflexible. The three balance principle of modeling complexity, precision and sparsity is established. According to this principle, appropriate dictionary of sparse analysis, recovery algorithm and model accuracy selection are carried out. Based on CS rich algorithm library and wavelet dictionary library, the measured wearable channel is modeled for channel impulse response.Thus, a sparse statistical analysis and modeling framework based on smv-cs method is constructed, and a mathematical model of the bridge relationship between channel sparse parameters and propagation of first-order and second-order statistics is established. According to the exponential attenuation characteristics of the channel sparse coefficient vector, three methods of sparse channel modeling for SMV-CS are proposed.Through a large number of Monte Carlo simulations of the measured multi-scene off-body channels and the simulation channel recommended by IEEE802.15.6, it is found that the proposed three models have obvious improvement over the statistical TDL model in complexity and accuracy.

- **Synchronous off-body sparse characteristics analysis and statistical modeling**

  An off-body synchronous sparse channel model based on multi-measurement vector compression sensing technology (MMV-CS) is established to extend the research results of the previous section from single channel to multi-channel synchronous measurement application, so as to solve the modeling problem of high-capacity and high-efficiency off-body networks. In order to meet the urgent needs of high-quality pictures and video acquisition, based on the 3.65GHz continuous bandwidth allocated by WBAN standard in UWB, the design of large scale multiple channels or high bandwidth channel supporting high burst wearable communication requirements cannot be ignored. However, such high-dimensional off-body channels depend on the characteristics of synchronous channels and the construction of synchronous channel modeling method. MMV-CS provides a new solution. In order to use the CS method to effectively extract the co-supported dictionary set of synchronous channel, the algorithms based on wavelet soft threshold de-noising, synchronous channel enhancement measures and adaptive dictionary selection are designed. A synchronization enhancement matching tracking algorithm (TA-SOMP) is implemented to carry out synchronous sparse analysis using wavelet dictionary, and a synchronization sparse channel modeling method is constructed. Compared with traditional modeling methods, it has many advantages, such as low complexity, support for real-time modeling, wide application of scenarios, and great potential for improving accuracy.

7.2 Future Study

Based on the research work I have completed, I find that the future in-depth research can be carried out in the following four aspects:

(1) in terms of the research on the basic characteristics of the off-body channel, it is urgent to carry out special research on the systematic channel modeling method under the influence of human, human motion, and the comprehensive recognition model of motion states, evaluation and analysis supported by remote cloud has the greatest application potential and deserves special research. Although the modeling of path loss characteristics and signal receiving model is carried out in this chapter, more off-body models like RMS delay spread model and power delay spectrum model also have great influence on scene calibration. Specialized research and multi-factor modeling literature are still scarce. These models have important theoretical value and great industrial prospect for off-body channel estimation, codec, simulator design and application deployment.

(2) in the aspect of off-body spatial diversity research, the exploration of multi-diversity influencing factors, diversity gain, MIMO access, the influence of circular polarization, and the exploration of anti-fading methods in complex scenarios (like dense urban, disaster scenes) are all important research directions with great potential. Moreover, there are still very few special researches in the latter two directions. The deployment of multi-diversity plays a great role in promoting the application of virtual reality (VR), augmented reality (AR) and electronic medicine. Therefore, it is of great theoretical significance and practical industrial value to study the key performance indexes like delay, jitter and capacity characteristics of VR and AR applications that have great influence.

(3) the framework of off-body sparse analysis has been preliminarily established in this chapter, but it still needs to be improved, and many constraint features and scene features with great potential are worth further exploration. One of the important directions is to train measured dictionaries that matchs the special scenarios based on sparse learning method. Its application can greatly reduce the recovery sparsity of off-body channel, improve the cluster expression ability, and reduce the performance requirements of the recovery algorithm. Another important direction is the research on the characteristics of off-body sparse vectors and the improvement of sparse modeling methods to promote the flexible representation of cluster structure characteristics such as multipath and multicluster. In addition, the cluster analysis characteristics of single channel based on wavelet dictionary are further explored to build and interpret the bridge between sparse parameters and propagation parameters. This is of great value to the research of rich compressed sensing theory and sparse modeling.

(4) the research on multi-channel joint analysis and modeling framework of off-body synchronization channel is also worth further deepening. The research has two clear directions. One is based on multi-scene channel joint analysis to extract the common sparse characteristics. In this way, the key features of high-dimensional off-body channel sets are grasped to solve some pain points in off-body communication, such as the scheme design to enhance reliability and capacity. The other is the real-time modeling direction of multi-diversity or off-body MIMO channel. The convenient reconstruction of synchronous off-body channel is used to improve the optimal design of off-body MIMO application and support the algorithm development. It is necessary to design more time-domain features that fit the WBAN channel in the two directions of dictionary and recovery algorithm, thus paving the way for low-cost wearable acquisition devices such as EGC and EEG. It also provides a solid foundation for physical layer design, link budget, performance analysis and estimation demodulation algorithm design of off-body

MIMO transmission schemes.

Bibliography

[1] Pengfei Cui. `https://github.com/PerfeyCui/SMV-SparseChannelSimulator`. Single Measurement Vector Sparse Channel Simulator program including GUI, accessed 6-October-2018.

[2] Peter S Hall and Yang Hao. Antennas and propagation for body centric communications. In *2006 First European Conference on Antennas and Propagation*, pages 1–7. IEEE, 2006.

[3] Emil Jovanov, Aleksandar Milenkovic, Chris Otto, Piet De Groen, B Johnson, S Warren, and G Taibi. A WBAN system for ambulatory monitoring of physical activity and health status: applications and challenges. In *2005 IEEE Engineering in Medicine and Biology 27th Annual Conference*, pages 3810–3813. IEEE, 2006.

[4] Nacer Chahat, Maxim Zhadobov, Laurent Le Coq, Stanislav I Alekseev, and Ronan Sauleau. Characterization of the interactions between a 60-GHz antenna and the human body in an off-body scenario. *IEEE Transactions on Antennas and Propagation*, 60(12):5958–5965, 2012.

[5] M G Doone, S L Cotton, and C Oestges. An Experimental Investigation into the Impact of Vehicular Traffic on Interpersonal Wearable-to-Wearable Communications Channels. *IEEE Transactions on Antennas and Propagation*, 65(10):5418–5430, 2017.

[6] Peter S Hall. *Antennas and propagation for body-centric wireless communications.* Artech house, 2012.

[7] IEEE Standard for Local and metropolitan area networks - Part 15.6: Wireless Body Area Networks. *IEEE Std 802.15.6-2012*, pages 1–271, 2012.

[8] Harald T Friis. A note on a simple transmission formula. *proc. IRE*, 34(5):254–256, 1946.

[9] Slawomir J Ambroziak, Luis M Correia, Ryszard J Katulski, Michal Mackowiak, Carla Oliveira, Jaroslaw Sadowski, and Kenan Turbic. An off-body channel model for body area networks in indoor environments. *IEEE Transactions on Antennas and Propagation*, 64(9):4022–4035, 2016.

[10] Ruben-Gregorio Garcia-Serna, Concepcion Garcia-Pardo, and Jose-Maria Molina-Garcia-Pardo. Effect of the receiver attachment position on ultrawideband off-body channels. *IEEE Antennas Wireless Propag. Lett*, 14:1101–1104, 2015.

[11] Stephane Van Roy, Francois Quitin, LingFeng Liu, Claude Oestges, François Horlin, Jean-Michel Dricot, and Philippe De Doncker. Dynamic channel modeling for multi-sensor body area networks. *IEEE Transactions on Antennas and Propagation*, 61(4):2200–2208, 2013.

[12] Mohammad Monirujjaman Khan, Qammer Hussain Abbasi, Akram Alomainy, Yang Hao, and Clive Parini. Experimental characterisation of ultra-wideband off-body radio channels considering antenna effects. *IET Microwaves, Antennas & Propagation*, 7(5):370–380, 2013.

[13] P Catherwood and W Scanlon. Off-body UWB channel characterisation within a hospital ward environment. *International. Journal on Ultra Wideband Communications & Systems*, 1(4):263–272, 2010.

[14] A A Goulianos, T W C Brown, and S Stavrou. Ultra-wideband measurements and results for sparse off-body communication channels. In *2008 Loughborough Antennas and Propagation Conference*, pages 213–216. IEEE, 2008.

[15] Philip A Catherwood and William G Scanlon. Link characteristics for an off-body UWB transmitter in a hospital environment. In *2009 Loughborough Antennas & Propagation Conference*, pages 569–572. IEEE, 2009.

[16] Patrick Van Torre, Luigi Vallozzi, Lennert Jacobs, Hendrik Rogier, Marc Moeneclaey, and Jo Verhaevert. Characterization of measured indoor off-body MIMO channels with correlated fading, correlated shadowing and constant path loss. *IEEE Transactions on Wireless Communications*, 11(2):712–721, 2012.

[17] Koichi Ogawa and Kazuhiro Honda. BAN shadowing properties of an arm-waving dynamic phantom. In *2012 6th European Conference on Antennas and Propagation (EUCAP)*, pages 515–519. IEEE, 2012.

[18] Simon L Cotton. A statistical model for shadowed body-centric communications channels: Theory and validation. *IEEE Transactions on Antennas and Propagation*, 62(3):1416–1424, 2014.

[19] Imdad Khan. *Diversity and MIMO for body-centric wireless communication channels*. PhD thesis, University of Birmingham, 2009.

[20] P. Cui, Y. Yu, Y. Liu, W. Lu, and H. Zhu. Joint rls and lms adaptive equalization for indoor wireless communications under staircase environments. In *2015 International Conference on Wireless Communications Signal Processing (WCSP)*, pages 1–5, Oct 2015.

[21] William C Jakes and Donald C Cox. *Microwave mobile communications*. Wiley-IEEE Press, 1994.

[22] Donald G Brennan. Linear diversity combining techniques. *Proceedings of the IRE*, 47(6):1075–1102, 1959.

[23] John G Proakis and Masoud Salehi. *Digital communications*, volume 4. McGraw-hill New York, 2001.

[24] Anupam R Chandran, Gareth A Conway, and William G Scanlon. Pattern switching compact patch antenna for on-body and off-body communications at 2.45 GHz. In *2009 3rd European Conference on Antennas and Propagation*, pages 2055–2057. IEEE, 2009.

[25] M T Ivrlac and J A Nossek. Quantifying diversity and correlation in Rayleigh fading MIMO communication systems. In *Proceedings of the 3rd IEEE International Symposium on Signal Processing and Information Technology (IEEE Cat. No. 03EX795)*, pages 158–161. IEEE, 2003.

[26] Patrick Van Torre, Luigi Vallozzi, Hendrik Rogier, and Jo Verhaevert. Diversity textile antenna systems for firefighters. In *Proceedings of the fourth European Conference on Antennas and Propagation*, pages 1–5. IEEE, 2010.

[27] Qammer Hussain Abbasi, Masood Ur Rehman, Hassan Tariq Chattha, Khalid Qaraqe, Akram Alomainy, Yang Hao, and Clive Parini. Ultra wideband antenna diversity characterisation for off-body communications in an indoor environment. *IET Microwaves, Antennas & Propagation*, 8(14):1161–1169, 2014.

[28] Simon L Cotton and William G Scanlon. Measurements, modeling and simulation of the off-body radio channel for the implementation of bodyworn antenna diversity at 868 MHz. *IEEE Transactions on Antennas and Propagation*, 57(12):3951–3961, 2009.

[29] Marina Marinova, Arno Thielens, Emmeric Tanghe, Luigi Vallozzi, Günter Vermeeren, Wout Joseph, Hendrik Rogier, and Luc Martens. Diversity performance of off-body MB-OFDM UWB-MIMO. *IEEE Transactions on Antennas and Propagation*, 63(7):3187–3197, 2015.

[30] Ameenulla J Ali, Simon L Cotton, and William G Scanlon. Spatial diversity for off-body communications in an indoor populated environment at 5.8 GHz. In *Antennas & Propagation Conference, 2009. LAPC 2009. Loughborough*, pages 641–644. IEEE, 2009.

[31] Chunsu Ahn, Byoungjik Ahn, Sunwoo Kim, and Jaehoon Choi. Experimental outage capacity analysis for off-body wireless body area network channel with transmit diversity. *IEEE Transactions on Consumer Electronics*, 58(2):274–277, 2012.

[32] Qammer H Abbasi, Mohammad Monirrujjman Khan, Akram Alomainy, and Yang Hao. Diversity antenna techniques for enhanced ultra wideband body-centric communications.

In *2011 IEEE International Symposium on Antennas and Propagation (APSURSI)*, pages 1323–1326. IEEE, 2011.

[33] Sławomir J Ambroziak, Lu\'\is M Correia, Ryszard J Katulski, and Michał Maćkowiak. Impact of radio wave polarisation on off-body communications in indoor environments. In *2015 9th European Conference on Antennas and Propagation (EuCAP)*, pages 1–3. IEEE, 2015.

[34] Patrick Van Torre, Luigi Vallozzi, Carla Hertleer, Hendrik Rogier, Marc Moeneclaey, and Jo Verhaevert. Indoor off-body wireless MIMO communication with dual polarized textile antennas. *IEEE Transactions on Antennas and Propagation*, 59(2):631–642, 2011.

[35] Jason Carter, Jason Saberin, Tejal Shah, and Cynthia Furse. Inexpensive fabric antenna for off-body wireless sensor communication. In *2010 IEEE Antennas and Propagation Society International Symposium*, pages 1–4. IEEE, 2010.

[36] Carla Hertleer, Lieva Van Langenhove, and Hendrik Rogier. Printed textile antennas for off-body communication. In *Advances in science and technology*, volume 60, pages 64–66. Trans Tech Publ, 2008.

[37] Theodoros Mavridis, Luca Petrillo, Julien Sarrazin, David Lautru, Aziz Benlarbi-Delai, and Philippe De Doncker. Theoretical and experimental investigation of a 60-GHz off-body propagation model. *IEEE transactions on antennas and propagation*, 62(1):393–402, 2014.

[38] Xiao-Qi Zhu, Yong-Xin Guo, and Wen Wu. Miniaturized dual-band and dual-polarized antenna for MBAN applications. *IEEE Transactions on Antennas and Propagation*, 64(7):2805–2814, 2016.

[39] D Ma and W X Zhang. A dual-band dual-polarized antenna for body area network. In *Proceedings of the Fourth European Conference on Antennas and Propagation*, pages 1–5. IEEE, 2010.

[40] Orestis Georgiou. Polarized Rician fading models for performance analysis in cellular networks. *IEEE Communications Letters*, 20(6):1255–1258, 2016.

[41] Theodore S Rappaport and Dwayne A Hawbaker. Wide-band microwave propagation parameters using circular and linear polarized antennas for indoor wireless channels. *IEEE Transactions on Communications*, 40(2):240–245, 1992.

[42] GE Panagopoulos, AD and Chatzarakis. Outage performance of single/dual polarized fixed wireless access links in heavy rain climatic regions. *Journal of Electromagnetic Waves and Applications*, 21(3):283—-297, 2007.

[43] Søren H Kvist, Pablo F Medina, Jesper Thaysen, and Kaj B Jakobsen. On-body and off-body 2.45 GHz MIMO communications for hearing instrument applications. In *2013 7th European Conference on Antennas and Propagation (EuCAP)*, pages 2595–2599. IEEE, 2013.

[44] S Gao, S Xiao, H Zhu, W Shao, and B-Z Wang. 2.45 GHz body-worn planar monopole antenna and its application in body-worn MIMO system. *Journal of Electromagnetic Waves and Applications*, 25(5-6):661–671, 2011.

[45] Carla Oliveira, Michal Mackowiak, and Lu\’\is M Correia. Modelling on-and off-body channels in body area networks. In *2013 SBMO/IEEE MTT-S International Microwave & Optoelectronics Conference (IMOC)*, pages 1–5. IEEE, 2013.

[46] Patrick Van Torre, Luigi Vallozzi, Hendrik Rogier, Marc Moeneclaey, and Jo Verhaevert. Reliable MIMO communication between firefighters equipped with wearable antennas and a base station using space-time codes. In *Proceedings of the 5th European Conference on Antennas and Propagation (EUCAP)*, pages 2690–2694. IEEE, 2011.

[47] I Khan, I Ullah, and P S Hall. Transmit–receive diversity for 2 × 2 multiple-input multiple-output channel in body area networks. *IET microwaves, antennas & propagation*, 5(13):1589–1593, 2011.

[48] S K Yoo and S L Cotton. An evaluation of micro and macro based diversity combining for wearable communications. In *2017 IEEE International Symposium on Antennas and Propagation USNC/URSI National Radio Science Meeting*, pages 1405–1406, 2017.

[49] Peng-Fei Cui, Yu Yu, Wen-Jun Lu, Yang Liu, and Hong-Bo Zhu. Measurement and Modeling of Wireless Off-Body Propagation Characteristics Under Hospital Environment at 6–8.5 GHz. *IEEE Access*, 5:10915–10923, 2017.

[50] David L Donoho, Arian Maleki, and Andrea Montanari. Message-passing algorithms for compressed sensing. *Proceedings of the National Academy of Sciences*, 106(45):18914–18919, 2009.

[51] Moshe Mishali and Yonina C Eldar. From theory to practice: Sub-Nyquist sampling of sparse wideband analog signals. *IEEE Journal of Selected Topics in Signal Processing*, 4(2):375–391, 2010.

[52] Yilun Chen, Moshe Mishali, Yonina C Eldar, and Alfred O Hero. Modulated wideband converter with non-ideal lowpass filters. In *2010 IEEE International Conference on Acoustics, Speech and Signal Processing*, pages 3630–3633. IEEE, 2010.

[53] Richard Bellman. Dynamic programming. *Science*, 153(3731):34–37, 1966.

[54] Gerard V Trunk. A problem of dimensionality: A simple example. *IEEE Transactions on Pattern Analysis & Machine Intelligence*, (3):306–307, 1979.

[55] Christopher M Bishop. *Pattern recognition and machine learning.* springer, 2006.

[56] Jon F Claerbout and Francis Muir. Robust modeling with erratic data. *Geophysics*, 38(5):826–844, 1973.

[57] B S Kasin. The widths of certain finite-dimensional sets and classes of smooth functions. *Izv. Akad. Nauk SSSR Ser. Mat*, 41(2):334–351, 1977.

[58] Efim Davydovich Gluskin. Norms of random matrices and widths of finite-dimensional sets. *Mathematics of the USSR-Sbornik*, 48(1):173, 1984.

[59] Emmanuel Candes, Justin Romberg, and Terence Tao. Robust uncertainty principles: Exact signal reconstruction from highly incomplete frequency information. *arXiv preprint math/0409186*, 2004.

[60] Emmanuel J Candès and Michael B Wakin. An introduction to compressive sampling [a sensing/sampling paradigm that goes against the common knowledge in data acquisition]. *IEEE signal processing magazine*, 25(2):21–30, 2008.

[61] Jun Won Choi, Byonghyo Shim, Yacong Ding, Bhaskar Rao, and Dong In Kim. Compressed sensing for wireless communications: Useful tips and tricks. *IEEE Communications Surveys & Tutorials*, 19(3):1527–1550, 2017.

[62] Saad Qaisar, Rana Muhammad Bilal, Wafa Iqbal, Muqaddas Naureen, and Sungyoung Lee. Compressive sensing: From theory to applications, a survey. *Journal of Communications and networks*, 15(5):443–456, 2013.

[63] Waheed U Bajwa, Jarvis Haupt, Akbar M Sayeed, and Robert Nowak. Compressed channel sensing: A new approach to estimating sparse multipath channels. *Proceedings of the IEEE*, 98(6):1058–1076, 2010.

[64] Christian R Berger, Zhaohui Wang, Jianzhong Huang, and Shengli Zhou. Application of compressive sensing to sparse channel estimation. *IEEE Communications Magazine*, 48(11), 2010.

[65] Omar El Ayach, Sridhar Rajagopal, Shadi Abu-Surra, Zhouyue Pi, and Robert W Heath. Spatially sparse precoding in millimeter wave MIMO systems. *IEEE transactions on wireless communications*, 13(3):1499–1513, 2014.

[66] Philip Schniter and Akbar Sayeed. Channel estimation and precoder design for millimeter-wave communications: The sparse way. In *2014 48th Asilomar Conference on Signals, Systems and Computers*, pages 273–277. IEEE, 2014.

[67] Sinh Le Hong Nguyen and Ali Ghrayeb. Compressive sensing-based channel estimation for massive multiuser MIMO systems. In *2013 IEEE Wireless Communications and Networking Conference (WCNC)*, pages 2890–2895. IEEE, 2013.

[68] Jia Meng, Wotao Yin, Yingying Li, Nam Tuan Nguyen, and Zhu Han. Compressive sensing based high-resolution channel estimation for OFDM system. *IEEE Journal of Selected Topics in Signal Processing*, 6(1):15–25, 2012.

[69] Zhen Gao, Linglong Dai, and Zhaocheng Wang. Structured compressive sensing based superimposed pilot design in downlink large-scale MIMO systems. *Electronics Letters*, 50(12):896–898, 2014.

[70] Athanasios A Rontogiannis and Kostas Berberidis. Efficient decision feedback equalization for sparse wireless channels. *IEEE Transactions on wireless communications*, 2(3):570–581, 2003.

[71] Ahmed Alkhateeb, Geert Leus, and Robert W Heath. Compressed sensing based multi-user millimeter wave systems: How many measurements are needed? In *2015 IEEE International Conference on Acoustics, Speech and Signal Processing (ICASSP)*, pages 2909–2913. IEEE, 2015.

[72] Zhilin Zhang, Tzyy-Ping Jung, Scott Makeig, and Bhaskar D Rao. Compressed sensing of EEG for wireless telemonitoring with low energy consumption and inexpensive hardware. *IEEE Transactions on Biomedical Engineering*, 60(1):221–224, 2013.

[73] Hossein Mamaghanian, Nadia Khaled, David Atienza, and Pierre Vandergheynst. Compressed sensing for real-time energy-efficient ECG compression on wireless body sensor nodes. *IEEE Transactions on Biomedical Engineering*, 58(9):2456–2466, 2011.

[74] Anna M R Dixon, Emily G Allstot, Daibashish Gangopadhyay, and David J Allstot. Compressed sensing system considerations for ECG and EMG wireless biosensors. *IEEE Transactions on Biomedical Circuits and Systems*, 6(2):156–166, 2012.

[75] Mohammadreza Balouchestani, Kaamran Raahemifar, and Sridhar Krishnan. Low power wireless body area networks with compressed sensing theory. In *2012 IEEE 55th International Midwest Symposium on Circuits and Systems (MWSCAS)*, pages 916–919. IEEE, 2012.

[76] Xiaodong Yang, Aifeng Ren, Zhiya Zhang, Masood Ur Rehman, Qammer Hussain Abbasi, and Akram Alomainy. Towards sparse characterisation of on-body ultra-wideband wireless channels. *Healthcare technology letters*, 2(3):74–77, 2015.

[77] Nguyen Thanh Son, Shuxu Guo, and Haipeng Chen. Impact of channel models on compressed sensing recovery algorithms-based ultra-wideband channel estimation. *IET Communications*, 7(13):1322–1330, 2013.

[78] Joel A Tropp, Jason N Laska, Marco F Duarte, Justin K Romberg, and Richard G Baraniuk. Beyond Nyquist: Efficient sampling of sparse bandlimited signals. *arXiv preprint arXiv:0902.0026*, 2009.

[79] David L Donoho. Compressed sensing. *IEEE Transactions on information theory*, 52(4):1289–1306, 2006.

[80] Emmanuel J Candès and Others. Compressive sampling. In *Proceedings of the international congress of mathematicians*, volume 3, pages 1433–1452. Madrid, Spain, 2006.

[81] Richard G Baraniuk. Compressive sensing. *IEEE signal processing magazine*, 24(4), 2007.

[82] Joel A Tropp and Anna C Gilbert. Signal recovery from random measurements via orthogonal matching pursuit. *IEEE Transactions on information theory*, 53(12):4655–4666, 2007.

[83] Jian Wang, Seokbeop Kwon, and Byonghyo Shim. Generalized orthogonal matching pursuit. *IEEE Transactions on signal processing*, 60(12):6202–6216, 2012.

[84] Deanna Needell and Joel A Tropp. CoSaMP: Iterative signal recovery from incomplete and inaccurate samples. *Applied and computational harmonic analysis*, 26(3):301–321, 2009.

[85] Wei Dai and Olgica Milenkovic. Subspace pursuit for compressive sensing signal reconstruction. *IEEE transactions on Information Theory*, 55(5):2230–2249, 2009.

[86] Suhyuk Kwon, Jian Wang, and Byonghyo Shim. Multipath matching pursuit. *IEEE Transactions on Information Theory*, 60(5):2986–3001, 2014.

[87] Scott Shaobing Chen, David L Donoho, and Michael A Saunders. Atomic decomposition by basis pursuit. *SIAM review*, 43(1):129–159, 2001.

[88] Emmanuel J Candes, Michael B Wakin, and Stephen P Boyd. Enhancing sparsity by reweighted ? 1 minimization. *Journal of Fourier analysis and applications*, 14(5-6):877–905, 2008.

[89] Thomas Blumensath and Mike E Davies. Iterative hard thresholding for compressed sensing. *Applied and computational harmonic analysis*, 27(3):265–274, 2009.

[90] Mohsen Bayati and Andrea Montanari. The dynamics of message passing on dense graphs, with applications to compressed sensing. *IEEE Transactions on Information Theory*, 57(2):764–785, 2011.

[91] Mário Figueiredo. Adaptive sparseness using Jeffreys prior. In *Advances in neural information processing systems*, pages 697–704, 2002.

[92] David P Wipf and Bhaskar D Rao. Sparse Bayesian learning for basis selection. *IEEE Transactions on Signal processing*, 52(8):2153–2164, 2004.

[93] Shihao Ji, Ya Xue, Lawrence Carin, and Others. Bayesian compressive sensing. *IEEE Transactions on signal processing*, 56(6):2346, 2008.

[94] Xiongwen Zhao, Jarmo Kivinen, and P Vainnikainen. Tapped delay line channel models at 5.3 GHz in indoor environments. In *Vehicular Technology Conference, 2000. IEEE-VTS Fall VTC 2000. 52nd*, volume 1, pages 1–5. IEEE, 2000.

[95] Dajana Cassioli, Moe Z Win, and Andreas F Molisch. The ultra-wide bandwidth indoor channel: from statistical model to simulations. *IEEE Journal on selected areas in Communications*, 20(6):1247–1257, 2002.

[96] G R Hiertz, Y Zang, J Habetha, and H Sirin. IEEE 802.15.3a Wireless Personal Area Networks - The MBOA Approach. In *11th European Wireless Conference 2005 - Next Generation wireless and Mobile Communications and Services*, pages 1–7, 2006.

[97] Adel A M Saleh and Reinaldo Valenzuela. A statistical model for indoor multipath propagation. *IEEE Journal on selected areas in communications*, 5(2):128–137, 1987.

[98] ETSI. LTE; 5G; study on channel model for frequency spectrum above 6 GHz. *3GPP TR 38.900 version 14.2.0 Release 14*, 2017.

[99] Stephan Jaeckel, Leszek Raschkowski, Kai Börner, and Lars Thiele. QuaDRiGa: A 3-D multi-cell channel model with time evolution for enabling virtual field trials. *IEEE Transactions on Antennas and Propagation*, 62(6):3242–3256, 2014.

[100] David L Donoho. Compressed sensing. *IEEE Transactions on information theory*, 52(4):1289–1306, 2006.

[101] Z. Gao, L. Dai, S. Han, C. I, Z. Wang, and L. Hanzo. Compressive sensing techniques for next-generation wireless communications. *IEEE Wireless Commun.*, 25(3):144–153, June 2018.

[102] Nguyen Thanh Son, Shuxu Guo, and Haipeng Chen. Impact of channel models on compressed sensing recovery algorithms-based ultra-wideband channel estimation. *IET Communications*, 7(13):1322–1330, 2013.

[103] Christian R Berger, Zhaohui Wang, Jianzhong Huang, and Shengli Zhou. Application of compressive sensing to sparse channel estimation. *IEEE Communications Magazine*, 48(11), 2010.

[104] Liefeng Bo, Xiaofeng Ren, and Dieter Fox. Multipath sparse coding using hierarchical matching pursuit. In *Proceedings of the IEEE Conference on Computer Vision and Pattern Recognition*, pages 660–667, 2013.

[105] Bruno A Olshausen and David J Field. Sparse coding with an overcomplete basis set: A strategy employed by V1? *Vision research*, 37(23):3311–3325, 1997.

[106] Jianchao Yang, Kai Yu, Yihong Gong, and Thomas Huang. Linear spatial pyramid matching using sparse coding for image classification. In *Computer Vision and Pattern Recognition, 2009. CVPR 2009. IEEE Conference on*, pages 1794–1801. IEEE, 2009.

[107] Ahmed Iyanda Sulyman, Abdulmalik Alwarafy, George R MacCartney, Theodore S Rappaport, and Abdulhameed Alsanie. Directional radio propagation path loss models for millimeter-wave wireless networks in the 28-, 60-, and 73-ghz bands. *IEEE Transactions on Wireless Communications*, 15(10):6939–6947, 2016.

[108] Dalin Zhu, Junil Choi, Qian Cheng, Weimin Xiao, and Robert W Heath Jr. High-resolution angle tracking for mobile wideband millimeter-wave systems with antenna array calibration. *IEEE Transactions on Wireless Communications*, 17(11):7173–7189, 2018.

[109] Waheed U Bajwa, Akbar Sayeed, and Robert Nowak. Sparse multipath channels: Modeling and estimation. In *Digital Signal Processing Workshop and 5th IEEE Signal Processing Education Workshop, 2009. DSP/SPE 2009. IEEE 13th*, pages 320–325. IEEE, 2009.

[110] Georg Taubock, Franz Hlawatsch, Daniel Eiwen, and Holger Rauhut. Compressive estimation of doubly selective channels in multicarrier systems: Leakage effects and sparsity-enhancing processing. *IEEE Journal of Selected Topics in Signal Processing*, 4(2):255–271, 2010.

[111] Tan Wang, Gen Li, Jiaxin Ding, Qingyu Miao, Jingchun Li, and Ying Wang. 5g spectrum: Is china ready? *IEEE Communications Magazine*, 53(7):58–65, 2015.

[112] Pekka Pirinen. A brief overview of 5g research activities. In *5G for Ubiquitous Connectivity (5GU), 2014 1st International Conference on*, pages 17–22. IEEE, 2014.

[113] Slawomir J Ambroziak, Luis M Correia, Ryszard J Katulski, Michal Mackowiak, Carla Oliveira, Jaroslaw Sadowski, and Kenan Turbic. An off-body channel model for body area networks in indoor environments. *IEEE Transactions on Antennas and Propagation*, 64(9):4022–4035, 2016.

[114] Yang Hao, A Alomainy, PS Hall, YI Nechayev, CG Parini, and CC Constantinou. Antennas and propagation for body centric wireless communications. In *Wireless Communications and Applied Computational Electromagnetics, 2005. IEEE/ACES International Conference on*, pages 586–589. IEEE, 2005.

[115] David Smith, Leif Hanlen, Jian Zhang, Dino Miniutti, David Rodda, and Ben Gilbert. Characterization of the dynamic narrowband on-body to off-body area channel. In *Communications, 2009. ICC'09. IEEE International Conference on*, pages 1–6. IEEE, 2009.

[116] Attaphongse Taparugssanagorn, Carlos Pomalaza-Ráez, Ari Isola, Raffaello Tesi, Matti Hamalainen, and Jari Iinatti. Uwb channel modelling for wireless body area networks in a hospital. *International Journal of Ultra Wideband Communications and Systems*, 1(4):226–236, 2010.

[117] TS Rapparport. Mobile radio propagation: large-scale path loss'. *Wireless Communications: Principles & Practice*, 1996.

[118] Renny E Badra and Alfonso Zambrano. Street-level los/nlos model for urban macrocells based on observations. In *Wireless Communications and Networking Conference (WCNC), 2011 IEEE*, pages 1294–1297. IEEE, 2011.

[119] Zhao Min, Wu Muqing, Hu Qian, Di Shiping, Zhou Panfeng, Zeng Xiangbing, and Ge Shuyun. A two-dimensional integrated channel model for train-ground communications. In *Telecommunications (ICT), 2014 21st International Conference on*, pages 348–352. IEEE, 2014.

[120] J Foerster et al. Ieee p802. 15 working group for wireless personal area networks (wpans), channel modeling subcommittee report-final. *IEEE J. Sel. Areas Commun*, 2003.

[121] Peng-Fei Cui, Yu Yu, Yang Liu, Wen-Jun Lu, and Hong-Bo Zhu. Body obstruction characteristics for off-body channel under hospital environment at 6 8.5 ghz. In *Ubiquitous Wireless Broadband (ICUWB), 2016 IEEE International Conference on*, pages 1–4. IEEE, 2016.

[122] Simon L Cotton and William G Scanlon. Channel characterization for single-and multiple-antenna wearable systems used for indoor body-to-body communications. *IEEE Transactions on Antennas and Propagation*, 57(4):980–990, 2009.

[123] Qing-Nian Zhang, Ji Zhang, Dan-Yang Zhang, Wen-Jun Lu, Kin Fai Tong, and Hong-Bo Zhu. A wearable loop-dipole combined antenna. In *Electromagnetics: Applications and Student Innovation Competition (iWEM), 2016 IEEE International Workshop on*, pages 1–3. IEEE, 2016.

[124] Yu Yu, Yang Liu, Wen-Jun Lu, and Hong-Bo Zhu. Path loss model with antenna height dependency under indoor stair environment. *International Journal of Antennas and Propagation*, 2014, 2014.

[125] Yang Liu, Yu Yu, Wen-Jun Lu, and Hong-Bo Zhu. Antenna-height-dependent path loss model and shadowing characteristics under indoor stair environment at 2.6 ghz. *IEEJ Transactions on Electrical and Electronic Engineering*, 10(5):498–502, 2015.

[126] Ye Wang, Wen-Jun Lu, Hong-Bo Zhu, et al. Propagation characteristics of the lte indoor radio channel with persons at 2.6 ghz. *IEEE Antennas and Wireless Propagation Letters*, 12:991–994, 2013.

[127] Ye Wang, Wen-jun Lu, and Hong-bo Zhu. Study on multipath propagation characteristics for lte indoor environment with persons. In *Wireless Symposium (IWS), 2013 IEEE International*, pages 1–4. IEEE, 2013.

[128] Peter S Hall, Yang Hao, Yuriy I Nechayev, Akram Alomainy, Costas C Constantinou, Clive Parini, Muhammad R Kamarudin, Tareq Z Salim, David TM Hee, Rostyslav Dubrovka, et al. Antennas and propagation for on-body communication systems. *IEEE Antennas and Propagation Magazine*, 49(3):41–58, 2007.

[129] Jung-Hwan Hwang, Tae-Wook Kang, Youn-Tae Kim, and Seong-Ook Park. Measurement of transmission properties of hbc channel and its impulse response model. *IEEE Transactions on Instrumentation and Measurement*, 65(1):177–188, 2016.

[130] Marc Simon Wegmueller, Michael Oberle, Norbert Felber, Niels Kuster, and Wolfgang Fichtner. Signal transmission by galvanic coupling through the human body. *IEEE Transactions on Instrumentation and Measurement*, 59(4):963–969, 2010.

[131] Saeed S Ghassemzadeh, Rittwik Jana, Christopher W Rice, William Turin, and Vahid Tarokh. Measurement and modeling of an ultra-wide bandwidth indoor channel. *IEEE Transactions on Communications*, 52(10):1786–1796, 2004.

[132] Homayoun Hashemi. The indoor radio propagation channel. *Proceedings of the IEEE*, 81(7):943–968, 1993.

[133] Greg Durgin, Theodore S Rappaport, and Hao Xu. Measurements and models for radio path loss and penetration loss in and around homes and trees at 5.85 ghz. *IEEE Transactions on Communications*, 46(11):1484–1496, 1998.

[134] J Foerster et al. Ieee p802. 15 working group for wireless personal area networks (wpans), channel modeling subcommittee report-final. *IEEE J. Sel. Areas Commun*, 2003.

[135] Kotaro Yamasue, Yuya Obinata, Kenichi Takizawa, Chika Sugimoto, and Ryuji Kohno. Measures against shadowing problem on a bed using high-band uwb-ban. In *Medical In-*

formation and Communication Technology (ISMICT), 2013 7th International Symposium on, pages 198–202. IEEE, 2013.

[136] Seok H Choi, Jong K Park, Sun K Kim, and Jae Y Park. A new ultra-wideband antenna for uwb applications. *Microwave and optical technology letters*, 40(5):399–401, 2004.

[137] Yong-Ling Ban, Chuan Li, Gang Wu, Kin-Lu Wong, et al. 4g/5g multiple antennas for future multi-mode smartphone applications. *IEEE Access*, 4:2981–2988, 2016.

[138] Akihiro Kajiwara. Line-of-sight indoor radio communication using circular polarized waves. *IEEE Transactions on Vehicular Technology*, 44(3):487–493, 1995.

[139] Qammer Hussain Abbasi, Andrea Sani, Akram Alomainy, and Yang Hao. On-body radio channel characterization and system-level modeling for multiband ofdm ultra-wideband body-centric wireless network. *IEEE Transactions on Microwave Theory and Techniques*, 58(12):3485–3492, 2010.

[140] Yan Zhao, Yang Hao, Akram Alomainy, and Clive Parini. Uwb on-body radio channel modeling using ray theory and subband fdtd method. *IEEE Transactions on Microwave Theory and Techniques*, 54(4):1827–1835, 2006.

[141] Huasong Cao, Victor Leung, Cupid Chow, and Henry Chan. Enabling technologies for wireless body area networks: A survey and outlook. *IEEE Communications Magazine*, 47(12), 2009.

[142] Slawomir J Ambroziak, Luis M Correia, Ryszard J Katulski, Michal Mackowiak, Carla Oliveira, Jaroslaw Sadowski, and Kenan Turbic. An off-body channel model for body area networks in indoor environments. *IEEE Transactions on Antennas and Propagation*, 64(9):4022–4035, 2016.

[143] Ruben-Gregorio Garcia-Serna, Concepcion Garcia-Pardo, and Jose-Maria Molina-Garcia-Pardo. Effect of the receiver attachment position on ultrawideband off-body channels. *IEEE Antennas Wireless Propag. Lett*, 14:1101–1104, 2015.

[144] Ameenulla J Ali, Simon L Cotton, and William G Scanlon. Spatial diversity for off-body communications in an indoor populated environment at 5.8 ghz. In *Antennas & Propagation Conference, 2009. LAPC 2009. Loughborough*, pages 641–644. IEEE, 2009.

[145] Simon L Cotton and William G Scanlon. Measurements, modeling and simulation of the off-body radio channel for the implementation of bodyworn antenna diversity at 868 mhz. *IEEE Transactions on Antennas and Propagation*, 57(12):3951–3961, 2009.

[146] Yu Yu, Yang Liu, Wen-Jun Lu, and Hong-Bo Zhu. Path loss model with antenna height dependency under indoor stair environment. *International Journal of Antennas and Propagation*, 2014, 2014.

[147] Yang Liu, Yu Yu, Wen-Jun Lu, and Hong-Bo Zhu. Antenna-height-dependent path loss model and shadowing characteristics under indoor stair environment at 2.6 ghz. *IEEJ Transactions on Electrical and Electronic Engineering*, 10(5):498–502, 2015.

[148] Orestis Georgiou. Polarized rician fading models for performance analysis in cellular networks. *IEEE Communications Letters*, 20(6):1255–1258, 2016.

[149] Theodore S Rappaport and Dwayne A Hawbaker. Wide-band microwave propagation parameters using circular and linear polarized antennas for indoor wireless channels. *IEEE Transactions on Communications*, 40(2):240–245, 1992.

[150] AD Panagopoulos and GE Chatzarakis. Outage performance of single/dual polarized fixed wireless access links in heavy rain climatic regions. *Journal of Electromagnetic Waves and Applications*, 21(3):283–297, 2007.

[151] Wen-Jun Lu, Jing-Wen Shi, Kin-Fai Tong, and Hong-Bo Zhu. Planar endfire circularly polarized antenna using combined magnetic dipoles. *IEEE Antennas and Wireless Propagation Letters*, 14:1263–1266, 2015.

[152] Riku M Makinen and Tiiti Kellomaki. Body effects on thin single-layer slot, self-complementary, and wire antennas. *IEEE Transactions on Antennas and Propagation*, 62(1):385–392, 2014.

[153] Mohammad Monirujjaman Khan, Qammer Hussain Abbasi, Akram Alomainy, Yang Hao, and Clive Parini. Experimental characterisation of ultra-wideband off-body radio channels considering antenna effects. *IET Microwaves, Antennas & Propagation*, 7(5):370–380, 2013.

[154] Theodore S Rappaport et al. *Wireless communications: principles and practice*, volume 2. prentice hall PTR New Jersey, 1996.

[155] Hirotogu Akaike. Information theory and an extension of the maximum likelihood principle. In *Selected papers of hirotugu akaike*, pages 199–213. Springer, 1998.

[156] Jian-Feng Gu and Ke Wu. Quaternion modulation for dual-polarized antennas. *IEEE Communications Letters*, 21(2):286–289, 2017.

[157] Donald G Brennan. Linear diversity combining techniques. *Proceedings of the IRE*, 47(6):1075–1102, 1959.

[158] Elena Bergamini, Pélagie Guillon, Valentina Camomilla, Hélène Pillet, Wafa Skalli, and Aurelio Cappozzo. Trunk inclination estimate during the sprint start using an inertial measurement unit: A validation study. *Journal of applied biomechanics*, 29(5):622–627, 2013.

[159] Yifan Chen, Jianqi Teo, Joshua Chong Yue Lai, Erry Gunawan, Kay Soon Low, Cheong Boon Soh, and Predrag B Rapajic. Cooperative communications in ultra-wideband wireless body area networks: Channel modeling and system diversity analysis. *IEEE Journal on Selected Areas in Communications*, 27(1):5–16, 2009.

[160] Zdravko I Botev and Pierre L'Ecuyer. Efficient probability estimation and simulation of the truncated multivariate student-t distribution. In *Proceedings of the 2015 Winter Simulation Conference*, pages 380–391. IEEE Press, 2015.

[161] Fredrik Rusek, Daniel Persson, Buon Kiong Lau, Erik G Larsson, Thomas L Marzetta, Ove Edfors, and Fredrik Tufvesson. Scaling up mimo: Opportunities and challenges with very large arrays. *IEEE signal processing magazine*, 30(1):40–60, 2013.

[162] Erik Luther. 5g massive mimo testbed: From theory to reality. *white paper, available online: https://studylib. net/doc/18730180/5g-massive-mimo-testbed–from-theory-to-reality*, 2014.

[163] Sohail Payami and Fredrik Tufvesson. Channel measurements and analysis for very large array systems at 2.6 ghz. In *Antennas and Propagation (EUCAP), European Conference on*, pages 433–437. IEEE, 2012.

[164] Xiang Gao, Ove Edfors, Fredrik Rusek, and Fredrik Tufvesson. Massive mimo performance evaluation based on measured propagation data.

[165] Paul Harris, Siming Zang, Andrew Nix, Mark Beach, Simon Armour, and Angela Doufexi. A distributed massive mimo testbed to assess real-world performance and feasibility. In *Vehicular Technology Conference (VTC Spring), 2015 IEEE 81st*, pages 1–2. IEEE, 2015.

[166] Stephan Jaeckel, Leszek Raschkowski, Kai Börner, and Lars Thiele. Quadriga: A 3-d multi-cell channel model with time evolution for enabling virtual field trials. *IEEE Transactions on Antennas and Propagation*, 62(6):3242–3256, 2014.

[167] Zhou Zhou, Xiang Gao, Jun Fang, and Zhi Chen. Spherical wave channel and analysis for large linear array in los conditions. In *Globecom Workshops (GC Wkshps), 2015 IEEE*, pages 1–6. IEEE, 2015.

[168] Joao Vieira et al. A flexible 100-antenna testbed for massive mimo. In *Globecom Workshops (GC Wkshps), 2014*, pages 287–293. IEEE, 2014.

[169] Yu Yu, Peng-Fei Cui, Jun She, Yang Liu, Xi Yang, Wen-Jun Lu, Shi Jin, and Hong-Bo Zhu. Measurement and empirical modeling of massive mimo channel matrix in real indoor environment. In *Wireless Communications & Signal Processing (WCSP), International Conference on*, pages 1–5. IEEE, 2016.

[170] Jun She, Chen Gao, Yu Yu, Peng-Fei Cui, Wen-Jun Lu, Shi Jin, and Hong-Bo Zhu. Measurements of massive mimo channel in real environment with 8-antenna handset. In

Wireless Communications and Signal Processing (WCSP), International Conference on, pages 1–4. IEEE, 2017.

[171] Leslie Rusch, Cliff Prettie, David Cheung, Qinghua Li, and Minnie Ho. Characterization of UWB propagation from 2 to 8 GHz in a residential environment. *IEEE Journal on Selected Areas in Communications*, 2003.

[172] Suiyan Geng and Pertti Vainikainen. Frequency and bandwidth dependency of uwb propagation channels. In *2006 IEEE 17th International Symposium on Personal, Indoor and Mobile Radio Communications*, pages 1–5. IEEE, 2006.

[173] Peng-Fei Cui, Yu Yu, Yang Liu, Wen-Jun Lu, and Hong-Bo Zhu. Body obstruction characteristics for off-body channel under hospital environment at 6 8.5 ghz. In *Ubiquitous Wireless Broadband (ICUWB), 2016 IEEE International Conference on*, pages 1–4. IEEE, 2016.

[174] Joel A Tropp. Greed is good: Algorithmic results for sparse approximation. *IEEE Transactions on Information theory*, 50(10):2231–2242, 2004.

[175] Peng-Fei Cui, J. Andrew Zhang, Wen-Jun Lu, Y. Jay Guo, and Wen-Jun Lu Zhu, Hong-Bo. Sparse channel modelling using multi-measurement vector compressive sensing. In *Global Communications (Globecom), 2018 IEEE International Conference on*. IEEE, accepted, 2018.

[176] Emmanuel J Candes, Yonina C Eldar, Deanna Needell, and Paige Randall. Compressed sensing with coherent and redundant dictionaries. *Applied and Computational Harmonic Analysis*, 31(1):59–73, 2011.

[177] Alfred M Bruckstein, David L Donoho, and Michael Elad. From sparse solutions of systems of equations to sparse modeling of signals and images. *SIAM review*, 51(1):34–81, 2009.

[178] Hirotogu Akaike. Information theory and an extension of the maximum likelihood principle. In *Selected papers of hirotugu akaike*, pages 199–213. Springer, 1998.

[179] Jie Chen and Xiaoming Huo. Theoretical results on sparse representations of multiple-measurement vectors. *IEEE Transactions on Signal Processing*, 54(12):4634–4643, 2006.

[180] Sangnam Nam, Mike E Davies, Michael Elad, and Rémi Gribonval. The cosparse analysis model and algorithms. *Applied and Computational Harmonic Analysis*, 34(1):30–56, 2013.

[181] Joel A Tropp, Anna C Gilbert, and Martin J Strauss. Algorithms for simultaneous sparse approximation. part i: Greedy pursuit. *Signal Processing*, 86(3):572–588, 2006.

[182] David L Donoho. De-noising by soft-thresholding. *IEEE transactions on information theory*, 41(3):613–627, 1995.

[183] Theodore S Rappaport et al. *Wireless communications: principles and practice*, volume 2. prentice hall PTR New Jersey, 1996.

[184] Siavash M Alamouti. A simple transmit diversity technique for wireless communications. *IEEE Journal on selected areas in communications*, 16(8):1451–1458, 1998.